Optimizing the Single-Molecule Counting Process of Solid-State Nanopores

Martin Charron

Thesis submitted to the Faculty of Graduate and Postdoctoral Studies in partial fulfillment of the requirements for the MSc. degree in Physics

Ottawa-Carleton Institute for Physics
Department of Physics
Faculty of science
University of Ottawa

Contents

Summary

Due to their intrinsic single-molecule resolution and now easy fabrication and microfluidic integration, solid-state nanopores show great potential of becoming flexible low-cost, point-of-need, ultra-sensitive biomarker detection sensors. Since nanopores are still limited by the arrival time of the analyte to the sensor, reaching ultra-low concentration levels (fM) in a reasonable measurement time remains a challenge. Before approaches solving this problem become possible, one subject, not often discussed, needs to be addressed: The reliability and uncertainty of capture-based nanopore measurements. Counting with nanopores is often accomplished through measuring translocation frequencies. However, limitations of nanofabrication techniques tend to produce solid-state nanopores with, at the atomic scale, different geometries or chemical structures. A question then arises: How different will the measured capture rate be for two seemingly identical pores, i.e. pores intended to have same diameter and thickness within the fabrication capabilities? One solution to circumvent this problem is to use calibration curves by measuring the capture frequency of different concentrations, which prompts a follow up question: Does a single nanopore capture frequency change over time during the course of an experiment? This thesis investigates these two questions and experimentally shows that intra-pore and inter-pore capture variations can be significant, thus reducing the precision of simple nanopore counting to determine concentration of an analyte. To address these complications, a solution involving an internal calibrator is presented and is demonstrated to increase the sensitivity of concentration measurements.

Sommaire

En raison de leur résolution mono-moléculaire intrinsèque et de leur facilité de fabrication et d'intégration micro-fluidique, les nanopores à l'état solide présentent un grand potentiel pour devenir des détecteurs de biomarqueurs ultra-sensibles, versatiles, peu coûteux et permettant des diagnostics directement aux points de services ou de besoin. Comme les nanopores sont encore limités par le temps d'arrivée de l'analyte au capteur, il est difficile d'atteindre des niveaux de concentration ultra-faibles (fM) en un temps de mesure raisonnable. Avant que des approches permettant de résoudre ce problème ne deviennent possibles, un sujet, peu souvent abordé, doit être étudié en détail : La fiabilité et l'incertitude des mesures de nanopore basées sur la fréquence de capture. Le comptage à l'aide de nanopores s'effectue souvent en mesurant les fréquences de translocation. Cependant, les limites des techniques de nano-fabrication tendent à produire des nanopores d'état solide avec, à l'échelle atomique, différentes géométries ou structures chimiques. Une question se pose alors: Dans quelle mesure le taux de capture mesuré sera-t-il différent pour deux pores apparemment identiques, c'est-à-dire des pores destinés à avoir le même diamètre et la même épaisseur dans les limites de capacités de fabrication? Une solution pour contourner ce problème est d'utiliser des courbes de calibration en mesurant la fréquence de capture de différentes concentrations, ce qui suscite une autre question: La fréquence de capture d'un nanopore change-t-elle avec le temps au cours d'une expérience? La présente thèse examine ces deux questions et démontre expérimentalement que les variations de capture intra- et inter-pore peuvent en effet être significatives, réduisant ainsi la précision du simple processus de comptage des nanopores pour déterminer les concentrations d'analytes. Pour remédier à ces complications, une solution faisant appel à un calibreur interne est présentée et il est démontré qu'elle augmente significativement la sensibilité des mesures de concentration.

Acknowledgements

On February 16th of 2017, I learned that after a few failed attempts, I was finally admitted into the physics master's program. On that same day, my family also learned that my mother had lung cancer that had spread to her brain. Quite a coincidence. For this reason, I was distracted throughout my master's, but also missed a lot of time in the lab to be at hospitals or wherever I was needed most. I will however never regret any experiment, meeting or entire workday missed to spend time by my mother's side. In December 2018, around the time I sat down to start writing an article and this thesis, her condition worsened. In early February, doctors estimated correctly that she had 2 months to live. One of her first reaction to this news was that she felt bad for delaying my thesis writing and eventual graduation. I hope she understood how pointless all of this really was to me in that instance. She was a wonderful woman and a fantastic mother. Coming back to work and writing this thesis has been quite emotional and has taken me more time than expected; this thesis to me materializes the process of moving on. I am however tired and look forward to the day this thesis will be printed and stored on a shelf, never to be read again.

Pretty dramatic start, sorry. Of course, throughout harsh times, some people make life not only bearable, but pleasant, interesting and filled with laughter and love. My entire family is evidently included in that group; particularly, my beloved father and sister Alain and Valérie, respectively. You guys are the most ridiculously funny and kind people I know and I'm thankful for every day I get to spend with you, whether it be through good or bad times.

I of course want to thank my lab coworkers for all the knowledge, time and help they've shared with me throughout the years. Thank you Aidan, Autumn, Caroline, Dan, Javad, Kyle, Liqun, Lucas, Matt, Philipp, Simon and Zach (Alphabetical order, don't worry Z-man). I should

emphasize my appreciation towards Kyle, since he's the one I showered with questions the most on a regular basis. Thanks to all of you for everything that you've taught me, or that we took the time to learn together. I would also like to slip in an apology, since I'm usually a more helpful, present and cheerful colleague and friend.

A very special thank you to Vincent for the chance you gave me, a not-so-well performing undergrad, to pursue graduate studies in your lab, and of course for being so understanding of my personal situation once the program started. I truly enjoy working under your guidance and am excited to advance this work in the future at a faster pace and with a healthier mental state.

Lastly but not least, to Alexandra: I'll be eternally grateful for everything you've done and endured for me in recent years. You are the most kind-hearted and the sweetest person I know. I love spending every day by your side, laughing at terrible jokes all day long. I'm truly lucky to share my life with you, I love you.

Statements of Originality and Contributions

The work presented in this thesis contains a combination of literature review, original interpretation of literature, and original research. Research was conducted during work as an MSc student under the supervision of Vincent Tabard-Cossa in the Centre for Interdisciplinary Nanophysics, Department of Physics at the University of Ottawa.

Chapter 3 contains a literature review of the nanopore capture process. In it, I present several concepts in order to centralize the relevant information and filter out outdated or proven wrong ideas. A few other key concepts are derived simply due to being hard to find or not well defined in publications or online.

Chapter 4 represents the work done after Kyle Briggs came up with the idea of using an internal calibrator for quantification. I contributed to the large majority of this body of work by designing and performing experiments, analyzing data from said experiments and writing and publishing a manuscript. Simon King and Matthew Waugh helped in acquiring data, whereas experimental details were discussed with Kyle Briggs and Vincent Tabard-Cossa. Everyone mentioned helped in the article writing process.

Chapter 5 comprises simulation work I completed that accompanied the previous chapter's publication as supporting information. Although not publication-worthy, the length and conclusions drawn from this numerical study are worthy of their own chapter in this thesis. I contributed to this work almost in its entirety, accompanied by discussions with Kyle Briggs and Vincent Tabard-Cossa on the meaning and interpretation of results.

Chapter 4 is a reproduction of the following publication:

Charron, M.; Briggs, K.; King, S.; Waugh, M.; Tabard-Cossa, V. Precise DNA Concentration Measurements with Nanopores by Controlled Counting. *Anal. Chem.* **2019**, acs.analchem.9b01900. https://doi.org/10.1021/acs.analchem.9b01900

I was given the opportunity to present posters of my work at the 61st annual Biophysical Society Meeting in New Orleans in New Orleans, Louisiana in February 2017, at the Biophysical Society of Canada Meeting in Montreal, Québec in May 2017, and at the NHGRI Advanced Genomic Technology Development Meeting in Boston, Massachusetts in May 2019:

Charron, M.; Baker-Murray, A.; Briggs, K.; Karau, P.; King, S.; Tippins, C.; Tabard-Cossa, V. *Counting 50bp DNA with Solid-State Nanopores*. Biophysical Society Meeting

Charron, M.; Waugh, M.; Briggs, K.; Berryman, S.; King, S.; Gunn, D.; Tabard-Cossa, V. *An instrument to Quantify DNA using Solid-State Nanopores.* Biophysical Society of Canada Meeting

Charron, M.; Briggs K.; King, S.; Waugh, M.; Tabard-Cossa, V. *Calibrating Capture Rates of Solid-State Nanopores for Precise DNA Concentration Measurements*. Advanced Genomics Technology Development Meeting

In partial fulfilment of the requirements for the Physics Master's degree at the University of Ottawa, I presented my work at the Ottawa-Carleton Institute for Physics student symposium in December 2018:

Charron, M.; Briggs K.; King, S.; Waugh, M.; Tabard-Cossa, V. *Optimizing dsDNA Concentration Determination using Solid-State Nanopores and Controlled Counting*. Ottawa-Carleton Institute for Physics

The work presented in this thesis resulted in the following patent:

U.S. Patent Application for the Calibrating Nanopore Capture Rates technology was filed on April 26, 2019 and assigned application number 16/395,910. Inventors: Kyle Briggs, Martin Charron and Vincent Tabard-Cossa.

List of Figures

Chapter 1

Introduction to Single-Molecule Detection Techniques

The presence of diseases in living organisms can result in increased productions of specific biomarkers, such as proteins, circulating nucleic acids or cancer cells. As a result, the abundance of these pathogen-associated target labels can be indicative of the progress or development of the instigating disease. For many diseases, the concentration of such biomarkers can be quite low in the range of $10^{-12}\ M$ down to $10^{-18}\ M$ and possibly lower.[1–3]

In the past two decades, measurement science has made great progress in studying and developing ultrasensitive biomarker sensors.[2–13] When sensing low concentrations (sub-picomolar), it becomes apparent that optimal counting techniques rely on single-molecule measurements, instead of ensemble measurements.[10] Indeed single-molecule techniques not only offer the advantage of counting individual molecules, but also typically capture the heterogeneity of the kinetics and dynamics of a sample.[1,8] To reach ultrasensitive detection limits, a detection assay should meet three different specifications: (1) High sensitivity, (2) low response time and (3) selectivity.[2] Sensitivity relates to the "slope of a calibration curve",[14] with the ultimate sensitivity being single-molecule resolution, i.e. detecting one molecule at a time. Note that sensors with ultimate sensitivity are only considered useful if accurate quantification of target analyte can be achieved within reasonable response times (usually minutes). Together, sensitivity and response time allow determination of the theoretical limits of detection (LOD); the lowest concentrations at which analytes can be accurately quantified in a pure sample. For real-world applications however,

target molecules will be extracted from various clinical specimen, such as blood, serum, plasma, urine, etc., which are expected to contain an extremely wide variety of biomolecules. If background molecules generate non-specific signals indiscernible from target analyte signals, this further puts a constraint on the detection limit.

In addition to ultra-sensitivity, further challenges must be met in order to optimize the applicability and ease-of-access of ultrasensitive assays. An accessible and decentralized assay should be of low-cost, and of small volume in order to allow transportability and point-of-care testing. Ultrasensitive single-molecule-detection assays should strive to acquire an accessibility status similar to lateral flow assays (e.g. Pregnancy tests) or glucose-meters sold over the counter. The following chapter introduces various single-molecule techniques and describes how each method faces the ultrasensitivity challenges previously mentioned.

1.1 Fluorescence-Based Detection

The first successful single-molecule (SM) detection techniques were achieved using fluorescence measurements.[10] Since most molecules are only weakly fluorescent, if at all, this most often requires labelling the desired molecules with fluorescent dyes. This is superior to simple absorption measurements due to the low absorption cross section of single molecules.[10] Dye-label methods are however critiqued due to the induced modifications to the target molecule's kinetics. Nevertheless, fluorescence techniques have shown great quantification success over the years, as briefly described here.

The most straightforward single-molecule fluorescence techniques consist in exciting fluorophores with the use of a laser. This was first achieved using total internal reflection fluorescence microscopy (TIRF) to excite any molecule diffusing into the evanescent wave above

the surface induced by a laser reflecting off the bottom of the said surface.[15] Single target molecules are identified and quantified by detecting photon bursts emitted by the excited fluorescent-dyed molecules over time (***Figure 1***a), the frequency of which depends linearly on the concentration of target molecules. Similar results can also be achieved using a laser beam tightly focused on a capillary tube through which molecules flow or diffuse, as depicted **Figure *1***b.[9] Labelled molecules transiting through the laser's sensing region, its focal point, are excited, emit light and are then quantified. A problem that arises with such diffusion-based techniques is that signal frequencies depend on the rate at which molecules diffuse or flow into sensing regions, which for laser-induced detection can be quite small, on the order of a few microns. Detecting ultra-low concentrations therefore requires extremely long experimental times and is simply not suitable for real-world applications. For this reason, diffusion-limited techniques with small sensing regions are typically compatible with detection limits in the high-picomolar to nanomolar concentration range.

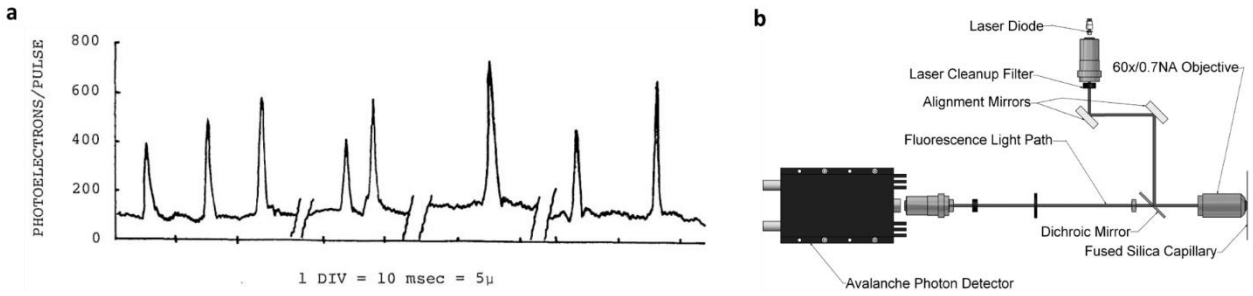

Figure 1. (a) Photometric signals from single molecule swept past illuminated aperture.[15] (b) Erenna immunoassay capillary-based detection system.[9]

Digital polymerase chain reaction (dPCR) is a nucleic acid quantification method that avoids long measurement durations through the use of wide-field measurements.[16–20] Basic PCR is used as a way to replicate and amplify the amount of DNA molecules of a specific sequence; dPCR consists of adding fluorophores in the PCR mix to dye the target sequences, followed by

diluting and aliquoting the DNA mixture into a high number of small volumes, in such way that each aliquot either contains either 1 or 0 target DNA strand. Running PCR reactions on every aliquot simultaneously, each volume initially containing 1 molecule fluoresces, whereas volumes with no target molecule do not. The concentration of the target DNA can therefore be directly inferred by simply counting the number of lit volumes versus the total cumulative volume. The detection limit of this method depends highly on the number of aliquots and on their volume. For this reason, dPCR's limit and range of detection can be highly increased using microfluidics to encapsulate nucleic capsules in water-in-oil droplets,[18,19] or micro-fabricated wells,[20] as pictured in **Figure *2***. Using multivolume micro-fabricated wells in fluidic channels, a LOD of 500 molecules/mL ($\sim 10^{-18}\ M$) is obtained.

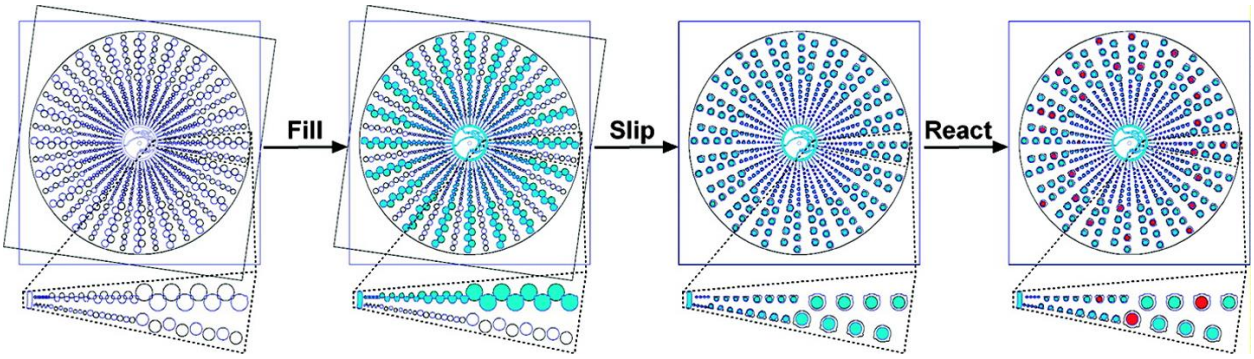

Figure 2. Schematic for radial "SlipChip" to perform multivolume digital PCR. Design consists of 160 wells each at 125, 25, 5, and 1 nL. Sample is loaded from the center and after filling is rotationally slipped to isolate wells. After the reaction, wells containing template have enhanced signal and can be counted.[20]

Although dPCR meets ultrasensitive detection limits and criteria for nucleic acid quantification, no amplification analogous to PCR exists for proteins or other biomarkers. Versatile assays have therefore been developed in order to detect wider ranges of biomarkers. One method of lowering the LOD of fluorescence-based methods is to amplify signals by pre-concentrating and immobilizing target molecules on surfaces. This can be achieved using single-molecule pull-down assays,[21] where target molecules are captured by surfaces functionalized with

capture antibodies. Fluorophore-labelled detection antibodies or fluorescent protein tags (FP) are added to solution and bind to a different epitope of the target molecule, as seen in **Figure *3***. The fluorescent protein complex can therefore be quantified and analyzed using TIRF microscopy to scan the desired surface. This type of assay is named sandwich immunoassays and is commonly used to meet the specificity criteria of ultrasensitive detection.

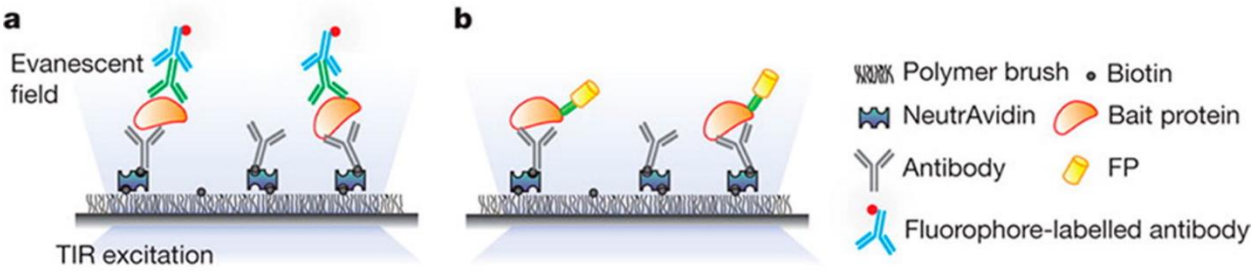

Figure 3. Schematic for single molecule pull assay. Immunoprecipitated protein complexes are visualized using TIRF microscopy via (a) fluorophores-labeled antibody or (b) fluorescent protein tags (FP).[21]

A common detection method relies on extending the sensing interface into the solution using magnetic micro-particles (MP) dispersed in solution.[2,8,10] This clever technique makes use of sandwich immunoassays by immobilizing target proteins on the surfaces of MP functionalized with target-specific capture antibodies. Collecting the biomarker-MP complex using magnets and flushing solution removes background molecules and therefore reduces non-specific binding. Two market-available ultrasensitive detection methods make use of this MP-amplification method yet differ in their sensing methods. The first method was developed by Singulex and consists in binding dyed antibodies to the MP-bound proteins, completing the sandwich immunoassay.[7] The solution is then replaced by a lower volume elution buffer, disrupting antibody-analyte interaction and releasing the target molecules from the MP. This immunoassay has been commercialized under the name “Erenna” and uses the previously described laser excitation in capillaries to detect and quantify the analyte-antibody complex. A more recent and sensitive method termed SiMoA

for Single Molecular Array using a digital ELISA approach was commercialized by the company Quanterix.[3] ELISA stands for enzyme-linked immunosorbent assay. The main difference between the Erenna and SIMoA assays is the detection antibody of an ELISA is not bound to a fluorescent label but to an enzyme that can covert a substrate into light. After the sandwich assay is completed, the MP beads are loaded into dense arrays of femtoliter-sized wells. After adding a fluorogenic enzyme substrate to the solution, the wells are sealed. Much like dPCR, wells which contain the target biomarker-antibody complex generate a highly concentrated fluorescent product due to the single enzyme catalysis ("on" or "1"), whereas wells with MP without the complex remain dark ("off" or "0"). **Figure *4*** depicts the various steps needed for digital ELISA. This detection technique has the advantage of using wide-field measurements, using a simple CCD camera to detect fluorescent wells and relying on Poisson statistics and calibration curves to infer concentrations. Digital ELISA was shown to have a detection limit of $10^{-19}\ M$ (~60 molecules in a milliliter sample) and can routinely detect in-serum protein concentrations of $10^{-15}\ M$.

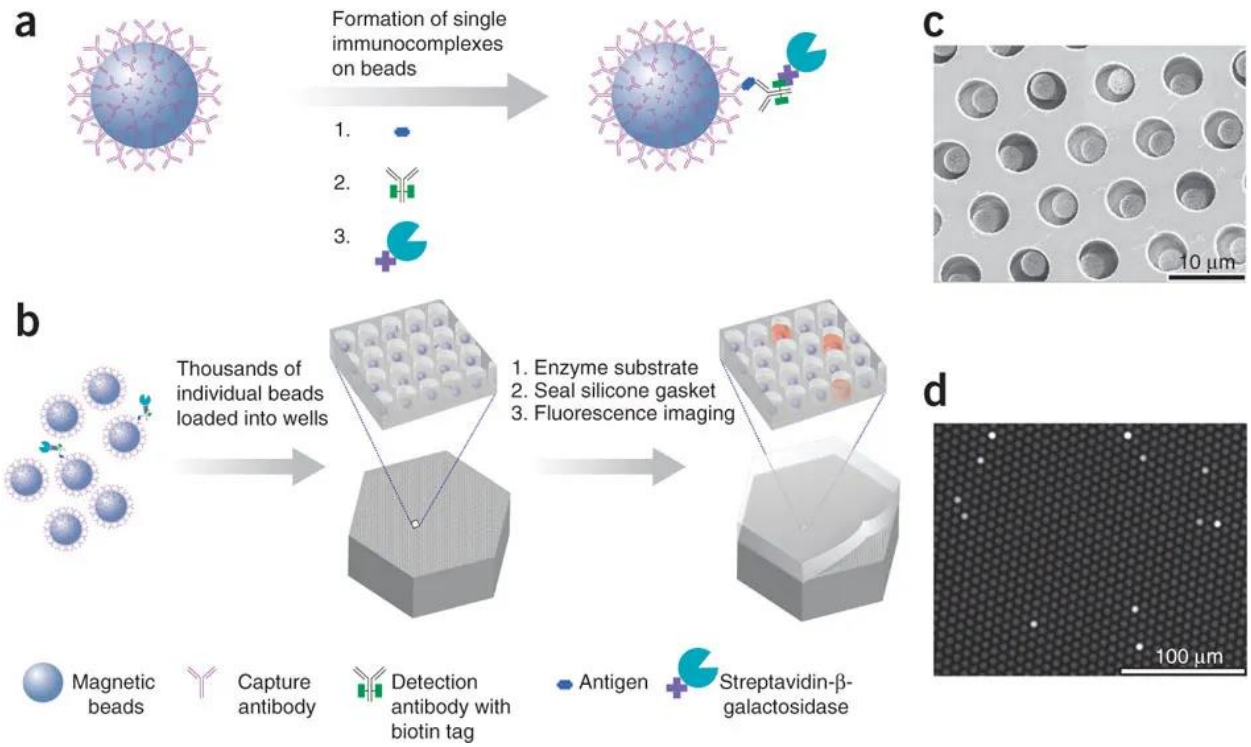

Figure 4. Digital ELISA based on arrays of femtoliter-sized wells. (a,b) Single protein molecules are captured and labeled on beads using standard ELISA reagents (a), and beads with or without a labeled immunoconjugate are loaded into femtoliter-volume well arrays for isolation and detection of single molecules by fluorescence imaging (b). (c) Scanning electron micrograph of a small section of a femtoliter-volume well array after bead loading. Beads (2.7 µm diameter) were loaded into an array of wells with diameters of 4.5 µm and depths of 3.25 µm. (d) Fluorescence image of a small section of the femtoliter-volume well array after signals from single enzymes are generated. Whereas the majority of femtoliter- volume chambers contain a bead from the assay, only a fraction of those beads possesses catalytic enzyme activity, indicating a single, bound protein molecule. The concentration of protein in bulk solution is correlated to the percentage of beads that carry a protein molecule [3]

1.2 Label-Free Detection

Although fluorescence methods have shown great success, new label-free single-molecule sensing methods are actively being researched. Low LOD have been obtained using methods often relying on similar principles: A transducer is functionalized with receptor molecules (antibodies, oligonucleotides, etc.), and as target biomarkers bind to the sensor, a chemical and/or physical change is observed over time. The details and nature of the measured changes are specific to the assay and type of transducer. Here, three different types of label-free sensors are briefly discussed.

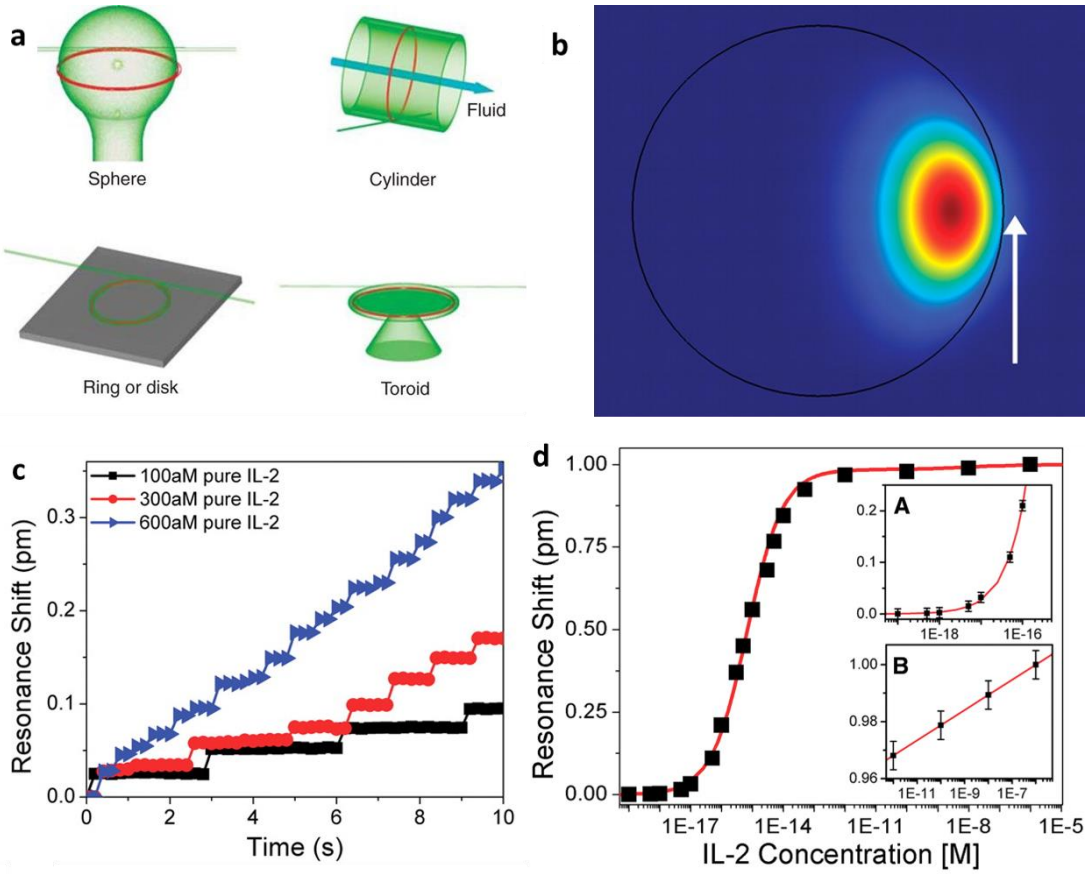

Figure 5. (a) Different whispering gallery microcavities resonator geometries. The WGM is highlighted in red, blue indicates microfluidic flow.[22] (b) A finite element model of a 4-mm microtoroid resonator immersed in water. Although the majority of the optical field resides in the silica toroid, a portion of the field evanesces into the environment (indicated by a white arrow). The interaction of the whispering-gallery mode with the environment, specifically molecules bound on the surface of the toroid, enables the ultrasensitive detection.[5] (c) The position of the resonance wavelength as a function of time at three different interleukin-2 (IL-2) concentrations. As molecules bind to the surface, the resonant wavelength position jumps, creating the steps seen. When the concentration is increased, the general slope of the trace increased because the binding rate increased.[5] (d) Working range and IL-2 dose response of the microtoroid sensor.[5]

Optical microcavities, as depicted in **Figure 5**a, act as ring resonators through which light propagates in the form of whispering gallery modes, due to total internal reflection (TIR) along the curved boundary of the silica resonator.[5,22–24] This internal reflection induces an evanescent wave, much like for TIRF microscopy, which interacts with the local surroundings of the resonator. When coupled with a laser, the precise geometry of the resonator and the nature of its immediate surrounding results in a specific resonance frequency. By functionalizing the surface of the microcavity with capture antibodies, target-molecules binding on the resonator are essentially changing the local refraction index of the medium, and as a result red-shifting the resonance

frequency of the system. Unlike linear functionalized waveguides in which light only interacts once with any bound target-molecule,[4] the sample in a microcavity can be sampled up to 100,000 times. As a result, single-molecule binding events can be individually detected in real-time, as shown in **Figure *5***c.[5] The dynamic range of the microcavity was established by detecting various concentrations of interleukin-2 (IL-2). Significant resonance shifts could be detected with concentrations as low as $5 \times 10^{-18}\ M$ (**Figure *5***d).[5]

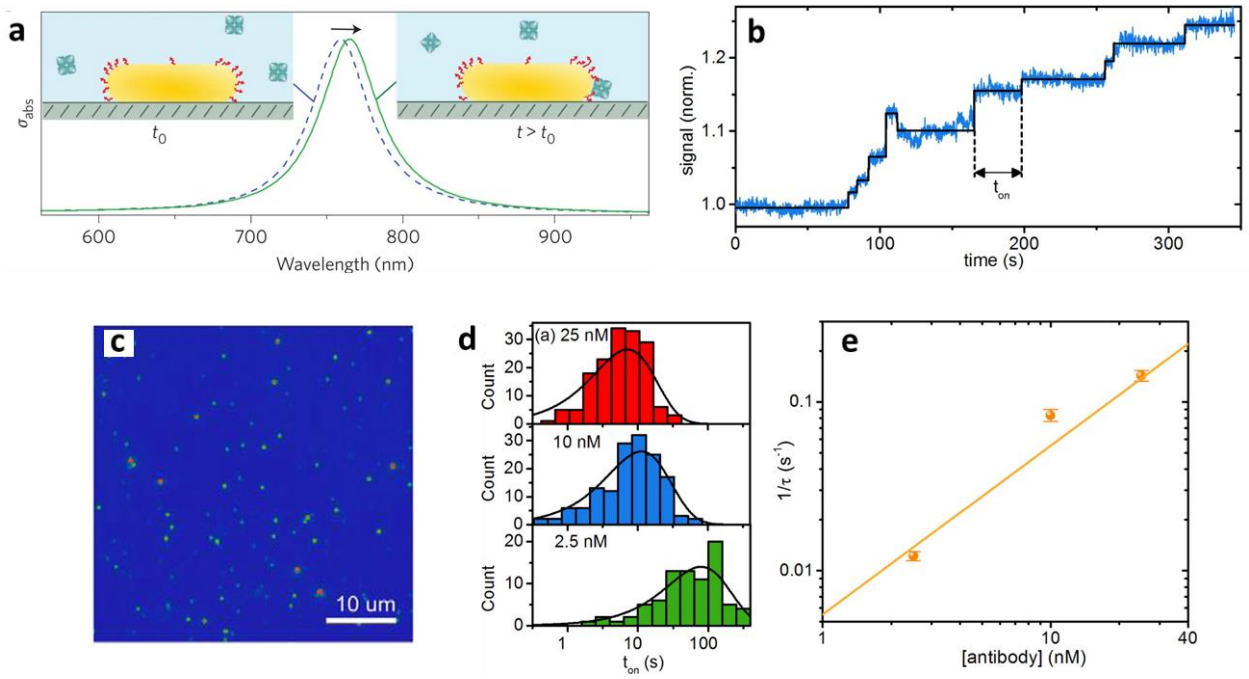

Figure 6. (a) A single gold nanorod functionalized with biotin is introduced into an environment with the protein of interest. Binding of the analyte molecules to the receptors induces a redshift of the longitudinal SPR (exaggerated in the illustration). This shift is monitored at a single frequency using photothermal microscopy.[25] (b) Time-trace of the scattered intensity of a single nanorod (10 nM antibody injected at t = 60 s). The solid line shows a fit with a step- finding algorithm from which is obtained the waiting-time between binding events, t_{on}. (c) Typical CCD image of a sample surface where multiple parallel measurements can be done. The color scale is linear and ranges from 0 (blue) to 16384 (red). (d) Waiting-time distributions for different antibody concentrations. The solid lines are Poissonian fits. (e) Dependence of the mean binding rate on the antibody concentration. The solid line is a first-order power law. The error bars are fitting errors obtained from the Poisson fits in (d).[26] Adapted with permission from [*Beuwer, M. A.; Prins, M. W. J. J.; Zijlstra, P. Stochastic Protein Interactions Monitored by Hundreds of Single-Molecule Plasmonic Biosensors.* Nano Lett. ***2015***, 15 *(5), 3507–3511*] Copyright (2020) American Chemical Society

Functionalized single plasmonic nanoparticles can also be used for single-biomarker molecule detection.[25–28] Plasmonic nanoparticles have a well-defined surface plasmon resonance frequency, which can be altered by its immediate surroundings. Individual target molecules that bind to its functionalized surface therefore shift the resonance and are identifiable, as pictured in

Figure *6*a-b. The attractive feature of plasmonic nanoparticles is that they can be investigated using far-field optics. For this reason, even though each plasmonic nanoparticle has a small sensing region, measurements can be parallelized with the use of a CCD camera (**Figure *6***c), and concentrations can be inferred from Poisson statistics (**Figure *6***d-e).

A more recent non-optical SM technique offers a unique label-free approach, with reported record-setting detection limits. The technique uses electrolyte-gated organic-field-transistors (EGOFETs),[7,29–32] as pictured in **Figure *7***a-d, in which millimeter-sized golden gate electrodes are functionalized with self-assembled monolayers (SAM). The SAMs consist of a chemical layer bound to the electrode and a biological layer bound atop the chemical layer. The biological layer is comprised of tightly packed ($10^4\ \mu m^{-2}$) bio-recognition elements (e.g. capture antibodies), whereas the chemical layer is com prised of alkanethiols with carboxylic terminal groups, which have the property of spontaneously self-assembling on gold surfaces, as depicted in **Figure *7***b-d. Detection of molecules is achieved by measuring the transistor's transfer characteristics (I_D vs V_G) after the introduction of the target molecules, as shown for different concentrations in **Figure *7***e. As more target proteins bind to the SAM, more shift is observed in the transfer characteristics. To quantify this behavior and relate it to a concentration, a calibration curve is acquired by measuring the relative shift in current, $\Delta I/I$, for different concentrations, as shown in **Figure *7***f. Using a negative control to estimate the experimental noise level, a detection limit for the capture of Immunoglobulin-G was determined as consisting of a single protein in a volume of $100\ \mu L$, corresponding to ~10 zM, or $10^{-20}\ M$.[7]

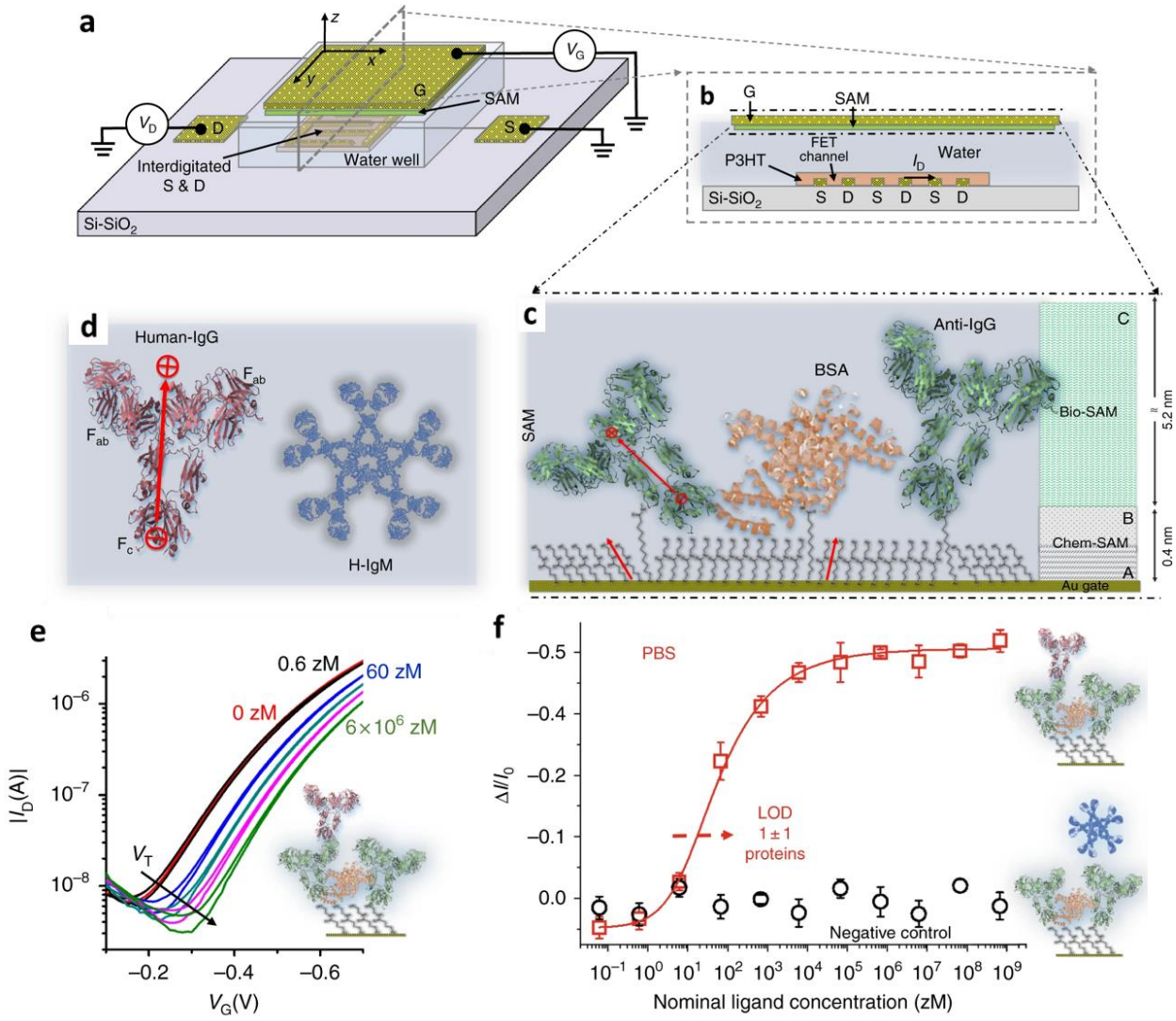

Figure 7. (a) The three-dimensional schematic structure of the field-effect transistor. **(b)** The cross-sectional structure of the transistor channel region. The source (S) and drain (d) interdigitated contacts are defined on a Si/SiO2 substrate and covered by a spin coated p-type, Poly(3-hexylthiophene- 2,5-diyl)-P3HT, organic semiconductor (OSC) layer. A 300 µl volume of HPLC-grade water is dispensed into a polydimethylsiloxane well covering the OSC surface. A bio-functionalized Au-gate stably hangs over the device at a distance of ~4 mm from the OSC surface while in contact with the water. **(c)** Sketch of the capturing SAM, comprising both a chem-SAM of activated-and-blocked 3-mercaptopropionic acid (3-MPA) and 11-mercaptoundecanoic acid (11-MUA) and a bio-SAM of capturing proteins. For the sake of clarity, features are not in scale. The dipole moments associated with the different components are schematically depicted with red arrows. The whole SAM thickness is 5.6. **(d)** Depiction of the structure of IgG and IgM ligands. **(e)** The SiMoT transfer characteristics (ID vs. VG at VD =−0.4 V). The red curve corresponds to the anti-Human-IgG SAM incubated in the bare PBS solution. The same gate is further exposed, in sequence, to PBS standard solutions of IgG at concentrations of 6 zM (black curve), (6 ± 3) × 10 zM (blue curve), (6 ± 1) × 102 zM (dark curve), (6.7 ± 0.1) × 103 zM (magenta curve) and (6.67 ± 0.01) × 106 zM (light green curve). **(f)** The Human IgG/anti-Human-IgG affinity binding calibration curve (red squares) as the relative change of the ID current (ΔI/Io) vs. the IgG concentration. A SAM comprising both the capturing anti-IgG and the BSA is used. The black circles are the negative control responses of the anti-IgG SAM to human-IgM solutions. The proteins are assays from standard solutions in PBS. The fitting of the IgG binding curve with the SiMoT dose curve model described in Supplementary Note 7, is shown as red solid line.[7]

1.3 Nanopores

Nanopores are nanometer-sized holes in ultra-thin membranes immersed in solution. When a potential difference is applied across a nanopore and charged molecules are in solution, they are driven towards and translocate through the pore. When molecules are inside the nanochannels, the ionic current is altered and typically reduced, as depicted in **Figure *8***. Much like the laser-induced fluorescence, by analyzing the current trace it is possible to detect and count the number of molecules that have entered the sensing region and translocated through the nanopore

Figure 8. Continuous current trace with 50bp dsDNA in 3.6M LiCl solution under an applied voltage of 300mV.

Biological nanopores embedded in lipid bilayers (**Figure *9***a) have seen a lot of success for DNA sequencing in the last decade,[33] by offering a fast and cost-effective sequencing solution. Their semiconductor-membrane counterparts, solid-state nanopores,[34] are however better-suited for biomarker sensing, due to their nanometer-tunable geometry,[35–37] a feature that is advantageous when working on detecting analytes of different sizes. There exist multiple ways of fabricating nanopores, and as a result, a large variety of pore geometries and sensors are used in the field. The majority of nanopores are fabricated in free-standing silicon nitiride membranes (**Figure *9***b) by exposing them to high electric-fields,[38] tightly focused laser beam[39] and highly energetic beams of ions[36] or electrons.[35] More recently, glass nanopipettes[40] (**Figure *9***c-d) have emerged as fully functional nanopores, due to the low noise induced by glass membranes.

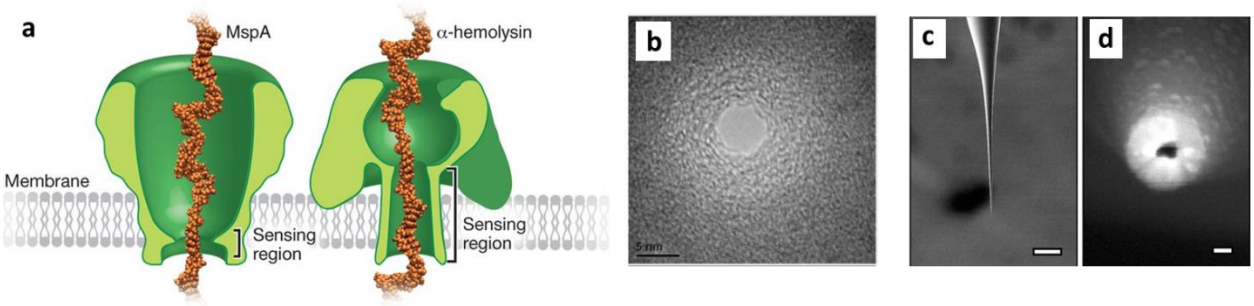

Figure 9. Various types of nanopores (a) Sensing regions in Biological pores, MspA and α-hemolysin.[33] (b) Solid-state nanopore on thin Silicon Membrane.[41] (c)-(d) SEM images of the nanopipette tip (c) and the nanopore at the tip (d). The scale bars are 250 μm and 25 nm, respectively.[42] Adapted with permission from [*Ivanov, A. P.; Actis, P.; Jönsson, P.; Klenerman, D.; Korchev, Y.; Edel, J. B. On-Demand Delivery of Single DNA Molecules Using Nanopipets.* ACS Nano ***2015***, 9 *(4), 3587–3594*] Copyright (2020) American Chemical Society

Under an applied voltage, the sensing region of nanopores is determined by the distance away from the pore at which charged molecules are captured by the induced electric field. The sensing region, termed the capture radius, is determined by the strength of the field outside the pore, and is of the order of 1-10 μm for typical published conditions.[43–46] Due to such a small sensing region, the inherent LOD for reasonable nanopore experiment durations (<1h) is in the high pM to nM range. Solid-state nanopores nonetheless offer features attractive for potential accessible point-of-care ultrasensitive diagnostics. For example, solid-state pores are easily integrable with microfluidics;[47] the material needed for nanopore fabrication and sensing is inexpensive, not bulky and easily transportable. Moreover, because translocation-induced blockage levels and durations depend highly on the geometry of translocating analytes, identifying and quantifying multiple target molecules simultaneously, multiplexing, is possible.

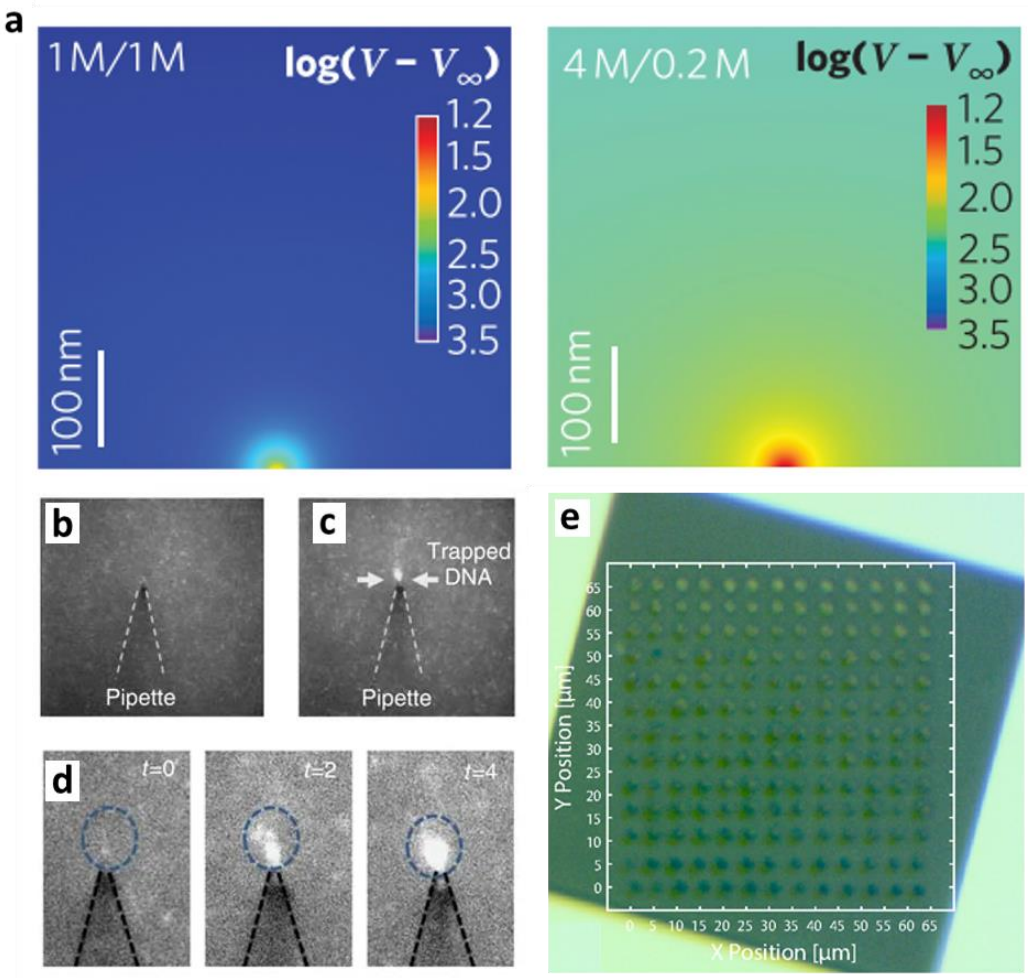

Figure 10. Electric potential maps evaluated numerically in the cis side of the pore, for both symmetric (top left) and asymmetric (top right) KCl concentrations. The pore mouth is positioned at the bottom centre of each image. The potential range outside the pore increases with salt asymmetry.[45] (b) YOYO-labelled 10 kbp DNA sample with the gold-coated nanopipette positioned 50mm above the surface of the planar counter electrode without applied AC voltage.[48] (c) YOYO-labelled 10 kbp DNA sample with an AC voltage (Vpp=20V, f_{AC}=1MHz) being applied between the gold layer on the nanopipette and the counter electrode. (d) Images showing the progression of DNA trapping which occurs at the tip of the nanopipette. (e) An image of the silicon nitride membrane and remaining contact residues after completing 169 automated sequential experiments.[49] Adapted with permission from [*Arcadia, C. E.; Reyes, C. C.; Rosenstein, J. K. In Situ Nanopore Fabrication and Single- Molecule Sensing with Microscale Liquid Contacts. ACS Nano 2017, 11 (5), 4907–4915*] Copyright (2020) American Chemical Society

Multiple techniques can be used to reduce the LOD of nanopores. It has been shown that when immersed in salt gradients with DNA on the low-salt side of the nanopore, the electric field on the DNA-side increases, as depicted in **Figure *10***a, and therefore so do the capture radius and translocation frequency. The detection limit, as a result, can be lowered low pM concentrations.[45] Another demonstrated way of amplifying signals and reducing detection limits is to pre-concentrate the analytes of interest near the pore mouth using dielectrophoretic trapping followed

by normal electrophoretic sensing, as pictured in **Figure *10***b-d. Using this method, the local concentration near the pore is significantly increased and for this reason lower bulk concentrations can be probed and quantified. This was achieved with gold-coated nanopipettes and a LOD of 5 fM for dsDNA detection was achieved.[48] Note also that much akin to plasmonic nanoparticles, increasing the throughput of nanopores can be achieved through parallel sensing. This is demonstrated in Oxford Nanopore's DNA sequencing commercial apparatus, in which ~2000 biological nanopores can be individually addressed in a single-flow cell and instruments to operate hundreds of flow cells simultaneously have been commercialized.[50] Recent solid-state nanopore fabrication techniques have also shown the ability of producing arrays of pores,[49,51,52] as shown in **Figure *10***e.

Although nanopores have in principle high specificity due to molecular-specific signals, simple electrophoretic nanopore sensing can have a hard time differentiating between different populations of globular proteins, which can have in practice very similar current blockage signatures. Moreover, due to non-uniform charges and complex structures affecting their transport properties, sensing certain biomarkers can be arduous.[53–55] To address specificity, and complicated transport properties, various techniques or assays have been proposed for specific detection and quantification. Recently, many techniques rely on binding target proteins or other biomarkers to DNA scaffolds and detecting the complex in the nanopore, where a difference in the current blockage profile is detectable, either from longer or deeper blockages[56–59] (**Figure *11***a) or through the presence of multiple identifiable ionic blockage sublevels[60–63] (**Figure *11***b). Much like with fluorescence techniques, immunoassays in conjunction with nanopore systems can be used in various ways. For example, as shown in **Figure *11***c, tips of nanopipettes have previously been functionalized with capture agents.[64] **Figure *11***d further shows how a sandwich assay can be used

with nanopores with both functionalized membranes and microparticles (MP).[65] After target biomarkers are captured by the MPs, the MP-protein complexes are brought near the pore and bind to detection antibodies in its vicinity. When proteins are sandwiched, discrete blockage reductions are observed, allowing for quantification. This has been reported to result in a limit of detection of 0.8 fM (10^{-15} M), when detecting PSA in blood serum.

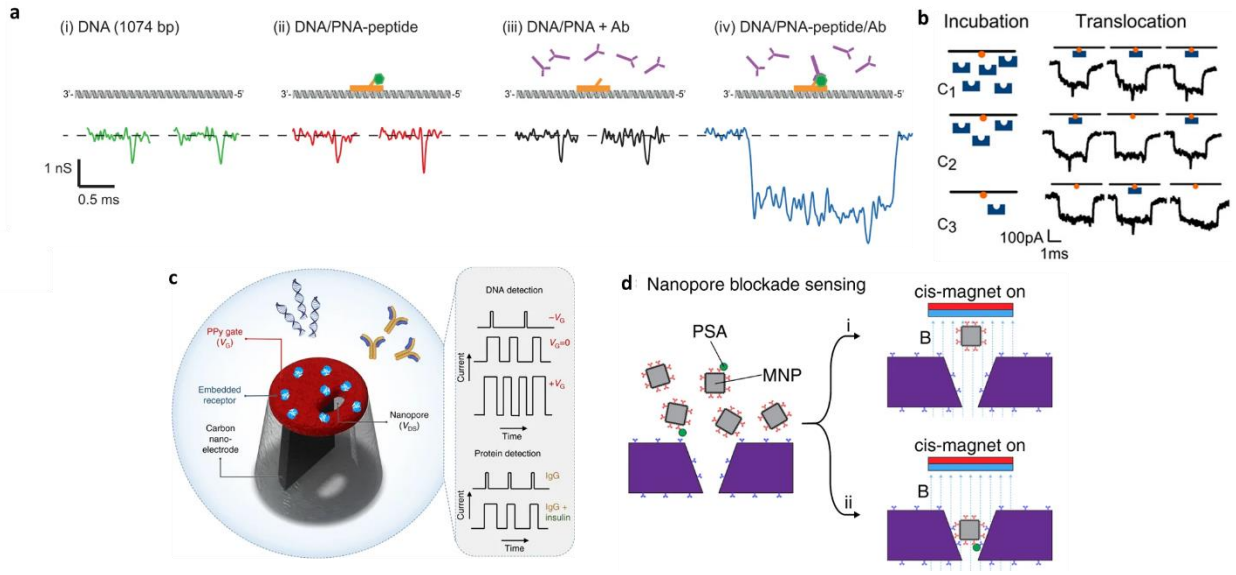

Figure 11. Specificity in nanopore experiments (a) Contrasting molecular cartoons and recorded nanopore event signatures for (i) DNA alone, (ii) DNA/PNA-peptide detection reagent, (iii) DNA/PNA (sans peptide) with antibody and (iv) detection reagent bound by antibody.[56] (b) Schematic and example DNA carrier translocation events after incubation with targeted protein of different concentrations. All the carrier translocation events have secondary current spike positioned in the middle (occupied events). Example events are produced by the biotin−streptavidin system.[62] (c) Schematic of the nanopore extended field-effect transistor (nexFET) biosensor. The nexFET platform is a functionalizable ionic nanopore transistor and is based on a dual-barrel quartz nanopipette with one barrel filled with a carbon nanoelectrode that also forms in a localized manner around the pipette tip. The ring-like carbon-electrode surrounding the nanopore is coated with PPy using ionic current feedback controlled electropolymerization, which serves to decrease the opening size of the second barrel. The PPy acts as a gate electrode surrounding the second barrel, a nanopore, that remains open and acts as a drain-source channel. By controlling the gate voltage molecular transport properties and event rates can be efficiently controlled at the single-molecule level. In addition, the PPy gate layer is ideally suited for embedding of artificial receptors that can be used for selective molecular sensing.[64] (d) Schematic of a nanopore blockade sensor. Active filtering of non-specific nanopore blockade events can be achieved by applying a magnetic field from the cis-side. (i) (Anti-PSA)-MNP that non-specifically adsorbed onto the pore surface will be ejected and thus unblocks the pore, whereas, (ii) (anti-PSA)-MNP that contains captured PSA will continue blocking the pore. Blue dashed lines represent the magnetic field lines, B.[65]

1.4 Thesis Overview

Although nanopores have shown to be versatile and promising single-molecule sensors, a rarely addressed subject is the uncertainty and reproducibility of nanopore quantification methods. Since solid-state nanopores do not have a pre-defined crystal and chemical structure like biological pores do, no two fabricated pores are expected to have the same exact geometry nor surface charge profile at the atomic scale. It has also been observed that pores can grow or shrink over long periods of time (>30 minutes).[66,67] Moreover, for shorter periods of time, nanopores are prone to sudden behavioral changes, such as baseline change, often credited to a pore being partially clogged. Solid-state nanopores are dynamic entities; if they are one day intended to be used as rapid, precise point-of-care ultrasensitive sensors this dynamic behavior should be studied and if measurement errors or irreproducibility are too prominent, methods should be developed to circumvent these uncertainties. Most nanopore assays introduced so far have been presented as proof-of-concept and do not address these problems.

After putting nanopores in context in the extensive field of single-molecule detection techniques, this thesis aims to evaluate and optimize analyte quantification using solid-state nanopores. More specifically, quantification techniques which rely on counting individual translocations rather than measuring the blockage[65,68] or IV rectification[69] induced by target analytes binding inside or near the pore. Before dwelling into quantification-related subjects, a brief overview and description of the fabrication, sensing and analysis of nanopores is given in Chapter 2, whereas Chapter 3 reviews fundamentals of the kinetics of nanopore capture. Chapter 4 begins by evaluating the precision of solid-state nanopores as single-molecule sensors. A high variation in capture rate is observed through single experiments or between seemingly identical pores. The use of an internal standard is shown to significantly lower the measurement

uncertainties, which shows even more promise in controlled environments, rather than proof-of-concept experiments like the ones shown in this work. Chapter 5 follows with an in-depth review of the statistical methods for extracting capture rates or concentrations in non-ideal experimental conditions, mimicking nanopore conditions. This chapter provides a useful guide for experimentalists extracting concentrations or capture rates from imperfect and non-constant sources, in contrast to assuming ideal Poisson processes.

Chapter 2

Solid-State Nanopore Fundamentals

2.1 Fabricating Solid-State Nanopores using Controlled Breakdown

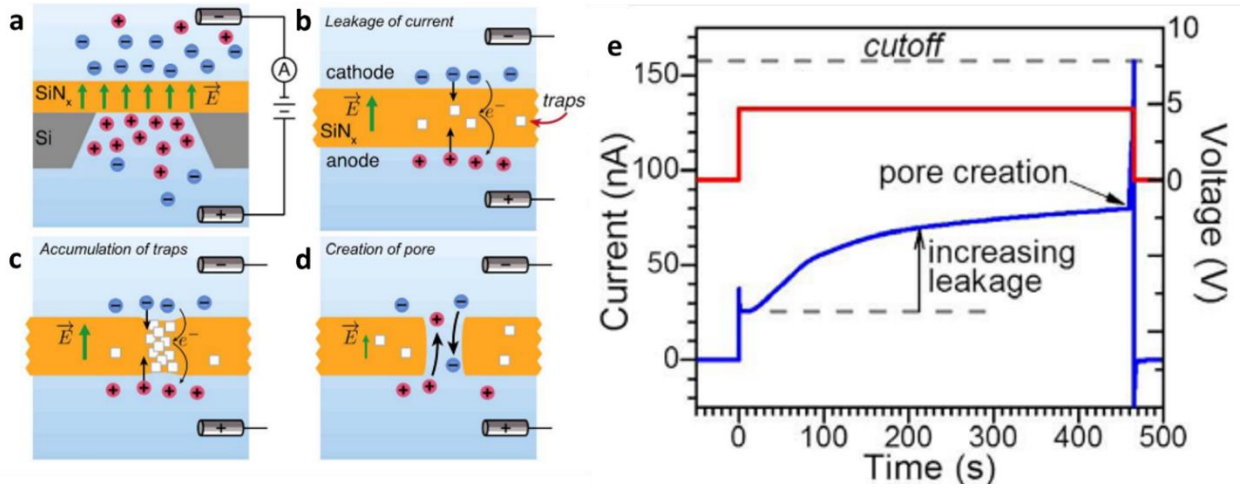

Figure 12. (a) Application of a trans-membrane potential generates an electric field inside the SiNx, and charges the interfaces with opposite ions. (b) Leakage current through the membrane follows a trap-assisted tunneling mechanism. Free charges (electrons or holes) can be produced by redox reactions at the surface or by field ionization of incorporated ions. The number of available charged traps (structural defects) sets the magnitude of the observed leakage current. (c) Accumulation of charge traps produced by electric field- induced bond breakage or energetic charges carries leads to a highly localized conductive path, and a discrete dielectric breakdown event. (d) A nanopore is formed following removal of the defects. (b) Current response under the constant application of electric field. Pore fabrication is detected by a sudden increase in current.[38]

Controlled BreakDown (CBD) is a high-precision, cost-effective, in-solution nanopore fabrication method,[38] which simply requires applying a high electric field across a thin insulating membrane. The applied field can be constant, increase in time or be pulsed. At high enough strengths, the electric field affects the material integrity by creating local defects through which electrons can tunnel (**Figure *12***a-c). This leakage current can be observed before pore fabrication. When too many defects are stochastically created at proximity, a breakdown phenomenon happens, and an opening is fabricated in the material, allowing the transport of ions, and indicated by a sudden increase in current measurements, as seen in **Figure *12***d-e. Using simple electronics,

the sudden current increase can be detected, after which voltage stops being applied. With a fast-enough trigger, it is possible to fabricate small pores of ~1-2 nm repeatedly with success, ideal for nucleic acid analysis.[70] Because of the rapid growth of the nanopore after the breakdown and of the non-Ohmic current response of the nanopore at high voltages, it is hard to obtain a precise initial pore size. AC voltage pulses of lower magnitude than the fabrication voltage are used to slowly increase the diameter of nanopores until a desired size is reached, as depicted in **Figure *13***a-b. Note that this growth technique can be used on pores fabricated by any other methods, once the pore is in salt solution.

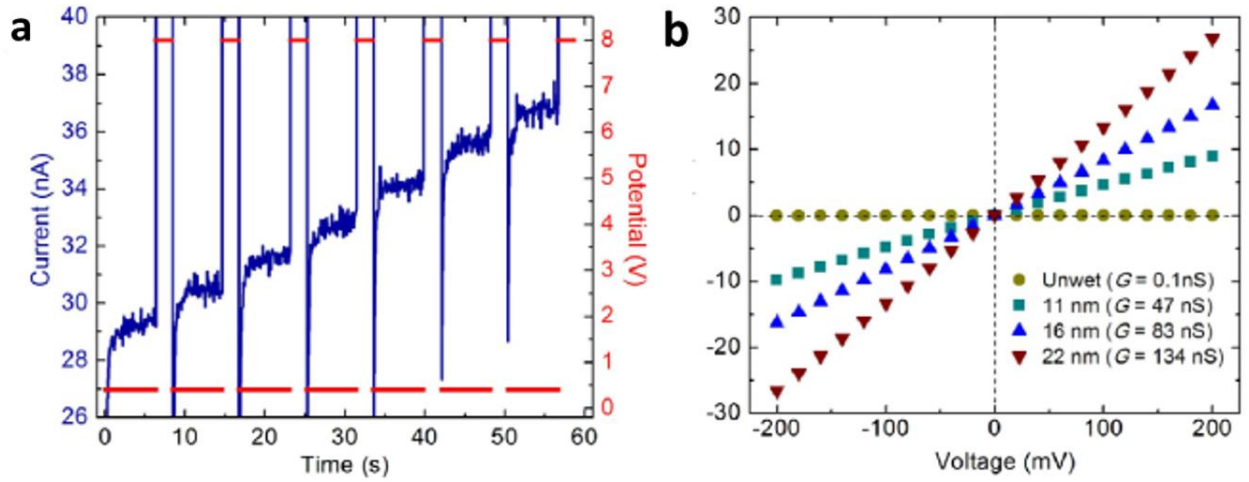

Figure 13. (a) Increasing ionic current (blue) upon treatment with high voltage pulses. Voltage (red) is alternated between 2 s pulses of 8 V and measurement periods 7 s at 400 mV. (b) I–V characteristics of various enlarged pores 30 min after enlarging. The yellow circles are data from an untreated pore that did not wet, and thus had almost no conductance. Upon the application of high field pulses, the pore wetted and was enlarged to 22 nm (red inverted triangles). Green squares and blue triangles were pores enlarged to 11 nm and 16 nm, respectively. In the voltage range of ±200 mV, the pores have a constant conductance.[37]

A simple electronic setup is needed for this fabrication technique (**Figure *14***f). Moreover, the fabrication is done in aqueous solutions, unlike most fabrication methods. This is quite advantageous, since nanopores can be fabricated in the same fluidic cells in which experiments will be run (**Figure *14***a-e). Accordingly, CBD allows for various microfluidics integrations,[47] a feat useful for high parallelization. For these reasons, CBD has potential of playing an important role in developing proper low cost, point-of-care single-molecule assays.

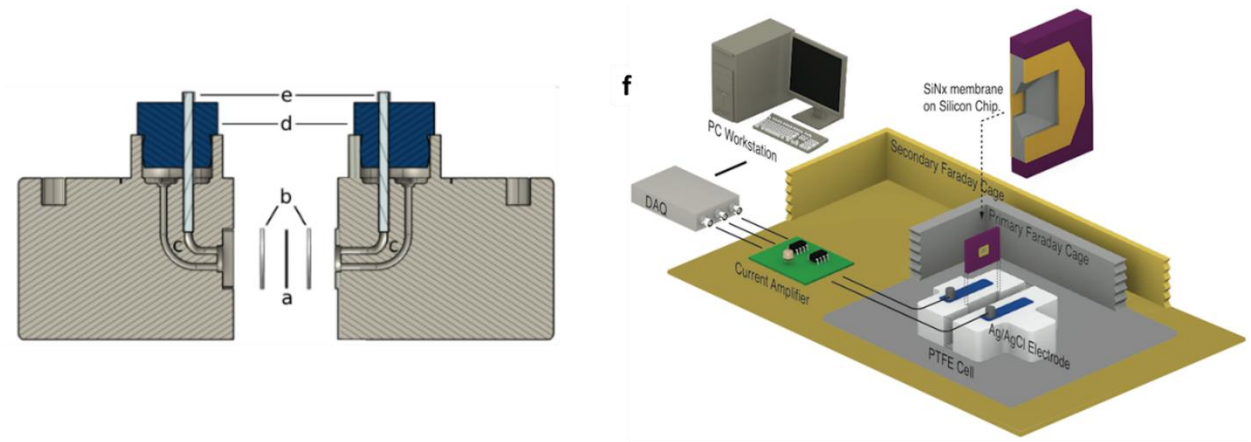

Figure 14. A schematic diagram of the fluidic flow cell used for nanopore experiments. (a) The nanopore support chip. (b) Gaskets used to pressure-seal around the nanopore. (c) Flow channels used to fluidically connect electrodes to the nanopore and to easily introduce samples. (d) Caps that hold the electrode and prevent evaporation of the electrolyte. (e) Ag/AgCl electrodes used to electrically connect to the nanopore.[71](f) Schematic of the fabrication setup. A computer-controlled custom current amplifier is used to apply voltages up to 620 V and measure the current with sub-nA sensitivity from one of the two Ag/AgCl electrodes positioned on either sides of the membrane.[38]

CBD however does have disadvantages. Due to the stochasticity of the fabrication process, it is possible for two pores to be fabricated simultaneously or before the voltage stops being applied after a first pore is detected. From experience, experiments with two pores are easily identifiable through translocation analysis, and such experimental outliers can be eliminated using appropriate fabrication protocols currently under development in the T.Cossa Lab. Further criticism concerning CBD is the fact that due once again to the stochasticity of the process, the location of the fabricated is unknown when running an experiment. Deterministic pore locations could be an attractive feature for some specific experiments requiring precise positioning of the pore next to nanoelectrodes or plasmonic antennas[72] for example. Unfortunately, pore location is hard to detect experimentally since, unlike TEM and ion-beam fabrications, microscopes are not an integral part of the fabrication process. It has been shown however that the location of pores can be pre-determined by locally thinning a small region of the membrane,[73] shining a laser on the membrane surface to help with the local defect induction,[74] using a nanopipette[49] or even using an AFM-tip[51] for breakdown. Interestingly, precise localized CBD fabrication methods, such as with the AFM-tip or nanopipette, allow for easy and rapid nanopore grid fabrication, as depicted in **Figure *14***a-c.

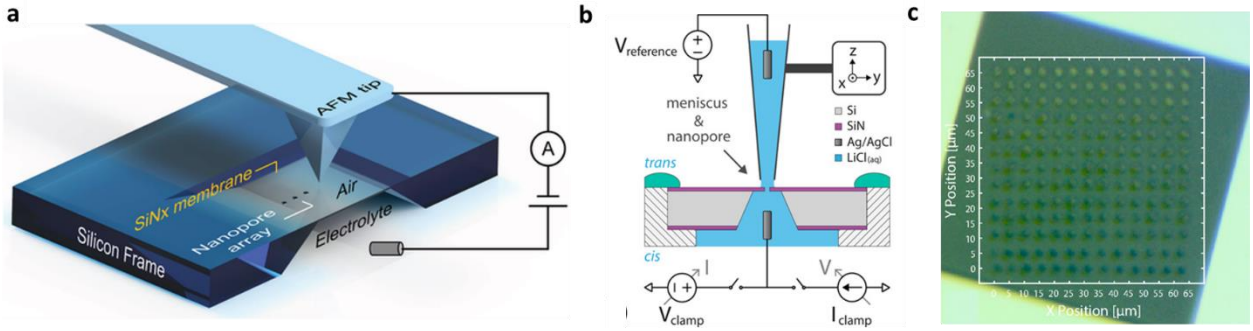

Figure 15. Nanopore fabrication via tip-controlled local breakdown (TCLB). A 3D schematic of the experimental setup depicting an AFM cantilever with a conductive tip positioned over a silicon nitride membrane. Application of a voltage pulse leads to formation of a nanopore at the tip position. Nanopore arrays can be readily formed via control of the AFM tip location, with in situ current measurement at each pore verifying successful pore fabrication at that location.[51] (b) Nanopore fabrication with microscale liquid contact. An illustration of the experimental setup depicting a micropipette with its tip forming a liquid contact to a silicon nitride membrane. A nanopore is formed within the meniscus area and used for single-molecule experiments.[49] (c) An image of the silicon nitride membrane and remaining contact residues after completing 169 automated sequential experiments. Adapted with permission from [*Arcadia, C. E.; Reyes, C. C.; Rosenstein, J. K. In Situ Nanopore Fabrication and Single- Molecule Sensing with Microscale Liquid Contacts. ACS Nano 2017, 11 (5), 4907–4915*] Copyright (2020) American Chemical Society

2.2 Nanopore Conductance

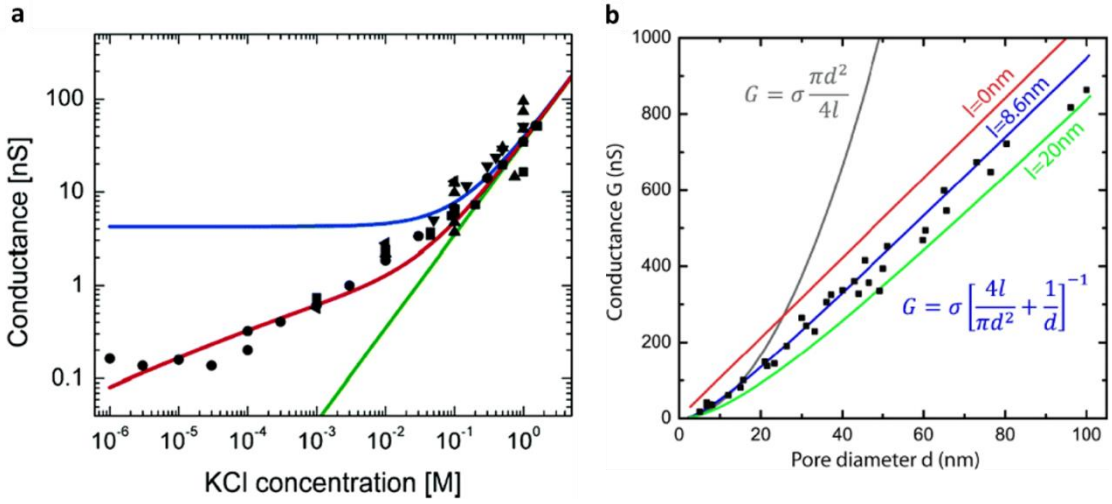

Figure 16. (a) Salt concentration dependence of nanopore conductance. Conductance values of 10 individual pores measured for KCl concentrations from 1 µM to 1 M. Each individual pore has its own symbol. The black upright triangles represent individual pores that were used at a single salt concentration. All of the pores used have diameters of 10 ± 2 nm. The green, blue, and red lines show the results of calculations as predicted by bulk behavior, a model for constant surface charge, and a model for a variable surface charge, respectively.[75] (b) Experimental data for conductance versus pore diameter of pores drilled into a 20 nm thin silicon nitride (SiN) membrane. The solid lines are fits to conductance models ignoring access resistance (gray line, l = 20 nm) and considering access resistance (2) (red, l = 0; blue, l = 8.6 nm; green, l = 20 nm).[76] Figure (a) adapted with permission from [*Smeets, R. M. M.; Keyser, U. F.; Krapf, D.; Wu, M.-Y.; Dekker, N. H.; Dekker, C. Salt Dependence of Ion Transport and DNA Translocation through Solid-State Nanopores. Nano Lett. 2006, 6 (1), 89–95*] Copyright (2020) American Chemical Society

Understanding the origin of the ionic current through a nanopore allows inferring information about the nanopore geometry in real-time during experiments, instead of relying on microscopy measurements. Note that conductance (G), i.e. the current (I) normalized by voltage

(ΔV), $G = I/\Delta V$, is the metric of choice for this topic. The conductance of pores is measured by calculating the slope of current vs voltage curves (I-V) (**Figure *13***b). Multiple sources contribute to the total ionic conductance of the system. The most straightforward conductance model however only considers the bulk of the pore. For a cylinder of diameter d_{pore} and length L_{pore} with a uniform distribution of salt solution of conductivity σ:

$$G_{cyl} = \frac{\sigma \pi d_{pore}^2}{4L_{pore}} \tag{1}$$

It has been shown experimentally however that Equation 1 does not describe the salt concentration[75] and pore diameter[76] dependences properly, as depicted in **Figure *16***a-b. A more complete conductance model considers contributions from the entire geometry of the system and from ionic currents induced by nanopore surface charge:[77]

$$G = \left[\left[\sigma \frac{\pi d_{pore}^2}{4L_{pore}} + \frac{\mu_+ \gamma \pi d_{pore}}{L_{pore}} + \frac{\pi \gamma^2 \lambda_D d_{pore}}{\eta L_{pore}}\right]^{-1} + \frac{1}{\sigma d_{pore}}\right]^{-1} \tag{2}$$

Here, η is the solution viscosity, γ is the surface charge density of the nanopore walls, assumed to be constant, μ_+ is the electrophoretic mobility of shielding cations, and λ_D is the Debye length, the screening length of the surface charge. Equation 2 results from considering three different conductive regions in the system: two access regions and the pore. This is justified by deriving the potential field outside the pore and noting that a significant, albeit typically small, voltage drop is present, as shown in **Figure *17***a-c. The access resistance can be calculated from the same field derivations (see Section 3.2.2), which results in the fourth term of Equation 2, $G_{acc} = 2\sigma d_{pore}$.[78] The first three terms of Equation 2 are parallel contributions that originate from inside the pore. The first term is the bulk cylindrical conductance term, identical to Equation 1, whereas the two other terms originate from the motion of counterions shielding the nanopore surface charges

(R_{surf}), and from the EOF induced by the fluid drag of the counterion motion (R_{eof}).[75,77] Note that this full conductance equation should be used judiciously, since some terms can be ignored in certain experimental conditions in order to avoid overfitting. Moreover, the value of some terms like the surface charge density either have unknown values or are prone to variations from pore-to-pore. In high salt concentrations, for example, the surface charge terms can be ignored, whereas the access resistance can be ignored for small pore-aspect ratios ($d_{pore} < L_{pore}$).

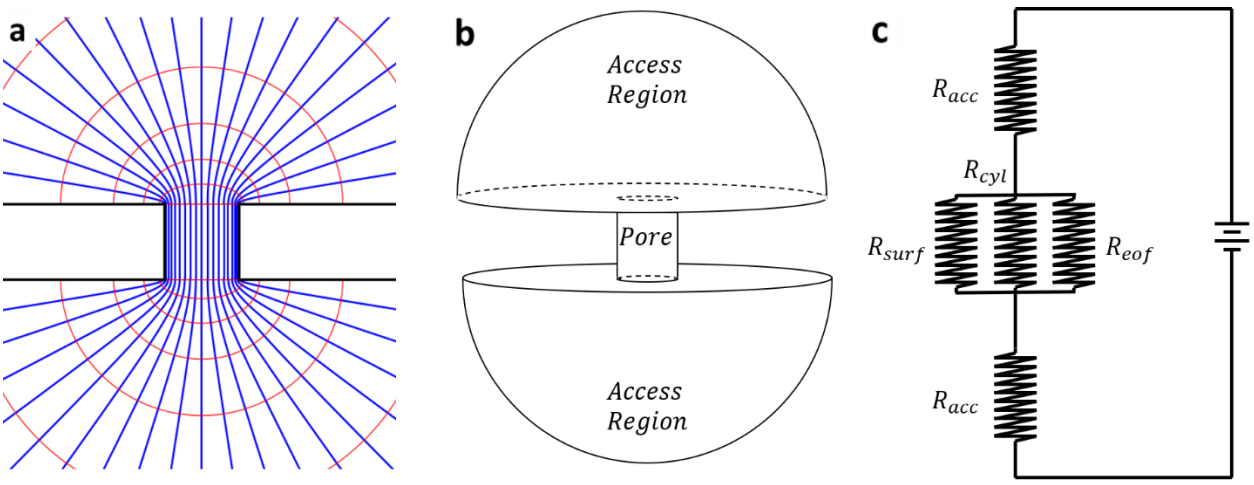

Figure 17. (a) Electric field inside and outside nanopore. (b) Different conductance contributions in the nanopore system. (c) Equivalent circuit representation of the nanopore system. Here, R_{acc}, R_{cyl}, R_{surf} and R_{eof} denote the resistances of the access regions, cylindrical pore, surface charge term and EOF term as explained in the text.

2.3 Current blockages

When charged molecules approach nanopores, they interact with the pore's ionic flow profile, resulting in significant changes of current readings. These current fluctuations enable the analysis and extraction of properties of the nanopore and translocating molecule. For dsDNA or any molecule whose contour length is longer than the pore length, the simplest model for ionic blockage consists in excluding an equivalent cylindrical volume of ions. The excluded cylinder has a cross-sectional diameter of $d_{DNA} = 2.2\ nm$, corresponding to the diameter of dsDNA. The

conductance blockage therefore corresponds to the contribution from ions that would have occupied the volume:

$$\Delta G = \frac{\sigma \pi d_{DNA}^2}{4L_{pore}} \tag{3}$$

This expression proves to be useful under high salt concentration conditions for interpreting different blockage levels obtained experimentally due to molecules translocating in various folded configurations.[79–81] More precisely, blockage depths are quantized: If a polymer is translocating in a folded way such that *n* sections translocate simultaneously, the blockage is expected to be approximately *n* times bigger, as demonstrated in **Figure *18***a. Note that this expression is also useful for experimentally estimating the effective pore length, L_{pore}, done by calculating the most probable unfolded blockage depth, ΔG, and inverting Eq. 3:

$$L_{pore} = \frac{\sigma \pi d_{DNA}^2}{4\Delta G} \tag{4}$$

As described for open-pore conductance, surface charges and their counter-ions can contribute significantly to the ionic current profile in low salt concentrations. This is true for both the charged nanopore walls and the charged dsDNA backbone. In low salt concentrations, the conductance of the charged sleeve surrounding the negatively charged polymer contributes to the signal. For this reason, current fluctuations induced by translocations can result in current increases, rather than the more commonly observed current decreases caused by volume exclusion.[75,82] The dependence of conductance blockage on salt concentration is shown in **Figure *18***b. Such conductance change can be expressed as:

$$\Delta G = \frac{\sigma \pi d_{DNA}^2}{4L_{pore}} - \frac{\mu_+ q_{DNA}}{L_{pore}} \tag{5}$$

Here, q_{DNA} is the effective charge on the DNA per unit length and μ_+ the electrophoretic mobility of counterions moving along the DNA.

Additionally, for higher aspect-ratio pores, the effects of the access region on ionic blockage need to be considered. The presence of the access resistance lowers the voltage across the pore and presents a hard-to-model ionic blockage inside the access region. A model that considers such pore size dependence has been proposed using the access-resistance conductance model (Eq. 2) and defining the conductance blockage as:[76]

$$\Delta G = G\left(d_{pore}\right) - G(d_{with\ DNA}) \tag{6}$$

Here, $d_{with\ DNA}$ is the adjusted pore diameter when DNA is present inside the pore which follows the following relation:$d_{with\ DNA}^2 = d_{pore}^2 - d_{DNA}^2$. **Figure *18***c shows the conductance blockage versus pore diameter alongside the corresponding fit, using Equation 6.

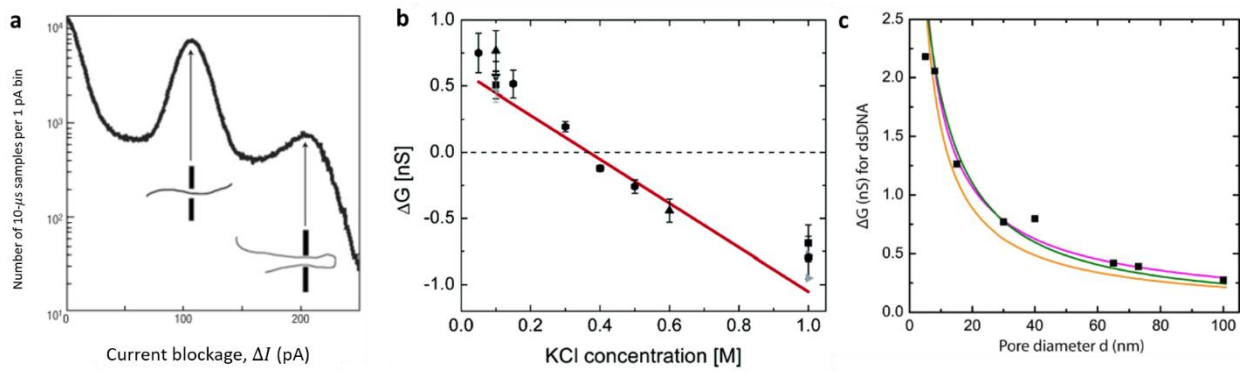

Figure 18. (a) Instantaneous time distribution of blockade current Δ*I* over translocation events. Current is sampled in a 10-μs time window. The quantized blockade currents corresponding to zero, one and two strands in the pore are clearly seen for 10-kb DNA data from a 10-nm pore for a120-mV bias.[80] (b) Conductance changes due to DNA translocation for KCl concentrations between 50 mM and 1 M. Only unfolded (type-1) DNA translocations are analyzed. Each symbol represents an individual pore of diameter 10±2 nm except for the gray right (15 nm) and left (21 nm) pointing triangles. The red line represents a linear fit to the data[75] (c) Experimental data for the change in pore conductance *Δ*G upon insertion of a dsDNA molecule, as a function of pore diameter. The solid lines are for a simple geometric model with cylindrical DNA in a cylindrical pore (green), and in a hyperboloid-shaped pore in two limits (purple and orange).[76] Figure (b) adapted with permission from [*Smeets, R. M. M.; Keyser, U. F.; Krapf, D.; Wu, M.-Y.; Dekker, N. H.; Dekker, C. Salt Dependence of Ion Transport and DNA Translocation through Solid-State Nanopores. Nano Lett. 2006, 6 (1), 89–95*] Copyright (2020) American Chemical Society

Chapter 3

Electrophoretic Capture of DNA by Nanopore

Under an applied bias, the successful capture and translocation of a molecule has been observed[79,83] and described[45,46,84,85] using the following steps: i) A molecule freely diffuses to a distance r^* away from the pore, termed the capture radius ii) The molecule is brought near the pore mouth through drifting motion induced by the attractive non-uniform electric field, inducing stretched polymer configurations iii) The molecule randomly finds a configuration which allows an end or a segment along its length when the pore can accommodate folding, to penetrate into the pore and begin translocation iv) The molecule fully translocates through the nanopore. The capture process is generally believed to depend primarily on electrophoretic and thermal forces present in the system and on how analytes of interest react to such forces. Electro-osmotic flow, electrostatic interactions and other considerations are typically deemed insignificant. The following sections describe forces and the resulting capture rates that arise in nanopore systems. The theory of such processes is presented and compared with published experimental data.

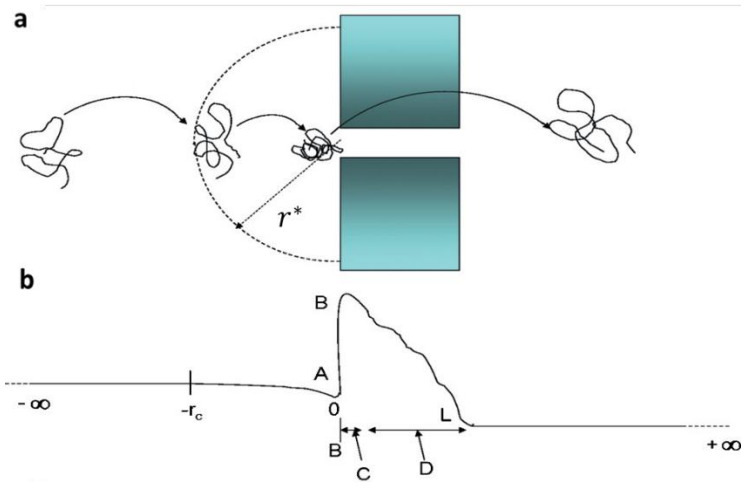

Figure 19. (a) Main stages of polymer capture and translocation process (b) Free energy landscape.[48]

3.1 Transport Properties of double stranded DNA

The diffusion of double stranded DNA in free solution has been reported as following Zimm dynamics, where polymers are not described as free draining.[86,87] The diffusion coefficient for Zimm dynamics is given by:

$$D(L) = \frac{k_B T}{6\pi\eta R_H(L)} \tag{7}$$

where k_B is the Boltzmann constant, T is temperature, η is the solution viscosity and $R_H(L)$ is the hydrodynamic radius of the DNA of length L. A scaling of $R_H \sim L^{\nu_F}$ is expected, where ν_F is the Flory coefficient ($\nu_F = 3/5$), for important excluded volume interactions. The L-scaling of Equation 7 has been obtained experimentally[86] through the use of free-solution capillary electrophoresis and resulted in a scaling of $D \sim L^{-0.57}$ as shown in **Figure *20***a, neighboring the theoretical Flory coefficient of 0.6. It was further shown that the diffusion coefficient is independent of the DNA sequence and of the presence or absence of electric fields.[86]

Although DNA acts as a non-free-draining polymer for thermal forces, it acts as a free-draining molecule in response to electric fields. This interpretation comes from the fact that DNA electrophoretic mobility, μ_e, is length independent.[46,84,88–90] More precisely, this is due to the mobile counterions transferring viscous drag to the backbone of the molecule. Since these hydrodynamic forces decay rapidly, the coupling between counterion-induced drag and electrophoretic pull on the charged backbone is said to be attained locally, on small subsections of the polymer. For this reason, the electrophoretic mobility of dsDNA is length-independent for strands longer than a few hundred base pairs. This is shown in **Figure *20***b where it can also be seen that the mobility of shorter strands deviates slightly from their longer counterparts.[88] Note that since the electrophoretic mobility depends on the interaction of the polyelectrolyte and its

counterions, the counter-ionic species and concentration has been shown to also highly impact the DNA electrophoretic mobility.[91,92]

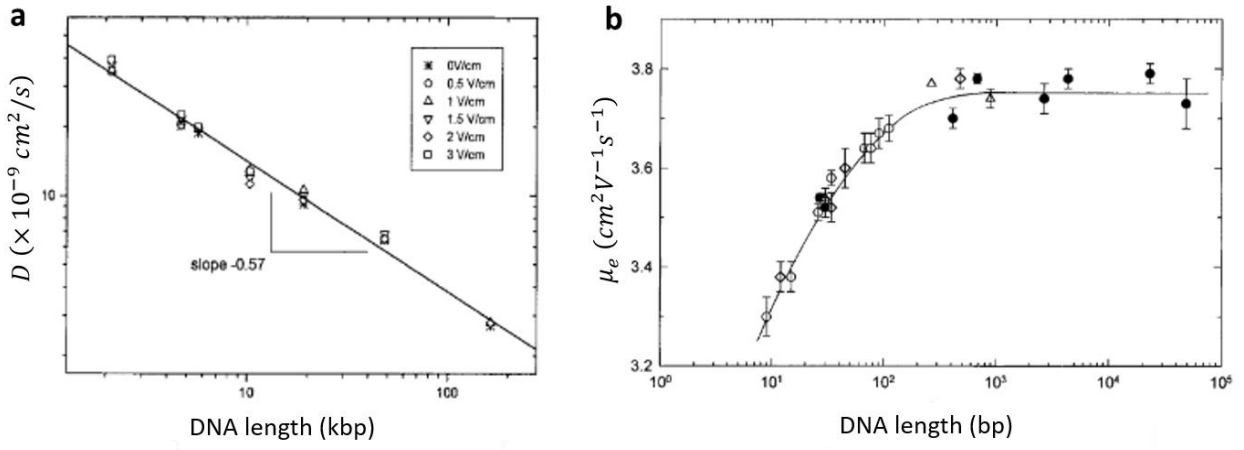

Figure 20. (a) Diffusion coefficient vs. dsDNA lengths (in base pairs). The slope (–0.57) indicates a Zimm's scaling for all molecular lengths.[86] (b) Dependence of the electrophoretic mobility of DNA in TAE buffer on the logarithm of DNA molecular weight, in bp. (●) Monodisperse DNA fragments from various sources; (○) fragments in the *Msp*I digest of pBR322; (◊) fragments in the *HpH*I digest of pBR322; (Δ) fragment in the *Taq*I digest of pUC19. The standard deviation of each of the values is indicated. The horizontal line represents the average electrophoretic mobility of the high molecular weight samples.[88]

3.2 Electrophoresis in Nanopore Systems

The motion of charged molecules through the electric field outside the pore has been observed and quantified experimentally[79,83] and is believed to be the main driving force behind the capture process. The drift velocity of charged molecules in electric fields is related to the field strength through the simple relationship $v_E = \mu_e E$, where μ_e is the aforementioned electrophoretic mobility and E is the electric field strength. For this reason, the nature of the electric field is primordial when discussing dynamics of nanopore capture. A few authors have derived expressions for the electric field responsible for such motion.[43–45,93,94] Although similar, some were obtained following questionable assumptions. For the sake of unbiasedness and clarity, the different equations are presented and compared here.

3.2.1 Spherically Symmetric Field Descriptions

In 2002, Nakane *et al.*[43] first postulated that the electric field far from the pore was responsible for the capture of charged molecules. Interestingly, they assumed the field near the nanopore was hemi-spherically symmetric and similar to the electric field in the proximity of a thin disc of charge:

$$E(r) \approx E_0 \left(1 - \frac{r}{\sqrt{r^2 + a_{pore}^2}}\right) \tag{8}$$

Here a_{pore} is the pore radius, r is the radial distance from the center of the pore, and E_0 is the electric field value as $r \ll a_{pore}$, analogous to $\frac{Q}{2\epsilon A}$ for infinite planes. They assumed for nanopores that E_0 could be defined as $\Delta V = \int_{-\infty}^{\infty} E dr = E_0(L_{pore} + d_{pore})$. Note that this implies that the voltage drop occurs entirely within the pore and two hemispheres of radius $d_{pore}/2$ at each end of the pore. Although this does not really support their proposed argument that the field far from the pore is responsible for capture, it gives a fair approximation that compares well to more recent results and observations shown further on:

$$E(r) \approx \frac{d_{pore}^2}{8L_{pore} + 8d_{pore}} \frac{\Delta V}{r^2} \tag{9}$$

In 2007 and onwards, a simple expression was derived[44,45,93] using Ohm's law $E = \xi/\sigma$, where ξ is the current density and σ the solution conductivity, combined with the assumption of hemispherical symmetry far away from the pore, implying $\xi = I/2\pi r^2$:

$$E(r) = \frac{G\Delta V}{2\sigma\pi r^2} \tag{10}$$

This simple relation first postulated by Gershow *et al.*[44] proved to be useful, as it turned out to be experimentally verifiable and validated by quantifying the drifting motion of stained (YOYO-1) DNA near nanopores.[83] Note that from Equation 10 the field dependence on pore geometry is entirely contained within the nanopore conductance term. In 2009, ensuing a complex and lengthy derivation, Wanunu *et al.*[45] derived a high salt electric field expression of the form:

$$E(r) = \frac{d_{pore}^2}{8L_{pore} + 4d_{pore}} \frac{\Delta V}{r^2} \tag{11}$$

The expression published in their main text was the simplified version of Equation 11 after assuming pores are of small aspect-ratio, that is $L_{pore} \gg d_{pore}$:

$$E(r) \approx \frac{d_{pore}^2 \Delta V}{8L_{pore} r^2} \tag{12}$$

Note that Equation 11 contains a minor inaccuracy. Instead of using the access resistance between a disk and a half spherical electrode, the resistance between two half spherical electrodes of radii $d_{pore}/2$ and $r \to \infty$ was used:

$$G_{acc}^* = \left[\int_{\frac{d_{pore}}{2}}^{\infty} \frac{dr}{2\sigma\pi r^2} \right]^{-1} = \pi\sigma d_{pore} \tag{13}$$

This interpretation of the access region electric field profile is incomplete, since it ignores the potential drop inside the hemisphere of radius $d_{pore}/2$ right above the pore, which is where most of the potential drop is located outside the pore.[95] This simple omission results only in a coefficient change when compared to the accepted access conductance expression[78] of:

$$G_{acc} = 2\sigma d_{pore} \tag{14}$$

Note that the derivation of Equation 14 is available in the following section, after the introduction of the proper mathematical foundation. Using the proper access conductance expression and the conductance equation for high salt conditions (ignoring surface-charge related terms in Equation 2), Davenport *et al.*[93] obtained:

$$E(r) = \frac{d_{pore}^2}{8L_{pore} + 2\pi d_{pore}} \frac{\Delta V}{r^2} \tag{15}$$

Note that even though previously introduced field expression were based on questionable assumptions, all equations presented are identical up to a single coefficient in the denominator, and all equations can be approximated by Equation 12, under the assumption of small aspect ratios.

3.2.2 Oblate Spheroidal Field Description

Although Equation 15 accounts for the proper access resistance, the assumption of hemispherical symmetry is clearly invalid near the pore where $E(r \to 0) \to \infty$. A proper electric field description in the nanopore access region should be described by calculating the field between a planar disk electrode at the pore mouth and a spherical electrode located at infinity, between which is applied a potential difference of amplitude ΔV_{access}. In 2013, a thorough solution, was described by Farahpour *et al.*[94] with the use of an oblate spheroidal coordinate system, as described in the following paragraphs.

Derivation

The oblate spheroidal coordinate system is defined by the coordinate transformation $(\mu, \nu, \phi) \to (x, y, z)$:

$$\begin{aligned} x &= a_{pore} \cosh\mu \cos\nu \cos\phi \\ y &= a_{pore} \cosh\mu \cos\nu \sin\phi \\ z &= a_{pore} \sinh\mu \sin\nu \end{aligned} \tag{16}$$

Here, a_{pore} is the pore radius. This coordinate system is used because of the similarities between its constant-μ surfaces and equipotential electrode surfaces described above. Constant-μ surfaces are described by oblate spheroids which follow equations of the form:

$$\frac{x^2 + y^2}{\cosh^2 \mu} + \frac{z^2}{\sinh^2 \mu} = a_{pore}^2 \tag{17}$$

For $\mu = 0$, the constant-μ surface describes a planar disk of radius a_{pore}, whereas for $\mu \to \infty$, the constant-μ surface describes spheres of radius $a_{pore} \cosh \mu$, describing the same surfaces as the electrodes previously introduced. This is because $\sinh \mu = 0$ for $\mu = 0$, and $\sinh \mu = \cosh \mu = e^{\mu}/2$, for $\mu \to \infty$, respectively. The potential field expression is therefore expected to depend on μ and be ϕ- and ν-independent. The potential profile is found by solving the Poisson equation, which requires developing the Laplace operator in curvilinear coordinates, expressed as:

$$\nabla^2 V = \frac{1}{h_\mu h_\nu h_\phi} \frac{\partial}{\partial \mu} \left(\frac{h_\nu h_\phi}{h_\mu} \frac{\partial V}{\partial \mu} \right) \tag{18}$$

Here h_μ, h_ν and h_ϕ are scaling factors defined as $h_u = \sqrt{\left(\frac{\partial x}{\partial u}\right)^2 + \left(\frac{\partial y}{\partial u}\right)^2 + \left(\frac{\partial z}{\partial u}\right)^2}$ for $u = \mu, \nu, \phi$. For oblate spheroidal coordinates, the scale factors are:

$$\begin{aligned} h_\mu &= h_\nu = a_{pore} \sqrt{\sinh^2 \mu + \sin^2 \nu} \\ h_\phi &= a_{pore} \cosh \mu \cos \nu \end{aligned} \tag{19}$$

Solving the Poisson equation with $V(\infty) = \Delta V_{access}$ and $V(0) = 0$ as boundary conditions results in a potential field expression of:

$$V(\mu) = \frac{2\Delta V_{acc}}{\pi} \tan^{-1}(\sinh \mu) \tag{20}$$

The expression for the electric field can then be found by calculating the gradient of $V(\mu)$:

$$E(\mu,\nu) = -\frac{1}{h_\mu}\frac{\partial V}{\partial \mu} = -\frac{2\Delta V_{acc}}{a_{pore}\pi \cosh\mu \sqrt{\sinh^2\mu + \sin^2\nu}} \tag{21}$$

Note, interestingly, that unlike the potential field, the electric field is not ν-symmetric.

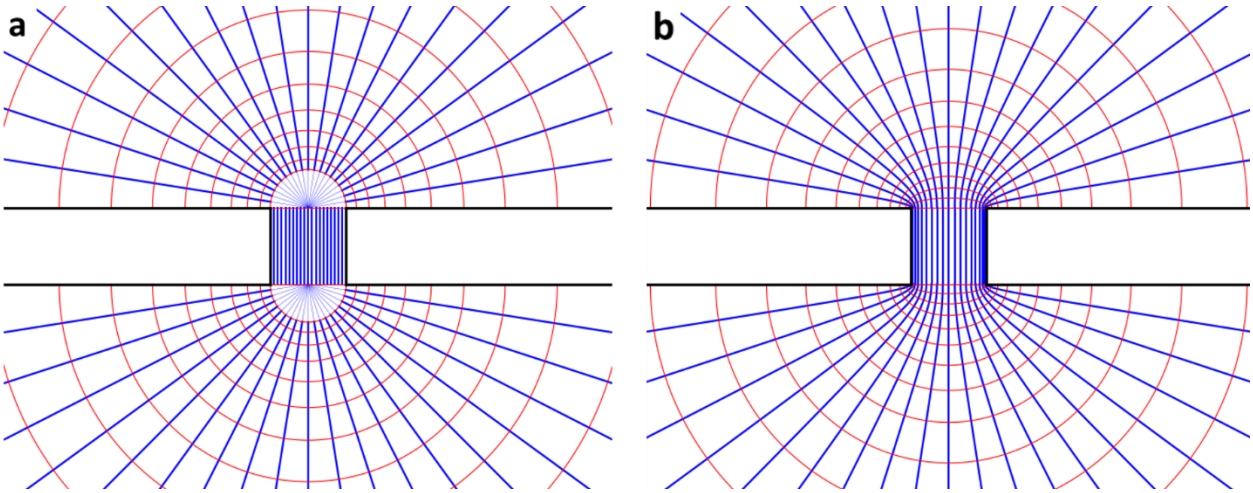

Figure 21. Analytical Electric field profiles, with (a) hemi-spherical description and (b) oblate spheroidal description. Electric field lines are shown in blue, whereas equipotential lines are shown in red.

Access Voltage and Resistance

To compare the oblate spheroidal electric field model with the hemi-spherical symmetric model, an expression for ΔV_{acc}, the potential drop across the access region, is needed. Since the nanopore system can be viewed as three resistors in series (a resistor for the cylindrical pore with two access resistors on either side), as previously described in Section 2.2, ΔV_{acc} can be expressed using a simple voltage divider equation:

$$\Delta V_{acc} = \frac{R_{acc}}{R_{eq}}\Delta V = G R_{acc}\Delta V \tag{22}$$

where G and R_{eq} are the system's equivalent conductance and resistance ($G^{-1} = R_{eq}$), R_{acc} is the access resistance and ΔV is the total applied voltage. Note that the full derivation of R_{acc} from first principles is difficult to find in publications or is obtained from arduous manipulations. Using

oblate spheroidal coordinates however, the access resistance can simply be calculated by integrating the current density, $\xi = \sigma E$, over equipotential surfaces to obtain the total current in the system, I:

$$\begin{aligned} R_{acc}^{-1} &= \frac{I}{\Delta V_{acc}} \\ &= \frac{\int_0^{2\pi}\int_0^{\frac{\pi}{2}} \sigma E\ h_\mu h_\nu d\nu d\phi}{\Delta V_{acc}} \\ &= \frac{\int_0^{2\pi}\int_0^{\frac{\pi}{2}} \sigma \left(-\frac{1}{h_\mu}\frac{\partial V}{\partial \mu}\right)\ h_\nu h_\phi d\nu d\phi}{\Delta V_{acc}} \\ &= -\frac{\sigma a_{pore}}{\Delta V_{acc}} \int_0^{2\pi}\int_0^{\frac{\pi}{2}} \left(\frac{2\Delta V_{acc}}{\pi}\frac{\cosh\mu}{1+\sinh^2\mu}\right)\cosh\mu\cos\nu\ d\nu d\phi \\ &= 4\sigma a_{pore} \end{aligned} \tag{23}$$

The potential drop across a nanopore access region is therefore:

$$\Delta V_{acc} = G R_{acc} \Delta V = \frac{G\Delta V}{2\sigma d_{pore}} \tag{24}$$

Comparison with Spherical Symmetric Expressions

Inserting Equation 24 in the electric field expression (Equation 21) results in:

$$E(\mu,\nu) = \frac{G\Delta V}{2\sigma\pi a_{pore}^2 \cosh\mu \sqrt{\sinh^2\mu + \sin^2\nu}} \tag{25}$$

To compare this solution to the hemi-spherical symmetric solution (Equation 10), Equation 25 is evaluated far away from the pore ($r, \mu \to \infty$), where $\sinh\mu \approx \cosh\mu \to e^{\mu}/2$ and $\sinh\mu \gg \sin\nu$:

$$E(\mu) = \frac{G\Delta V}{2\sigma\pi a_{pore}^2 \cosh^2\mu} \tag{26}$$

The relationship between radial distance from the pore, r, and oblate spheroidal coordinates can be established from the Euclidean distance definition $r^2=x^2+y^2+z^2$ which far from the pore yields:

$$r^2 = a_{pore}^2[\cosh^2\mu\cos^2\nu + \sinh^2\mu\sin^2\nu\,] \approx a_{pore}^2\cosh^2\mu \tag{27}$$

Substituting Equation 27 into the denominator of Equation 26 results in

$$E(r) = \frac{G\Delta V}{2\sigma\pi r^2} \tag{28}$$

Interestingly, this expression is completely equivalent to the one derived from basic hemi-spherical-symmetry arguments (Equation 10). In order to further compare both field models, the equipotential and electric field lines of both models can be observed in **Figure *21***, where similarities far from the pore are obvious between both types of surfaces. This observation validates using the simple hemispherical-symmetric field expression for studying the capture process, instead of the more complex curvilinear model.

3.3 Thermal Forces

Thermal forces, result on average in molecules diffusing away from the pore, as will be shown. From this radial thermal motion, it is possible to define a radial ensemble diffusion velocity associated to this process:

$$v_D \sim \frac{D}{r} \tag{29}$$

An overly simple way to find this radial scaling is to define the radial velocity as $v_D = \Delta r/t$, where Δr is the distance away from the pore over which the molecule diffuses over a time t. Inserting the expression for the time required for a molecule to diffuse over a distance Δr, $t = \Delta r^2/6D$, results in the previously mentioned radial diffusion velocity scaling. Note however, that this simple

derivation does not yield a preferred diffusion direction. A more thorough derivation of v_D has been described by Gershow *et al*,[44] which consists in calculating the instantaneous rate of change of the molecule's distance from the pore, assuming a known initial distance at time *t*, *r*(*t*):

$$v_D(r) = \lim_{\Delta t \to 0} \frac{\langle r(t+\Delta t)\rangle - r(t)}{\Delta t} \tag{30}$$

In order to find an expression for v_D, the expected radial distance after diffusing for a duration of Δt, $\langle r(t+\Delta t)\rangle$, must be evaluated. Using a spherical coordinate system centered at *r*(*t*) with its z-axis aligned with $\vec{\boldsymbol{r}}(t)$ as shown in **Figure *22***a, *r*(*t*+Δ*t*) can be expressed as:

$$r(t+\Delta t) = \sqrt{r(t)^2 + \rho^2 + 2r(t)\rho\cos\theta} \tag{31}$$

The expected value of *r*(*t*+Δ*t*) for Δ*t*→0 is calculated through the diffusion probability density:

$$\begin{aligned}
\langle r(t+\Delta t)\rangle &= \int_0^{\pi}\int_0^{2\pi}\int_0^{\infty} d\rho d\theta d\phi \rho^2 \sin\theta \sqrt{r(t)^2+\rho^2+2r(t)\rho\cos\theta}\,(4\pi D\Delta t)^{-\frac{3}{2}} e^{\frac{-\rho^2}{4D\Delta t}} \qquad (32)\\
&\approx \frac{2\pi r(t)}{(4\pi D\Delta t)^{3/2}}\int_0^{\pi}\int_0^{\infty} d\rho d\theta \sin\theta\left(\rho^2 + \frac{\rho^4}{2r(t)^2} + \frac{\rho^3}{r(t)}\cos\theta\right) e^{\frac{-\rho^2}{4D\Delta t}}\\
&= \frac{4\pi r(t)}{(4\pi D\Delta t)^{3/2}}\int_0^{\infty} d\rho\left(\rho^2 + \frac{\rho^4}{2r(t)}\right) e^{\frac{-\rho^2}{4D\Delta t}}\\
&= \frac{4\pi r(t)}{(4\pi D\Delta t)^{3/2}}\left[\frac{\pi^{1/2}}{4}(4D\Delta t)^{3/2} + \frac{3\pi^{1/2}}{16r(t)^2}(4D\Delta t)^{5/2}\right]\\
&= r(t) + 3\frac{D\Delta t}{r(t)}
\end{aligned}$$

This calculation confirms that molecules indeed tend to diffuse away from the pore, as previously mentioned. Note that for the derivation to be accurate $r(t)$ is assumed to be bigger than the expected diffusion distance, or $r(t) \gg D\Delta t$, which is expected to hold since $\Delta t \to 0$. Inserting $\langle r(t+\Delta t)\rangle$ in Equation 30 results in the radial diffusion velocity of scaling $v_D \sim D/r$, directed away from the pore.

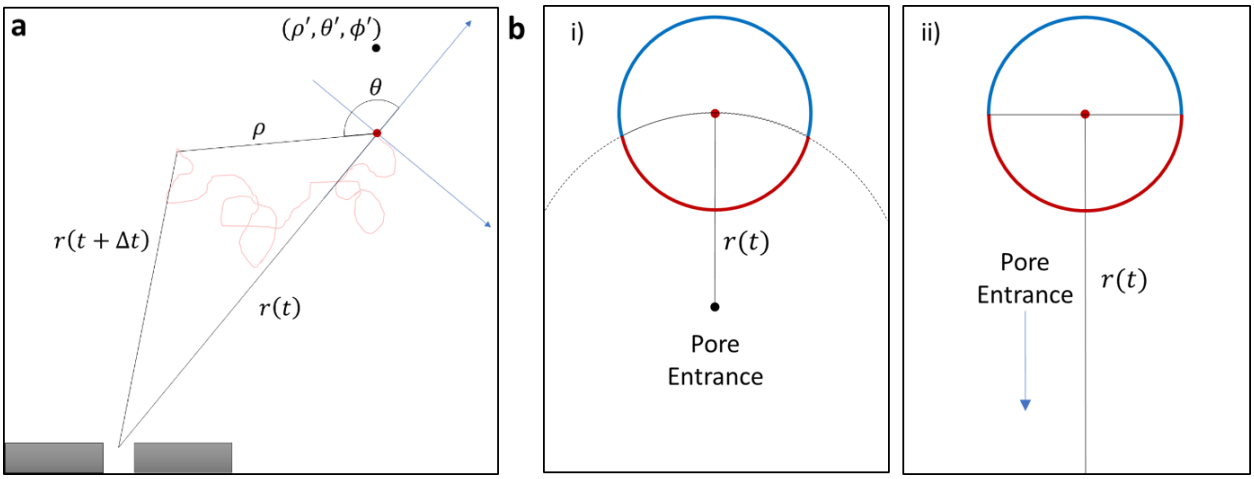

Figure 22. Schematics demonstrating radial diffusion concepts (a) Diffusion process with respect to the nanopore (b) The different coloured arcs represent the possible diffusion steps which bring the molecule closer (red) or farther (blue) than the initial distance r(t). i) and ii) show a finite and infinite initial distance from the pore, respectively.

To make sense of the $1/r$ scaling of radial diffusion velocity, which induces the counter-intuitive result that $v_D \rightarrow 0$ at infinity, one needs to consider that v_D is a measure of an ensemble radial velocity with respect to the pore entrance. To better visualize this, **Figure *22***b(i)-(ii) shows a schematic representation of finite-step 2D diffusion for molecules initially located at a distance $r(t)$ from the pore entrance. The circle around $r(t)$ represents the set of possible locations of the forthcoming step. For small or moderate initial distances, shown in i), more than half of possible steps are located at greater distances than $r(t)$. For this reason, on average, molecules are expected to diffuse away from the pore entrance. In the case where $r(t) \rightarrow \infty$, shown in ii), diffusing molecules are equally likely to be further away or closer to the pore entrance than they were at time t. The radial diffusion velocity at infinity is therefore expected to be null.

3.3 Experimental Capture Rate Observations

Nanopores are sensitive sensors due to their intrinsic single-molecule resolution. Translocation count or capture rate are important metrics used to determine concentrations of charged analytes. It was shown that in dilute solutions where inter-molecular interactions are negligible, the capture rate is constant in time and scales linearly with the analyte concentration.[96]

The random and independent arrival of molecules at the pore mouth follows a Poisson point process, as depicted in **Figure *23***. This means that the inter-event times, τ, follow an exponential probability density of the form:

$$P(\tau) = Je^{-J\tau} \tag{33}$$

Here, J is the capture rate, which has units of Hz. The capture rate can be extracted from fitting the distribution of inter-event times to Equation 33. Chapter 5 of this thesis expands on this idea and on various ways of extracting J under different non-ideal experimental conditions.

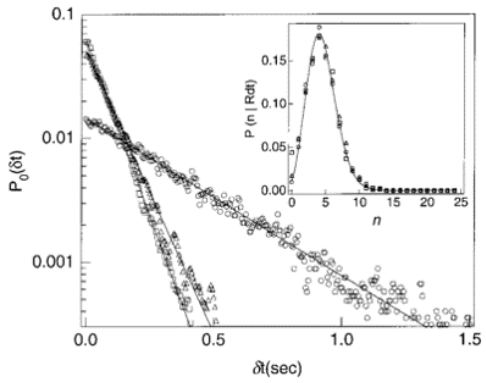

Figure 23. Normalized distributions of the elapsed time between successive capture events. Three polymer types and concentrations are plotted: (□) $(dA)_{20}$ at 2.3 μM; (Δ) $(dCdCdTdCdC)_6$ at 1.8 μM; (○) $(dC)_{40}$ at 0.5 μM. The elapsed time distributions were obtained by measuring δt for more than 5000 events for each polymer type. In each case, the distributions were normalized to the total number of events. For a large number of events, these distributions are proportional to the probability of having zero events in a time interval dt, denoted $P_0(\delta t)$. The solid lines are exponential fits that can be used to extract the event rate and its error. Inset: The same raw data was used to calculate the probability to observe n = 0, 1, 2 . . . events in a time interval dt.[96]

To understand the kinetics of capture, the dependence of capture rate on voltage was initially studied in biological pores.[43,97] An exponential voltage dependence was found for low field strengths (**Figure *24***a), whereas a linear voltage dependence was found for higher fields (**Figure *24***b). In solid-state nanopores, the same two regimes were found,[45,46,79,84,85] yet with bigger pore diameters being interrogated on average, it is not uncommon to observe mostly linear rate vs voltage curves, as seen in **Figure *24***c.

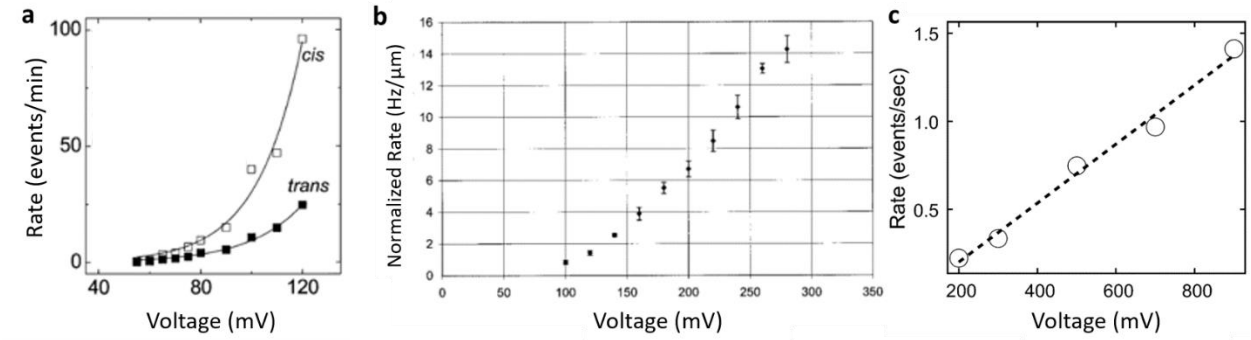

Figure 24. Capture rate dependence on voltage. (a) Exponential voltage dependence in biological pores (α-HL) for low voltages. At a given concentration, polymer added to the cis side is about six times more likely to transiently block the pore than when it is added to the trans side.[97] (b) Transition between exponential and linear voltage dependence in biological pore (α-HL).[43] (c) Linear voltage dependence in 15 nm solid-state nanopore.[79] Reprinted with permission from [*Chen, P.; Gu, J.; Brandin, E.; Kim, Y.-R. R.; Wang, Q.; Branton, D. Probing Single DNA Molecule Transport Using Fabricated Nanopores. Nano Lett. 2004, 4 (11), 2293–2298*] Copyright (2020) American Chemical Society

To the best of my knowledge, the dependence of capture rate on DNA length has been reported only twice experimentally in solid-state nanopores **Figure *25***a-b).[45,98] The capture rate depends non-linearly on DNA length for shorter strands, whereas it is DNA-length independent for longer strands. The dependence is once more split into two regimes. The nonlinear and linear regimes have been termed barrier-limited and diffusion-limited[45] (or drift-[84]) regimes, for reasons that will become apparent in the following sections.

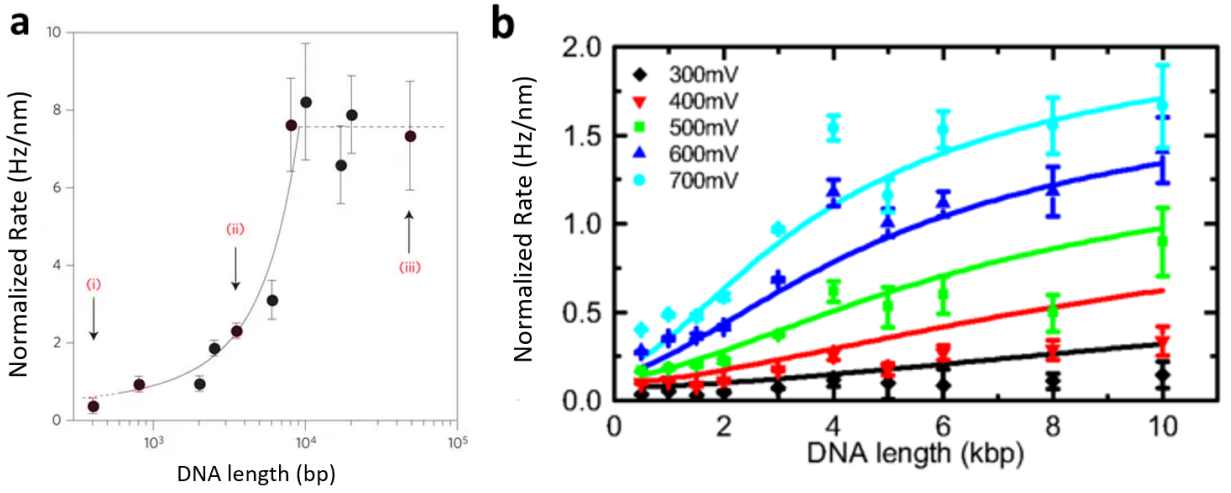

Figure 25. Capture rate dependence on DNA length. (a) Data from a ~3.5 nm pore with ΔV=400 mV in an electrolyte of 1M KCl.[45] (b) Experiment on a ~10 nm nanopipette with five different voltages used in an electrolyte of 4M LiCl. The trend lines show least-squares fits to the data using a 1D capture model.[98]

3.4 Theoretical Capture Rate Description

Most capture models assume that when applying a voltage across a nanopore, the capture process relies primarily on the balance between electrophoresis and thermal forces, arguing that dielectrophoretic forces are negligible due to low external fields (low voltage, small pores, etc.) and that electrostatic interactions and electro-osmotic forces can be ignored due to high salt concentrations shielding any surface-charge-related phenomena.[44–46,84,85] Both introduced capture regimes were initially modelled and described individually as separate processes. Although some generalized models[84,85] have been published, the individual descriptions give a good intuition on the subject and for this reason will be briefly described in the subsequent sections.

3.4.1 Barrier-Limited Regime

The exponential dependence on voltage was modeled as a Kramer (or Van't Hoff - Arrhenius) process, with the underlying principle being that for a molecule to begin translocating, it needs to surpass an energy barrier of entropic nature.[45,99] The rate of such process is described by the product of the attempt frequency and the probability of successful translocation and has the form:

$$J_{bar} = \omega_b \exp\left[-\frac{F_b - F_E}{k_B T}\right] \tag{34}$$

Here, ω_b is the attempt frequency, F_b is the energy barrier height and F_E is the electrostatic free energy of the charged molecule in electric field *E*. Note that $F_E \propto \Delta V$ explains the exponential dependence on voltage. Attempts at further deriving Equation 34 to find the dependence of J_{bar} on DNA length have been made but were later found to be erroneous due to self-declared incorrect

assumptions regarding the suppression of electro-osmotic flow through the DNA coil when it came to the proximity of the membrane.[45,46,85,89]

3.4.2 Diffusion-Limited Regime (Drift Regime)

Note that two nomenclatures, diffusion-limited regime and drift regime, are used in literature to describe this capture regime. The reason for both names will become apparent as discussion on this regime progresses. Contrary to the barrier-limited regime, in the diffusion-limited regime entropic barriers are expected to be negligible.[43,45,46,84] This is due in part to the higher voltages, i.e. electric fields, used when in the diffusive regime. Going back to the step-by-step description of the capture process (**Figure *19***), without a significant rate-limiting energy barrier at the pore entrance, the translocation frequency is equivalent to the rate at which molecules diffuse into the capture radius r^*. Such problem, diffusion into an absorbing hemisphere, has a well-known steady-state solution of:[45]

$$J_{diff} = 2\pi D r^* c \tag{35}$$

To relate the capture rate to voltage and DNA length, an expression for r^* is needed. One of the simplest way of estimating r^* consists in finding the distance at which the electrophoretic pull is countered exactly by the radial diffusive velocity, that is $v_E = v_D$.[43,44] This results in an expression for the capture radius of

$$r^* = \frac{\mu_e G \Delta V}{\sigma 2\pi D} \tag{36}$$

Here the expressions $v_E(r) = \mu_e E(r)$ and $v_D = D/r$, as derived in previous sections, are used for the electrophoretic and radial diffusion velocity. Note that different derivations and interpretations of r^* have previously been reported, most resulting in identical expressions to Equation

36.[43,45,46,85]. Inserting r^* in the hemisphere absorption equation (Eq. 35) results in a steady-state capture rate expression of

$$J_{diff} = \frac{\mu_e G \Delta V}{\sigma} c \tag{37}$$

Note how for DNA this corresponds qualitatively to the properties of the diffusion-limited regime observed experimentally. Translocation frequency is linearly dependent on voltage and independent on DNA length ($\mu_e \propto L^0$).

3.4.3 Generalized Solution

Two commonly used generalized capture solutions have been developed.[84,85] Both start by analyzing the net molecular flux of molecules, *j*, through a diffusion-convection equation:

$$j = -D\nabla c(r) + c(r)v \tag{38}$$

Here, v is the net velocity of molecules, which arises from external forces and local gradients in the free energy landscape. Note that the molecular flux (j) and capture rate (J) are related through $J = \int_S j \, dA$, where dA is the infinitesimal of a surface S.

1-D Convection-Diffusion Model

In 2010, Muthukumar was the first to attempt a general description of the capture rate process in order to match theory and experiment.[84] To achieve this, the capture and translocation process was mapped to a 1-dimensional process, and the net velocity term was expanded into an electrophoretic contribution and a free-energy barrier term:

$$j(x) = -D\frac{\partial c(x)}{\partial x} - \mu_e c(x)\frac{\partial V}{\partial x} - \frac{Dc(x)}{k_B T}\frac{\partial F}{\partial x} \tag{39}$$

Here, F, is the free-energy barrier of entropic nature, which a polymer must surpass in order to translocate. Using this 1-dimensional model, the steady-state capture rate can be found simply by integrating the equation across the nanopore from 0 to L_{pore}. Note that three regimes naturally come out of Equation 39: the diffusive, drift, and barrier regimes. Each regime is prominent when a single term of Equation 39 overpowers the two others. For example, in the drift regime, the second term overpowers the two others, resulting in the solution:

$$J = \frac{1}{L_{pore}} \int_0^{L_{pore}} j(x)dx = -\frac{\mu_e c_0 \Delta V}{L_{pore}} \tag{40}$$

Here, a constant concentration c_0 is assumed inside and outside the pore. Note the similarities with the previously introduced diffusion-limited regime: both are linearly dependent on voltage, and inversely proportional to membrane thickness. However, this drift regime does not include any diameter-dependence. Rearranging and integrating Equation 39 results in a general solution:

$$J = -D \frac{\left(c(L) e^{\tilde{F}(L) + \frac{\mu_e}{D} V(L)} - c_0 e^{\tilde{F}(0) + \frac{\mu_e}{D} V(0)} \right)}{\int_0^{L_{pore}} dx e^{\tilde{F}(x) + \frac{\mu_e}{D} V(x)}} \tag{41}$$

Here, $\tilde{F}$ is equivalent to $F/k_B T$. In order to compare this solution with experimental results, a simplistic energy barrier model was introduced with the barrier height and width left as fitting parameters, as seen in **Figure *26***a. Fixing the fitting parameters emulates the two experimentally observed regimes qualitatively through both voltage and DNA length dependencies, as shown in **Figure *26***b-c.

More recently, this 1-dimensional model was used to fit data acquired through a glass nanopipette with an effective sensing length of ~200 nm and a diameter of 10 nm.[98] The fits agree relatively well with the experimental data acquired using nanopipettes, as seen in **Figure *26***d-e.

Note that the voltage drop and electric field outside the pore are ignored in this model and so is the pore diameter due to the 1-D nature of the model. For this reason, nanopipettes or any high-aspect ratio pores are decent candidates to validate such model, since the electric field outside high-aspect ratio pores are insignificant, as demonstrated in **Figure *26***f. Whether this model also works on low-aspect ratio pores has yet to be tested.

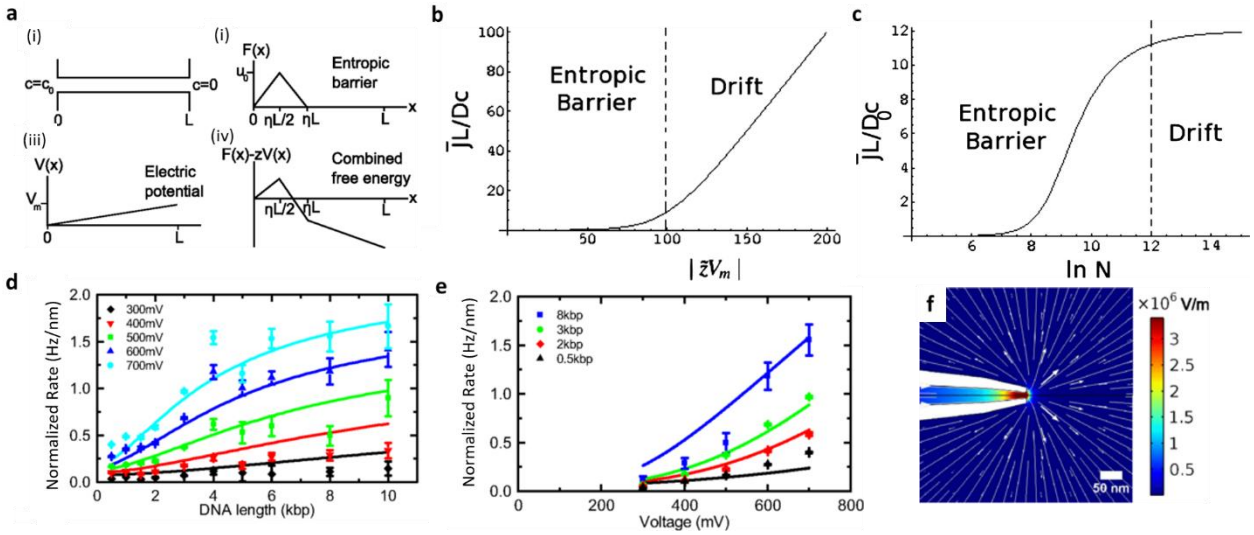

Figure 26. (a) (i) Modeled 1D geometry with length L, concentration c_0 in the sample reservoir and zero in the opposing reservoir. (ii) Triangular profile for the entropic barrier F(x) with height u_0. η parameterizes how far the barrier extends. (ii) The electric potential (V_m is the applied voltage) and (iv) combined free-energy profile for the nanopore where z is the effective DNA charge (b) Plot of scaled capture rate against the scaled voltage (c) and against the DNA length.[84] (d) Fitting of 1-D model to experimental nanopipette capture rate against DNA length (e) and voltage. (f) Finite-element analysis of the electric-field profile at a voltage of +600 mV. Lines represent tangents to the electric field.[98]

Smoluchowski Model

A few years after the 1-D model was derived, a different general solution was published which follows a Smoluchowski formalism.[85] This model makes use of hemispherical symmetry far from the pore to relate the molecule flux and capture rate, $j(r) = J/2\pi r^2$, and the linear relationship between capture rate and concentration, $J = R_c c$:

$$c(r)R_c = J = D2\pi r^2\left(\nabla c(r) + \frac{c(r)}{k_B T}\nabla F(r)\right) \tag{42}$$

Here, R_c is the normalized capture rate of units Hz/nM and $F(r)$ is the free-energy landscape, which combines contributions from the electrophoretic pull and the entropy of a DNA coil near a membrane. Equation 42 can be equipped with an absorbing boundary condition $c(r_b{\sim}l) = 0$, where l is the DNA persistence length, equivalent to absorption when a DNA end touches the pore. Solving for $c(r)$ results in:

$$c(r) = c_0 \frac{R_c}{2\pi D} e^{-\frac{F(r)}{k_B T}} \int_{r_b}^{r} e^{\frac{F(r')}{k_B T}} \frac{dr'}{r'^2} \tag{43}$$

An expression for R_c can be then be obtained by normalizing for the total number of particles in the system of volume V:

$$\frac{2\pi \mathrm{V} D}{R_c} = \int_{r_b}^{\infty} e^{-\frac{F(r)}{k_B T}} \left[\int_{r_b}^{r} e^{\frac{F(r')}{k_B T}} \frac{dr'}{r'^2} \right] dr \tag{44}$$

Much like the 1-D model, an expression for $F(r)$ must be found for an expression of J or R_c to be found. A qualitative description of the free-energy landscape is pictured in **Figure *27***a. Note that the energetic profile is 0 at infinity and contains a local minimum, $F(r) = -W(R_{coil})$, as it arrives at a distance R_{coil} of the pore, where R_{coil} is the coil size. Within R_{coil}, as a DNA end finds the pores mouth, a molecule obtains an energetic gain $W_p(r)$ and suffers an entropy cost $S_p(r)$. The free energy landscape is therefore represented as:

$$F(r) = -W(R) - TS_p(r) - W_p(r) \tag{45}$$

Note here that the entropic cost S_p originates from introducing one DNA end into the pore and contains two entropic contributions: a conformational term, and a term related to the DNA end's orientational freedom, $S_p = S_p^{con} + S_p^{or}$. The work terms are calculated by integrating the stall force, defined as the force required to stall DNA against an electric field. Note that near the pore

surface, this required developing a model for the electrophoretic mobility of DNA in the non-uniform electric fields in the presence of a surface.[89] By doing so and including the described free-energy landscape in Equation 45, the two experimentally observed capture regimes naturally came out as two extremes of the generalized solutions:

$$R_c = \begin{cases} \beta_1 e^{\beta_2 \Delta V} L^{\alpha}, & L, \Delta V < L^*, \Delta V^* \\ \dfrac{\mu_e G \Delta V}{\sigma}, & L, \Delta V > L^*, \Delta V^* \end{cases} \tag{46}$$

Here, β_1, β_2 and α are scaling factors related to various experimental conditions and nanopore properties. L^* and ΔV^* are the DNA length and voltage at which there is a capture regime transition. The obtained models fit data well and interestingly show a DNA-length power scaling of $\alpha \sim 1$ (**Figure *27***b-c).

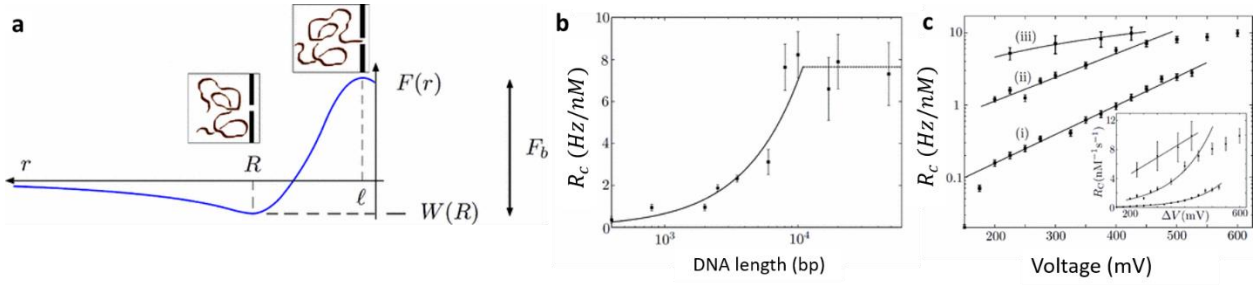

Figure 27. (a) DNA free-energy landscape F(r) in the barrier-limited regime as a function of the reaction coordinate r, set to be the position of the DNA end with respect to the pore. For r> R, where R is the DNA coil size, the free energy is solely determined by the coil's electrophoretic attraction and decreases to −W(R) as the coil is brought to a distance R from the pore. For r< R, and as one DNA end moves from within the coil toward the pore, the conformational and orientational entropy of the coil also contribute to the free energy; for the barrier-limited regime, this contribution results in an overall increase F_b in the free energy as the DNA end is brought from a distance ~R to ~l, which is the height of the free-energy barrier. The free energy begins to fall again for r < l, as of the the strong electric field inside the pore performs work on the DNA segments which pass through the pore. (b) Fitting of Smoluchowski model to experimental nanopore capture rate against DNA length (c) and voltage.[85]

Chapter 4

Precise DNA Concentration Measurements with Nanopores by Controlled Counting

Martin Charron, Kyle Briggs, Simon King, Matthew Waugh, Vincent Tabard-Cossa

Adapted with permission from [Charron, M.; Briggs, K.; King, S.; Waugh, M.; Tabard-Cossa, V. Precise DNA Concentration Measurements with Nanopores by Controlled Counting. *Anal. Chem.* **2019**, acs.analchem.9b01900.]

4.1 Introduction

In recent years, solid-state nanopores have gained significant attention as single-molecule sensors that can electrically detect a range of biological molecules, and as such are leading candidates to revolutionize existing biomolecular detection technologies.[34,100] By enabling real-time quantification of clinically-relevant concentrations of biomarkers with high sensitivity in a point-of-care format, nanopores are an ideal candidate to provide the next step towards precision medicine. While some studies have made progress towards this goal,[56,58–63,101–104] several key challenges remain before solid-state nanopores find application in clinical diagnostics. In particular, current nanopore-based methods of measuring molecular concentration are prone to high variability even in clean mock samples, which limit their performance as a precise and quantitative tool.

Most nanopore research to date has focused on DNA as the primary target molecule, since DNA is well-suited to the conditions in which solid-state nanopores function optimally. However,

many clinically relevant targets are proteins,[53–55,104–107]for which solid-state nanopore operating conditions must be tuned more carefully. Proteins are often incompatible with the high molarity salt concentrations preferred for a high nanopore signal, and their transport properties are more complex due to their low and non-uniform charge distribution, and their secondary and tertiary structures.[53–55] Even when proteins can be directly detected in nanopores, the translocation events are often too fast for the limited time-resolution available to conventional current amplifiers.[105] In contrast, DNA can withstand high molarity salt concentrations, and its high and uniform charge distribution allows for relatively simpler transport properties. As a result, many recent studies aimed at the detection of proteins and other biomarkers, from small molecules to viruses, have used linear or slightly modified linear DNA as a surrogate label or carrier for the actual target of interest.[56–63] This allows for more robust nanopore signals that are still representative of the actual target concentration, and in some cases permits multiplexed detection.[56,61,62,108–112] Distinguishable DNA-based proxy labels have also been shown to enable low-level multiplexing of nanopore measurements.[113] Given the recent progress in the design of DNA-based labels and in assay schemes that employ them, it is clear that a more consistent concentration measurement for DNA would translate directly to improved accuracy in the measurement of a wide range of clinically relevant biomarkers, including specific DNA sequences and modifications,[59,108,109,114–116] miRNA,[117,118] and proteins.[55,56,61,62,110,111,119]

The most commonly employed method for determining molecular concentration using nanopores is to measure the capture rate J, the frequency at which molecules translocate through the nanopore. J is extracted from the analysis of the nanopore current signal (**Figure *28***a) and can be obtained from either the slope of the cumulative single molecule counts as a function of time (**Figure *28***b), from the statistical analysis of inter-event times through calculating the survival

probably (**Figure *28***c), or by fitting the distribution of the log of inter-event times (**Figure *28***d). While these three methods yield the same answer in theory, and approximately the same answer in most practical cases, their actual performances in different situations are further described in detail in Chapter 5.

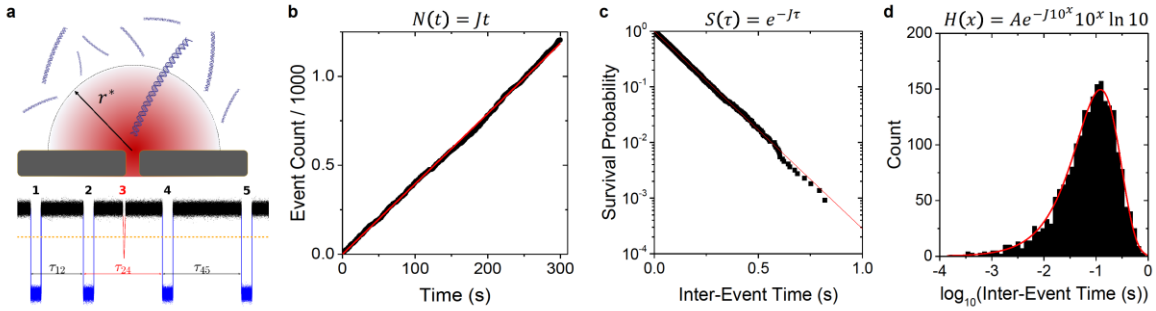

Figure 28. Methods to extract capture rate from nanopore data. **(a)** Schematic depicting the electrophoretic capture process and simulated current trace highlighting events correctly fitted by the analysis algorithm (blue) and ambiguous events (red), which are explicitly excluded from inter-event time statistics, as described in the Supporting Information section S1. **(b)** Fitting the slope of the cumulative single molecule counts as a function of time to extract the capture rate. **(c)** Survival probability method of extracting capture rate. **(d)** Fitting the distribution of the log of inter-event times to extract capture rate. In the equation above, x = $\log_{10}(\tau)$

In dilute solutions for which inter-molecular interactions are insignificant, capture rate is proportional to concentration c,[96] and is given by

$$J = R_c c \tag{47}$$

where the normalized capture rate R_c, depends on both the geometry of the nanopore sensor and the electrophoretic transport properties of the target molecule.[43,45,46,77,84,85,93,98] In theory, determining concentrations relies on establishing the value of R_c for a given nanopore system. This calibration is usually achieved by measuring J for a variety of concentrations, yielding a calibration curve which would in principle be valid for any identical nanopore under identical conditions. The precision of this method therefore relies on the ability to extract R_c from the resulting calibration curve, and on the ability to consistently fabricate nanopore devices with identical capture

properties and systematically operate them under identical conditions, which, as we show here, is simply not feasible under real-world conditions using state-of-the-art nanofabrication tools.

Here, we show that while electrophoretic capture theory describes capture rate properties qualitatively,[43,45,46,85,93,98] there are additional dependencies in real-world nanopore measurements which cause variations in the observed capture rate, not only between nominally identical pores (inter-pore variation), but also over time on a single nanopore (intra-pore variation). These variations can make it very difficult to extract the proportionality constant R_c and render straightforward counting techniques insufficiently precise for many applications.

There are numerous sources for this variability. While some can be controlled with varying degree of precision by the user, such as salt concentration (±2%), applied voltage (±1mV), nominal membrane thickness (±1 nm), and initial pore size (±1 nm), others are much less easily controlled, such as effective pore height, precise pore geometry, and pore size stability over the course of an experiment. Indeed, nanopores are often unstable in solution, growing slowly over time, which translates to a time-dependent normalized capture rate.[120] Even nanopores with identical conductance can have different geometries,[121–123] which affect the details of capture rate between nanopores that appear otherwise electrically identical. Furthermore, capture rate can also depend sensitively on the details of the membrane-electrolyte interface and on the presence of other molecules in and around the nanopore. Electro-osmotic flow induced by membrane surface charges has been shown to impact the capture and translocation properties of various charged molecules, in some cases hindering or completely preventing translocation.[124–127] Electrostatic interactions,[128] which are ignored in many capture rate models, could also contribute to forces felt by molecules as they approach the charged nanopore surface. Polymer-polymer electrostatic repulsion caused by molecules sticking to the membrane near the pore could give rise to changes

in both open pore conductance and capture rate. Since most of the issues on this non-exhaustive list of error sources are generally beyond the control of the user, they present themselves as systematic errors and drift in any measurements of concentration that relies on direct measurements of the nanopore capture rate.

Here we present controlled counting, a method that relies on simultaneously sensing a second molecular population of precisely known concentration, which acts as an internal calibrator with an easily distinguishable electrical signature. We show that the respective capture rates of both species are highly correlated, both in time and from pore to pore. This high correlation enables improved precision in concentration measurements through calculation of the ratio of capture rates of both populations. Doing so reduces the uncertainty and removes the need to employ pores with identical and time-invariant characteristics. While the use of internal standards is common practice in many analytical techniques to account for variations from run to run in the quantity of sample analyzed or in the instrument response, it is not *a priori* obvious that for the nanopore analysis tool a different length of linear dsDNA would be a suitable internal calibrator since it is unknown whether or not the uncertainties in nanopore capture rates have any DNA length dependence. In this work, we experimentally demonstrate conditions in which the variability in the nanopore capture rate of linear dsDNA does not vary with polymer length, and verify that linear dsDNA is therefore an appropriate internal calibrator for quantitative concentration measurement.

4.2 Experimental Section

Nanopore Fabrication

Nanopores are fabricated using controlled breakdown (CBD)[38] in 10 nm thick SiN_x membranes purchased from Norcada Inc. (NT005Z and NPBX5004Z). In cases where high bandwidth recording is necessary, chips are painted with polydimethylsiloxane (PDMS) prior to

sensing in a custom millifluidic flow cell in order to reduce device capacitance.[129] Just prior to mounting, chips are plasma cleaned using 20 W air plasma for 30 s. CBD is carried out in 1 M potassium chloride (KCl) buffered with 10 mM 4-(2-hydroxyethyl)-1-piperazineethanesulfonic acid (HEPES) at pH 8, controlled using custom hardware and LabVIEW software. Pores are subsequently grown to the desired size using square pulses at ±3 V with an 8 s period. Pore size is measured in 1.8 M lithium chloride (LiCl) pH 8 buffered with 10 mM HEPES by fitting the conductance *G* obtained from a standard I-V curve to the widely used equation[76]

$$G = \sigma \left[\frac{4L_{pore}}{\pi d_{pore}^2} + \frac{1}{d_{pore}} \right]^{-1}, \tag{48}$$

where σ is the electrolyte conductivity, L_{pore} the effective pore height, and d_{pore} the pore diameter. Note that L_{pore} is calculated for every pore from the first (unfolded) blockage level of linear dsDNA translocation.[130]

Nanopore Sensing

DNA molecules are pre-mixed to the desired concentration after measurement of their concentration using a spectrophotometer (Biotek Epoch 2). Capture rate measurements of linear dsDNA were performed in 1.8 M LiCl pH 8, buffered with 10 mM HEPES, using 300 mV unless otherwise noted. Time-series current recordings were obtained using both the Axopatch 200B (for long molecules) and the Chimera VC100 (for short molecules). Data are sampled using these two systems at either 500 kHz or 4.167 MHz, respectively, using the full bandwidth available for each instrument.

Capture Rate Analysis

Data analysis is performed using a custom implementation of the CUSUM+ and adept2state algorithms[131,132] (https://github.com/shadowk29/CUSUM) in order to extract inter-event times for use in capture rate analysis.

To optimally extract a capture rate from a nanopore current trace, every significant deviation from baseline current is numbered and identified as a potential translocation event. When multiple DNA populations are present, their respective events are separated according to their equivalent charge deficit (ECD), which is simply a measure of the area between the blocked current and the baseline. After filtering out undesired or ambiguous events (too short, too long, collisions, bad fits, *etc*.) the capture rate is calculated using only the subset of inter-event times bounded by consecutively indexed potential events which pass all of the quality control filters. As long as no systematic bias exists in the quality control filters, this procedure limits the effect of poorly analyzed current traces on the extracted capture rate.

Capture rate is obtained by one of three methods: i) by using the survival probability of the open-pore state to estimate inter-event times (cumulative distribution function of the inter-event time distribution), ii) the histogram of the logarithm of the inter-event times (probability density of the inter-event times), or finally iii) by counting the total number of single-molecule events and normalizing by the duration over which they were captured. The first method requires fewer data points to give a reasonable estimate of capture rate, but is sensitive to small numbers of outliers, whereas the second method is insensitive to outliers but requires more comprehensive statistics to be useful and can mask artefacts in the data. Simple counting is the most robust method but is generally more difficult to apply in practice since stretches of data may contain clogs or other effects that render sections of data unusable, making the normalizing time difficult to estimate. In

cases where the capture rate is varying in time, only the direct counting method is reliable, as both inter-event time fitting methods are distorted by time-variation in the capture rate. All of these fits give the same result when the data set is well-behaved (time-constant capture rate and all data usable). See Chapter 5 for a more detailed discussion of methods for analyzing capture rate.

4.3 Results and Discussion

4.3.1 Physics of Nanopore Capture Rate

The details of molecular capture rate through nanopores under electrophoretic driving force are complex, and consequently only a few experimental[44,53,79,93,97,98,133] and theoretical[43,45,46,84,85,134] studies on the subject have been published to date. In this section, we briefly review the generally agreed upon theoretical framework for the electrophoretic nanopore capture process, which we will show describes the behavior of real-world nanopores only qualitatively.

Applying an electric potential difference across a nanopore induces an electric field distribution inside and outside the pore, resulting in a field gradient with an approximately spherically symmetric inverse square dependence on radial distance from the pore (**Figure *28***a). Combining Ohm's law, and hemispherical symmetry,[44,45,93] the electric field outside the pore is well approximated by:[83]

$$E(r) = \frac{G\Delta V}{2\sigma\pi r^2}, \tag{49}$$

where $G = G(d_{pore}, L_{pore}, \ldots)$ is the nanopore conductance which encodes all geometric information about the pore such as diameter d_{pore} and pore height L_{pore}, ΔV is the applied voltage, σ is the solution conductivity and r is the radial distance away from the pore mouth. The dependence of the electric field on the pore geometry and its surface properties arises entirely from the nanopore conductance term. Note that Equation 49 is valid only for distances from the pore $r > d_{pore}/2$. More

complex formalism exists for the field outside a nanopore[94] which agrees with Equation 49 in the limit where $r \gg d_{pore}$, as demonstrated in section 3.2.2.

Capture rate properties induced by such fields can be determined by solving the Smoluchowski equation using the electrostatic free-energy landscape induced by the fields as molecules approach the nanopore.[46,84,85,89] From the generalized steady-state solution, two capture regimes naturally emerge:

$$J = R_c c = \begin{cases} \dfrac{G\mu_e \Delta V c}{\sigma}; & L, \Delta V > L^*, \Delta V^* \\ \beta_1 e^{\beta_2 \Delta V} L^{\alpha} c; & L, \Delta V < L^*, \Delta V^* \end{cases}. \tag{50}$$

Here, the pore conductance G contains all of the pore geometry dependence in the first regime and β_1, β_2, and α are scaling factors related to various experimental conditions and nanopore properties in the second.[85] The first regime describes the capture of long molecules under high electric fields and is referred to as the diffusion-limited regime. The diffusion-limited capture rate is characterized by linear voltage dependence[43,79] and, in the case of linear dsDNA, is independent of polymer length.[45] This capture rate is analogous to the rate of molecules diffusing into an absorbing hemisphere.

The second regime describes the capture of short molecules under the influence of weaker electric fields and is referred to as the barrier-limited regime. Barrier-limited capture rate is characterized by an exponential voltage dependence[97] and, in the case of linear dsDNA, by a power scaling law with polymer length.[45,85] The barrier-limited regime is often approximated as a Kramer[45,46] (or Arrhenius[97]) process, which gives the rate at which particles overcome energy barriers, as derived in section 3.4.

Figure *29*a shows experimental data for the typical dependence of the normalized capture rate on dsDNA length. The barrier-limited regime is observed for small molecules, whereas length independence is observed for longer molecules in the diffusion-limited regime. The DNA length at which the two regimes cross is L^*, a value which depends on experimental parameters such as the strength of the attracting field and the pore geometry.[85] **Figure *29***b shows experimental data for the capture rate voltage dependence for the barrier-limited and diffusion-limited regimes for two different pores and molecules. The crossover voltage, V^*, like the crossover length, depends on pore size and dsDNA length, where stronger electric fields outside the pore (*i.e.* larger nanopores) and longer dsDNA result in smaller values of V^*.[85]

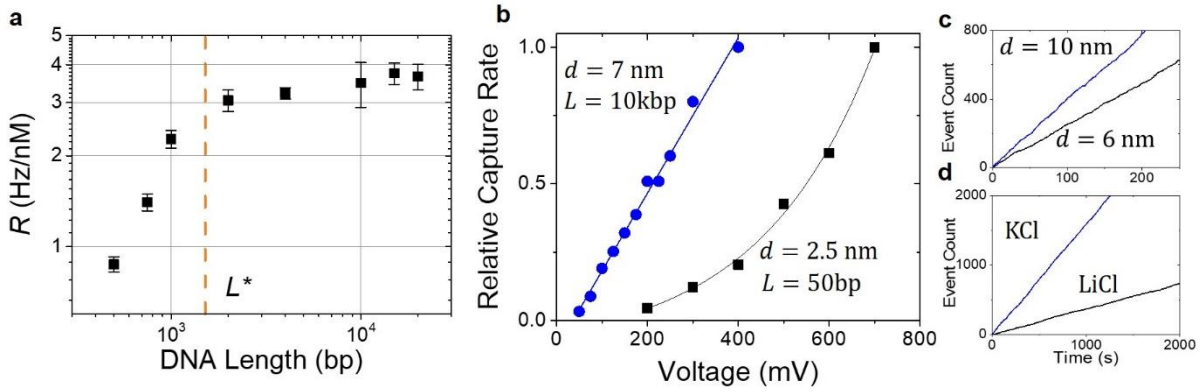

Figure 29. (a) Normalized capture rate versus dsDNA length for a 7 nm pore in 1.8 M LiCl pH8 at 300 mV. The orange vertical line shows a rough estimation of the capture regime transition. **(b)** Relative capture of 10 kbp dsDNA in a 7 nm pore in 1.8 M LiCl (blue circles) and 50 bp dsDNA in a 2.5 nm pore in 3.6 M LiCl (black squares), to highlight the qualitative voltage dependencies of barrier- and diffusion-limited regimes. **(c)** Number of 10 kbp dsDNA translocations as a function of time for a 6 nm nanopore (black) and a 10 nm pore (blue) at the same DNA concentration of 0.2 nM, under 300 mV bias. **(d)** Number of translocations as a function of time for 10 kbp in 1.8 M KCl (black) and 1.8 M LiCl (blue) at the same DNA concentration of 0.2 nM, under 200 mV bias

Since larger pore sizes result in stronger and more spatially extended electric fields outside the pore, they also exhibit higher capture rates for a given voltage. This is experimentally validated by the data in **Figure *29***c, for which the number of captured events versus time is shown for the same nanopore at two different diameters, obtained by enlarging the pore using high electric field

pulses.[37] As expected, the capture rate is higher after the pore is enlarged from 6 ± 1 nm to 10 ± 1 nm (2.5 Hz *vs.* 4.0 Hz).

The capture process depends not only on the electric field outside the pore, but also on how molecules respond to it. This response is encoded in the electrophoretic mobility μ_e, which originates from the local balance between the electrophoretic force and the viscous drag from counter-ions surrounding charged molecules. The mobility and capture rate therefore depend on experimental parameters such as temperature,[77] ionic concentration, and electrolyte type.[92,98] **Figure *29***d provides experimental data showing how sensitive capture rate is to ionic type by comparing the cumulative count of captured 10 kbp molecules versus time for the same 1.8M concentrations of LiCl and KCl. The higher capture rate measured in KCl (1.6Hz) than in LiCl (0.35Hz) is expected, since K^+ counter-ions are known to shield dsDNA less effectively than Li^+ counter-ions.[92,98]

This shows that a purely electrophoretic capture model suffices to explain the scaling dependencies of the capture rate on intrinsic (pore geometry, electric field) and extrinsic (temperature, salt concentration) experimental conditions. Extrinsic parameters are easily kept fixed for the duration of an experiment or from pore-to-pore, whereas intrinsic parameters are more difficult to control, as discussed above. According to this electrophoretic capture theoretical framework, translocation frequency and open-pore conductance are two manifestations of the same underlying mechanism and both phenomena result from the transport of charged molecules through an electric field whose profile depends primarily on the system geometry. Both capture rate and conductance are expected to vary within or across experiments in a highly correlated fashion, since $J \propto G$. In the following two sections, we address the intra- and inter-pore capture

variations and show empirically that capture rate and conductance do not always scale proportionally, due to experimental parameters which are beyond reasonable experimental control.

4.3.2 Intra-pore capture variations

We have observed that the capture rate J of a given nanopore can fluctuate over time during the course of a single experiment, even when efforts are made to tightly control relatively easily controllable parameters, such as temperature, evaporation (salt concentration) and applied voltage. We therefore attribute these fluctuations to variations in pore properties, which are generally much less controllable.

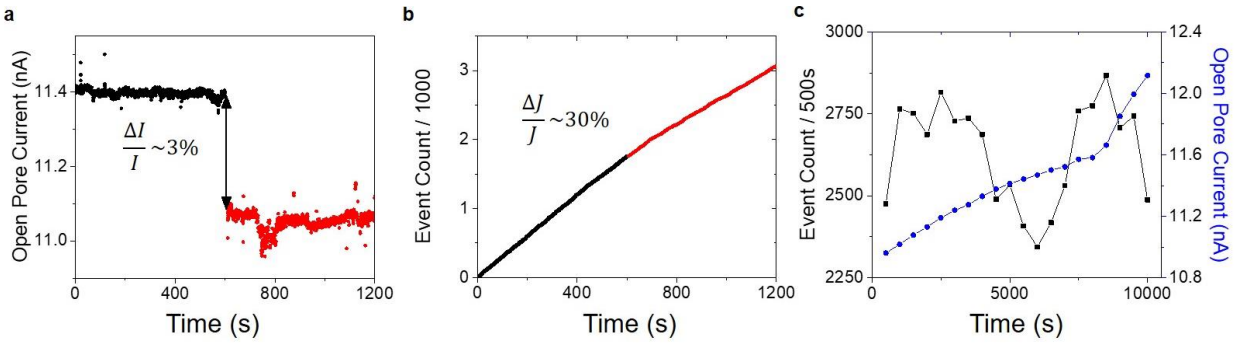

Figure 30. Visualization of intra-pore variations. **(a)** Open pore current baseline as a function of time for a 9 nm pore in 1.8 M LiCl pH8, at 300 mV showing an uncontrolled 3% drop around the 600 seconds mark. **(b)** Cumulative event number (single molecule counts) as a function of time, showing a sudden ~30% capture rate reduction of 10 kbp DNA correlated with the drop in (a). **(c)** Single molecule events count in 500 seconds bins versus time for 11 nm pore in 3.6 M LiCl pH8 at 200 mV, revealing up to 20% intra-pore capture variations for 1.5 kbp DNA during a ~3-hour experiment, with the drift in open pore current superimposed.

To highlight this intra-pore variability, **Figure *30***a shows the open pore current of a 6 ± 1 nm pore in 1.8 M LiCl at an applied voltage of 300 mV, over a ~20-minute timespan, capturing and translocating 10 kbp dsDNA. After 600 s of steady baseline, a ~3% (~350 pA) decrease in open pore current can be observed. This change is smaller than the expected blockage level from a dsDNA molecule under these experimental conditions (~850 pA). Instead of the expected 3% reduction in capture rate, the capture rate instead drops by ~30% (**Figure *30***b). Another illustration

of intra-pore fluctuation is presented in **Figure *30***c, which shows the event count in 500 second bins for an 11 nm pore detecting 250 bp dsDNA over a 3-hour experiment. In this example, a slow 20% capture rate variation can be observed throughout the experiment, weakly correlated to open-pore current variations.

4.3.3 Inter-pore capture variations

We have also observed that the capture rate for nanopores with similar conductance and seemingly similar geometry can vary significantly between pores, even when measured under identical experimental parameters. Because the normalized capture rate R_c of a given molecule under fixed external conditions (temperature, salt concentration, *etc*.) should depend only on pore geometry, nominally identical nanopores should have the same value of R_c. In practice this fails, for instance due to the fact that it is not generally possible to be certain that any two solid-state pores are geometrically identical even if they have the same conductance.[121–123]

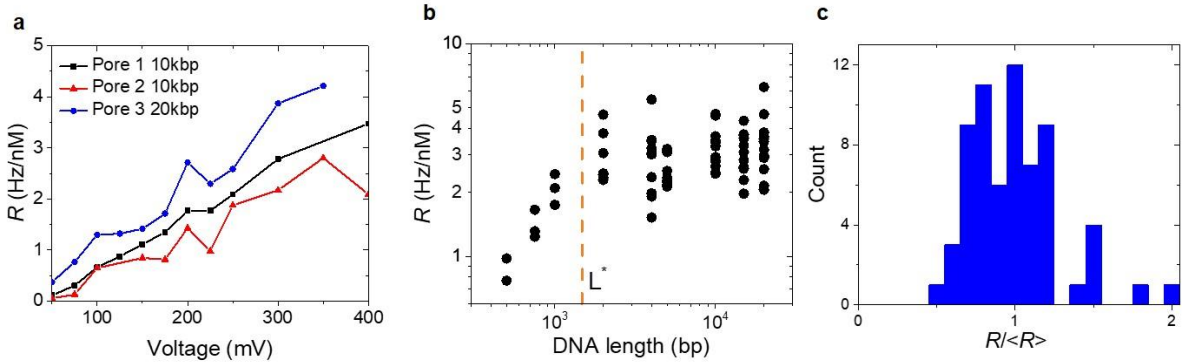

Figure 31. Visualisations of inter-pore variations. **(a)** Normalized capture rate of 10 kbp (red circles and black squares) and 20 kbp (blue triangles) as a function of voltage for three 7 nm nanopores in 1.8 M LiCl pH8. **(b)** Normalized capture rate versus DNA length in 1.8 M LiCl pH8 at 300 mV for 13 different nanopores of diameters 7 ± 1 nm and effective height 6 ± 1 nm. The orange vertical line roughly demarks the barrier- from the diffusion-limited regimes. **(c)** Distribution of diffusion-regime normalized capture rate data from (b). The mean normalized capture rate is 3.08 Hz/nM with a coefficient of variation of 29%

Figure *31*a shows the normalized capture rates as a function of voltage for three nanopores of similar diameters (7 ± 1 nm) and heights (6 ± 1 nm), all immersed in 1.8 M LiCl pH8. 10 kbp dsDNA was used for two pores (black square and red triangle), whereas 20 kbp was used for the third pore (blue circle). Both dsDNA lengths are in theory expected to have identical capture rates in the diffusion-limited regime. The observed capture difference between these pores is on the order of the capture rate itself. Note that intra-pore fluctuation is also observed on individual pores.

To further highlight this inter-pore variation, we performed 75 experiments using various lengths of dsDNA (500 bp – 20 kbp) using 13 distinct nanopores, all fabricated with the same diameter, d_{pore} = 7 ± 1 nm, and effective height, L_{pore} = 6 ± 1 nm. **Figure *31***b shows the normalized capture rates as a function of dsDNA length. This graph is similar to **Figure *29***a with an added vertical spread in the data, due to inter-pore variations. A histogram of the normalized capture rate distribution for all combined dsDNA lengths from the diffusion-limited regime (to the right of the vertical dash line in **Figure *31***b), where capture rate should have no dependence on polymer length, is shown in **Figure *31***c. A significant spread is observed, which corresponds to a 29% coefficient of variation (CV) for the 67-experiment subset in the diffusion-limited regime, using lengths of dsDNA ranging from 2 kbp to 20 kbp. Note that this variation does not appear to be caused by simple geometrical variations, since respective capture rates and open pore conductances are only weakly correlated (r = 0.33). To further validate that intrinsic pore variations are responsible for the capture variations, and not loosely defined experimental conditions or manipulations errors, the translocation times, τ_d, of the data in **Figure *31***b are plotted against their respective DNA length. Fitting the well-behaved data to a power law results in scaling coefficient of 1.22, consistent with previous work.[120,135,136]

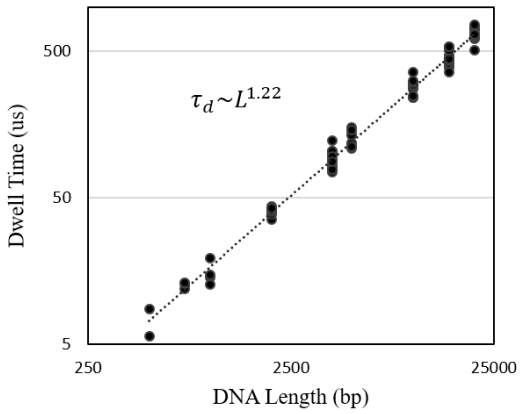

Figure 32. Scaling of translocation duration and DNA length in 1.8 M LiCl pH8 at 300 mV for 13 different nanopores of diameters 7 ± 1 nm and effective thickness 6 ± 1 nm. The dotted line is a power-law fit, resulting in a scaling constant of 1.22.

4.3.4 Controlled Counting

We propose a reliable and simple way to overcome uncontrolled capture rate variations in order to use nanopores for precise counting and concentration measurement purposes by using an internal calibrator to normalize away uncontrolled sources of variability in capture rates. To this end, we propose a qualitative reinterpretation of the capture rate expression:

$$J = R_c c = PQc. \tag{51}$$

Here, P is a function that depends solely on pore properties (diameter, height, geometry, surface charge density and distribution, *etc.*), and implicitly depends on time, whereas Q accounts for properties of the captured molecules (dimensions, electrophoretic mobility, diffusion coefficient, *etc.*) and experimental conditions (salt concentration, applied voltage, *etc.*). The two functions are defined such that Q is independent of the pore properties and is constant in time (under fixed experimental conditions), whereas each pore has a unique time-dependent P which encompasses the inter- and intra-pore capture variations. While this factorization is not necessarily possible for any target molecule, we demonstrate below that it is for the case of linear dsDNA used here, and

the method presented will be applicable to any target for which this factorization is valid, regardless of the exact functional form of *P* and *Q*.

Figure *33*a presents a schematic illustration of the proposed method, in which two distinguishable molecular species are simultaneously captured by the pore. In **Figure *33***b, we demonstrate that two DNA lengths can be easily distinguished by their equivalent charge deficit value (**Figure *33***b, inset), allowing extraction of capture rates for each species. **Figure *33***c shows the time evolution of translocation counts of a mixture of 250 bp and 1.5 kbp in 3.6 M LiCl at 200 mV in an 11 nm diameter, 13 nm long pore, which shows highly correlated intra-pore capture variations throughout the 3-hour experiment. This strongly supports the notion that intra-pore capture fluctuations originate from time-varying nanopore properties (*P*) and not from time-insensitive analyte properties (*Q*). Using the diffusion-limited regime capture rate data from 13 similar-conductance pores already presented in **Figure *31***b-c, in which every experiment involved a different mixture of two distinguishable dsDNA lengths, **Figure *33***d plots the normalized capture rates of each molecule type. A strong correlation is observed (r = 0.77). This suggests that if a molecule has a higher capture rate than expected due to systematic errors, other similarly charged molecular species present in the solution will also have a proportionately higher capture rate, supporting the validity of the proposed factorization. Note that when capture rate is time-varying as previously shown, it becomes an ill-defined quantity. Capture rates calculated for **Figure *33***d were extracted from short experiments (<20 minutes) during which no apparent capture variation was observed. Further discussion on quantifying time-varying capture rates is given above in the Experimental Section (Section 4.2) and in Chapter 5.

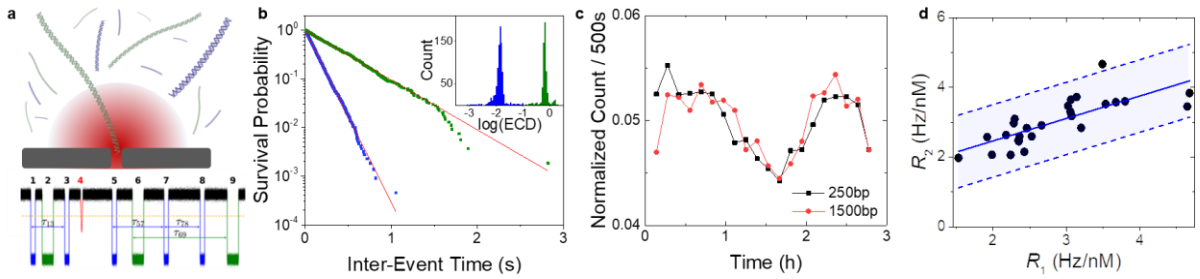

Figure 33. (a) Schematic of the controlled counting principle: capturing a target molecule of unknown concentration, while simultaneously capturing an internal calibrator molecule of known concentration, with distinguishable event characteristics. Simulated current trace highlighting single molecule events from each population, their indexation and intra-event times within each population. **(b)** An example of the population separation by equivalent charge deficit (ECD) and inter-event time fitting methods used to extract correlated capture rates for two molecular species in a mixture. **(c)** Correlated time-dependent capture variations of 250 bp and 1.5 kbp in 3.6 M LiCl pH8 at 200 mV by a pore, 11 nm in diameter with a 13 nm effective height. **(d)** Normalized capture rate correlations (r = 0.77) of two populations of molecules detected in mixture, in 1.8 M LiCl pH8 at 300 mV for 13 different nanopores of diameters 7 ± 1 nm and effective height 6 ± 1 nm, using the data in the diffusion-limited regime from Figure 32b. The coloured region shows the 95% prediction interval for the linear fit.

These correlations can be used to improve the precision of nanopore concentration measurements: if a second population of known concentration (the internal calibrator, c_{ic}) is present at the same time as the target (of unknown concentration, c_T), it can be used as an internal control by which the effects of uncontrolled pore properties are normalized. Since the capture rate of both distinguishable molecules depends on the same pore-specific function P at any time during an experiment, determining the unknown concentration of a target can therefore be simply achieved by calculating:

$$c_T = \frac{J_T}{J_{ic}} \frac{Q_{ic}}{Q_T} c_{ic}. \tag{52}$$

In order to validate the performance of the proposed controlled counting method, all data presented are again taken from the diffusion-limited regime presented in **Figure *31***b, a regime for which we expect $Q_{ic} = Q_T$.[85]

In order to verify the underlying assumption that in the diffusion-limited regime, capture is DNA length independent, **Figure *34***a plots the ratio of normalized capture rates, $r_J = \frac{J_T}{J_{ic}}\frac{c_{ic}}{c_T} = \frac{R_T}{R_{ic}}$, versus the DNA length ratio, L_{ic}/L_T. The recorded values are close to the expected value of 1, with no obvious sign of length dependence for a 10-fold change in DNA length ratio. Under this condition the concentration and capture rate ratios should be equivalent ($c_T/c_{ic} = J_T/J_{ic}$), **Figure *34***b displays the ratio of capture rates versus the ratio of concentrations of the two distinguishable DNA populations on logarithmic scales. A power law fit to the data yields a 0.88 ± 0.05 exponent value, close to the expected value of 1, for ratios of concentrations and capture rates spanning a range of 2 orders of magnitude. This slight deviation is likely due to small unaccounted-for time-variation in capture rate, for which mitigation strategies are discussed below.

We can quantify the improvement provided by the use of the controlled counting method for measuring the concentration of an unknown molecular target by measuring the coefficient of variation of r_J and comparing it to that of the data presented in **Figure *31***c, which represented a demanding attempt at controlling the pore properties to the limit of what can be experimentally achieved. **Figure *34***c shows the distribution of r_J, with a measured CV of 16%. This is a significant reduction from the previously observed 29% CV obtained when performing careful capture rate measurements without an internal calibrator. This reveals that the use of an internal calibrator of known concentration reduces the influence of the specific nanopore sensor in use, without the need to fully characterize its uncontrolled sources of systematic errors, which in turn allows more precise measurements of an unknown target concentration. Note also that this factor of 2 improvements involves a mixture of many internal calibrator lengths, some of which are near the crossover between the diffusion-limited and barrier-limited regimes, and further improvement can be expected when using a consistent calibrator well in the diffusion-limited regime every time.

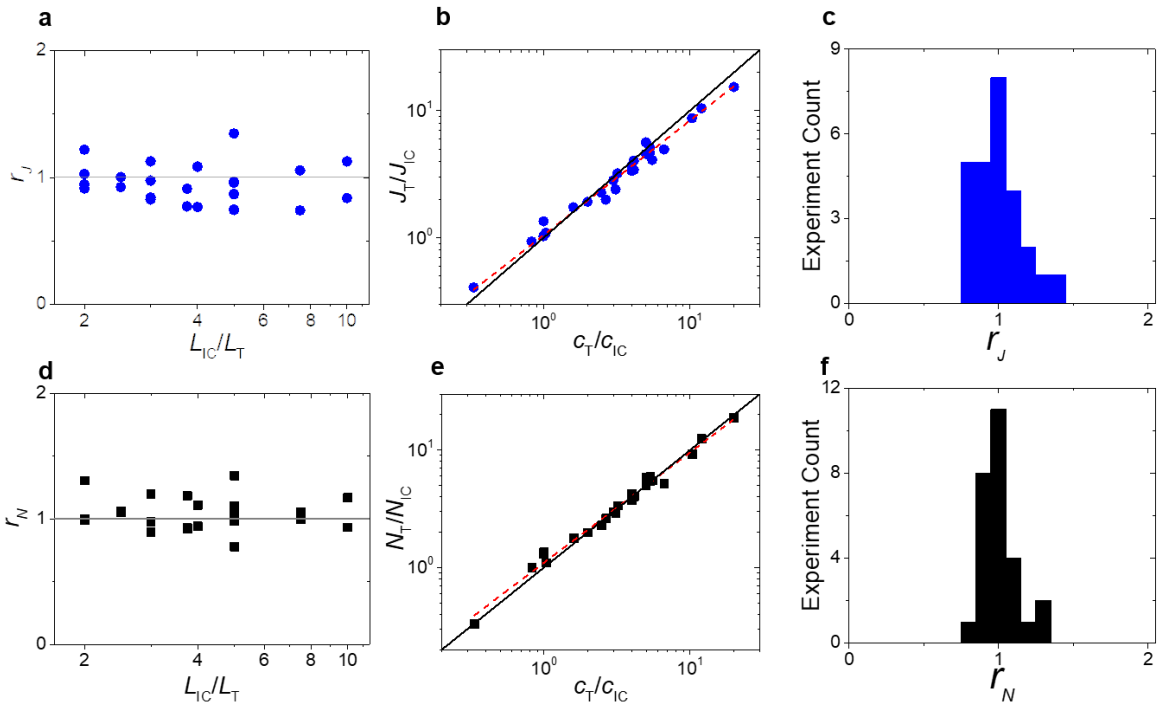

Figure 34. Validation of controlled counting principles using the capture of two distinguishable molecules in the diffusion-limited regime. **(a)** Ratio of normalized capture rates versus DNA length ratio. **(b)** Scaling of the capture rate ratio with concentration ratios. Power law exponent is 0.88 ± 0.05. The solid line shows the expected relation y=x. **(c)** Distribution of r_J the ratio of normalized capture rates, having a 16% CV. **(d)** Ratio of population counts versus DNA length ratio. **(e)** Scaling of the capture rate ratio with concentration ratios. Power law exponent is 0.94 ± 0.05. The solid line shows the expected relation y=x. **(f)** Distribution of r_N, the ratio of population counts normalized by the concentration ratios, having a 12% CV.

When significant intra-pore variations are present in an experiment, the capture rate becomes an ill-defined quantity (see Chapter 5). In this case, the calculation of capture rates by fitting inter-event times mistakenly assumes a constant R_c, resulting in the extraction of ill-defined capture rate values. Consequently, when the assumption of a constant R_c does not hold, it is preferable to use population count ratios (N_T/N_{ic}) over the full duration of the experiment instead of capture rate ratios (J_T/J_{ic}), since single-molecule counts integrate out variations in capture rate (see Chapter 5 for more details about this counting approach). To highlight this, the data in **Figure *34***a-c are replotted in **Figure *34***6d-f, using population count ratios instead of capture rate ratios. **Figure *34***d further validates DNA length independence in the diffusion-limited regime by displaying $r_N = \frac{N_T c_{ic}}{N_{ic} c_T}$ versus L_{ic}/L_T, showing no correlation between the ratios. **Figure *34***e shows

N_T/N_{ic} as a function of c_T/c_{ic}, fitted to a power law with an exponent of 0.94 ± 0.05, even closer to the expected value of 1. The distribution of r_N, in **Figure *34***f shows a further reduced coefficient of variation of 12%.

As already discussed, the most probable source of the increased coefficient of variation when using capture rate ratios instead of population count ratios lies in the fact that the capture rate can vary in time, adding additional uncertainty when a constant capture rate is assumed. Furthermore, the coefficient of variation can be further reduced when using only a single predetermined and premeasured internal calibrator instead of the range of calibrators used here. Because both r_J and r_N depend on four measured parameters, whereas the target concentration, c_T, calculated via Equation 52 depends only on three measured parameters for the case of linear dsDNA, the precision of concentration measurements made by this method will be further improved. Aside from the internal control concentration uncertainty, the fundamental limit of precision for the measurement of capture rate ratios is ultimately Poisson noise, decreasing with the inverse square root of the number of events used to calculate the ratio. Note also that the polymer length transition between the barrier- and diffusion-limited regimes is not as sharp as described by theory. Working with DNA lengths near that boundary will result in increased uncertainty, due to the underlying assumption that $Q_{ic} = Q_T$ for dsDNA, an assumption which will improve in the limit of $L/L^* >> 1$.

4.4 Conclusions

The popular electrophoretic capture model used to describe the capture of dsDNA by solid-state nanopores provides a picture of the capture process that is quantitatively incomplete. We have empirically shown that inter- and intra-pore fluctuations give rise to significant, poorly controlled variations in capture rate, which translate to large systematic errors in the determination of

molecular concentration. We demonstrate that these fluctuations are primarily due to variability in properties of the solid-state nanopore itself and are beyond what can reasonably be experimentally controlled. The observed fluctuations severely impact the precision of concentration determination based on simple capture rate measurements with solid-state nanopores, resulting in a coefficient of variation for capture rate which is unacceptably high for many applications, including diagnostics, which generally require a coefficient of variation below 20%.

The controlled counting method proposed here removes the influence of uncontrolled nanopore variations and dramatically reduces the uncertainty in extracted concentration measurements based on capture rates. This improvement in precision is achieved by decoupling the determination of target concentration from unpredictable nanopore properties, owing to the real-time capture rate calibration offered by the internal calibrator. Moreover, the proposed controlled counting method provides additional advantages to the measurement of concentration based on single-molecule nanopore sensing. On the level of an individual nanopore sensor, the method obviates the need to perform a time-consuming calibration curve for each nanopore in order to relate capture rate to concentration, and perhaps of greater technological importance, it eliminates any requirements for precise nanopore size and geometry or even geometric stability. Furthermore, across many nanopore sensors, the method reduces the error from inter-pore variations due to fluctuations in pore properties which are below the level of reproducibility achievable with state-of-the-art fabrication and measurement techniques.

Chapter 5

Extracting Capture Rates from Nanopore Data

5.1 Simulating Homogeneous and Inhomogeneous Poisson Processes

Homogeneous Poisson point processes are one-dimensional stochastic processes defined as points, or events, randomly and uniformly distributed on a one-dimensional space. The probability of finding n events in a time interval is defined by the Poisson distribution. The probability density of an inter-event time having a value of τ is given by

$$P(\tau) = \lambda e^{-\lambda\tau} \tag{53}$$

Here, λ is the rate parameter of the process and is equivalent to the inverse of the average inter-event time. For nanopores, events are translocations randomly distributed in time and λ is simply equivalent to the translocation frequency, or capture rate J.

Inhomogeneous Poisson processes are Poisson processes for which the rate parameter is not constant in time. For this reason, we define an instantaneous rate parameter $\lambda(t)$. This is appropriate for nanopores for which we've shown experimentally that the capture rate varies with time $J(t)$. For inhomogeneous Poisson processes, the inter-event time probability density, given that the last event occurred at time t' is defined as:

$$P(t; t') = \lambda(t) e^{-\int_{t'}^{t} \lambda(\tau) d\tau} \tag{54}$$

The cumulative function distribution of equation 54, i.e. the probability that an event occurs before a time t given that the previous event happened at time t', is given by:

$$CFD(t;t') = \int_{t'}^{t} P(\xi;t')d\xi = 1 - e^{-\int_{t'}^{t}\lambda(\tau)d\tau} \tag{55}$$

To simulate inhomogeneous Poisson processes, event times are generated one by one. To do so, first note that the CFD is a monotonic function that has values ranging from 0 to 1. To generate event times, it therefore suffices to randomly generate a number m between 0 and 1 and to find the corresponding time, t^*, for which $m = CFD(t^*:t')$. The process can be done repeatedly by replacing t' by the newly found t^*. As shown in table 1, some time-varying rate functions have analytical solutions, whereas others require numerical solutions. The numerical approach follows the exact same algorithm described here, by calculating values of $CFD(t;t')$ for various values of t, starting at t', and finding the first value $t^*$for which $CFD(t^*;t') > m$.

Table 1. Analytical functions used to randomly generate an inter-event time, given a random number, for various time-varying capture rates.

$\boldsymbol{\lambda(t)}$	$\boldsymbol{t^*}$
$\boldsymbol{J_0}$	$t' - \dfrac{\ln(m-1)}{J_0}$
$\boldsymbol{J_0 t}$	$\sqrt{t'^2 - \dfrac{\ln(m-1)}{J_0}}$
$\boldsymbol{J_0 e^{-t/\tau_0}}$	$-\tau_0 \ln\left(e^{-t'/\tau_0} - \dfrac{\ln(m-1)}{J_0\tau_0}\right)$

5.2 Optimal capture-rate-extraction methods under different experimental conditions

For applications requiring thorough capture rate analysis such as nanopore single-molecule counting, it is important to know how to optimally extract event frequencies from experimental data. For Poisson processes with a time-invariant rate, there exist multiple extraction methods.

Event Counts

The first method used to extract capture rates consists of counting the number of single-molecule events, *N*, and dividing by Δt, the amount of time passed: $J = N/\Delta t$. This is the simplest method but can be practically difficult to apply in cases where inter-event time outliers are present, as will be discussed in more detail below. We term this approach, the "*direct counting method*".

Inter-Event Time Statistics

Capture rate can also be extracted by investigating inter-event times, τ, which follow an exponential distribution of the form, $P(\tau) = Je^{-J\tau}$, where $J = \langle\tau\rangle^{-1}$. Two inter-event time fitting methods can be used for this purpose. The first involves fitting the shifted cumulative probability distribution $S(\tau)$, the survival probability, to an exponential distribution of the form $S(\tau) = e^{-J\tau}$. The survival probability of an inter-event time τ_i is defined:

$$S(\tau_i) = 1 - \frac{n(\tau_i)}{N-1} \tag{56}$$

where $n(\tau_i)$ is the number of events with preceding inter-event times shorter than τ_i, and *N* is the total number of events. We term this approach, the "*survival probability method*".

Finally, one can fit the probability density of inter-event times, $P(\tau)$, directly. This approach is best applied by log-transforming the data first, and fitting the $\log(\tau)$ distribution to the log transform of $P(\tau)$, which in the base 10 logarithm commonly used on logplots has the form

$$H(\tau) = Je^{-J10^{\tau}}10^{\tau}\ln 10 \tag{57}$$

We term this approach, the "*inter-event time distribution method*".

For an ideal, time-invariant (i.e. homogeneous) Poisson process with no interruptions (i.e. nanopore clogs) or false positive events, the most precise extraction method is the direct counting method. Random inter-event times generated following an exponential distribution with a fixed rate of J = 1 Hz are used to demonstrate this in **Figure *35***. Every point in **Figure *35***a shows the average extracted capture rate of 200 realizations of randomly generated data of size N, where N is the number of events. As N increases, all three methods result in capture rates approaching the expected 1 Hz. **Figure *35***b shows the average standard deviation, σ_J, from 1 Hz. Although the uncertainty of all three methods scale as $N^{-0.5}$, the simple counting technique is shown to be the most precise for all N. This is shown in **Figure *35***b which plots the standard deviation's scaling with data length, and **Figure *35***c which shows the deviation scaled with the ideal Poisson deviation of $N^{-0.5}$. Additionally, the survival probability method is observed to be more precise than the inter-event time distribution method for small data sets (N < 100), with the opposite being true for larger datasets (N > 100).

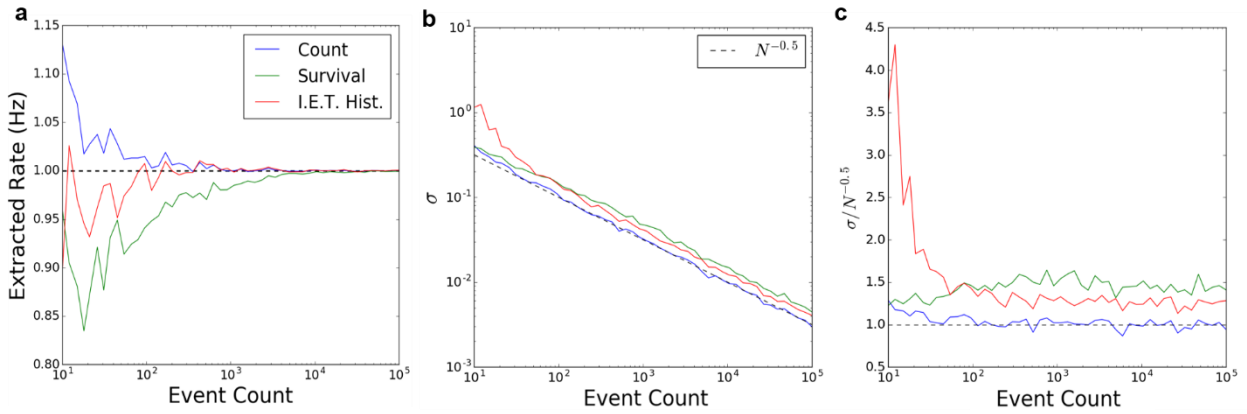

Figure 35. Comparison of three methods for capture rate extraction as a function of event counts. A count is simulated by averaging of 200 randomly generated Poisson processes with an expected rate of 1 Hz. **(a)** Average extracted capture rates as a function of data points for the three methods discussed **(b)** Average standard deviations from expected rate of 1Hz for the rates calculated in (a). **(c)** Average standard deviations from (b) normalized by $N^{-0.5}$, the standard deviation for an ideal Poisson process

Although informative, the analysis shown above is not necessarily representative of real-world nanopore data. In addition to time-variation of the capture rate already discussed, two other

types of issues can be present in real datasets. First, nanopore clogs due to molecules being stuck inside or near a pore can temporarily prevent new molecules from being captured, affecting the total number of molecules counted in a fixed time. Second, false positive events can also be present, due either to collisions, contamination, or simply momentarily higher noise on the open pore current baseline. When one or both of these conditions are present in a dataset, statistical inter-event time analysis can be advantageous over the simple counting technique.

While data cleanup and other post-processing manipulations can be used for capture rate extraction of more complex datasets, it is important to know which analysis technique is most robust and less dependent on user-defined analysis parameters. To achieve this, we again generated data randomly, though this time with artificially added inter-event time outliers. **Figure *36*** shows the standard deviation, σ_J, and scaled standard deviation, $\sigma_J/N^{-0.5}$, for the three capture rate extraction methods in four different outlier scenarios. The datasets for first two outlier scenarios include 10 and 20 inter-event time outliers of 5 s each, to model temporary clogs. Interestingly, the inter-event time distribution method is the optimal capture rate extraction method for intermediate dataset sizes ($10^2 < N < 10^4$), although the direct counting method is naturally more precise as $N \rightarrow \infty$. The other two outlier cases include in their datasets 25 and 50 short inter-event time outliers of 1 ms each, to model the effect of false positive events as discussed above. In these cases, inter-event time analysis is barely affected by such outlier type, whereas the direct counting approach shows higher standard deviation for small data sets ($N < 10^3$).

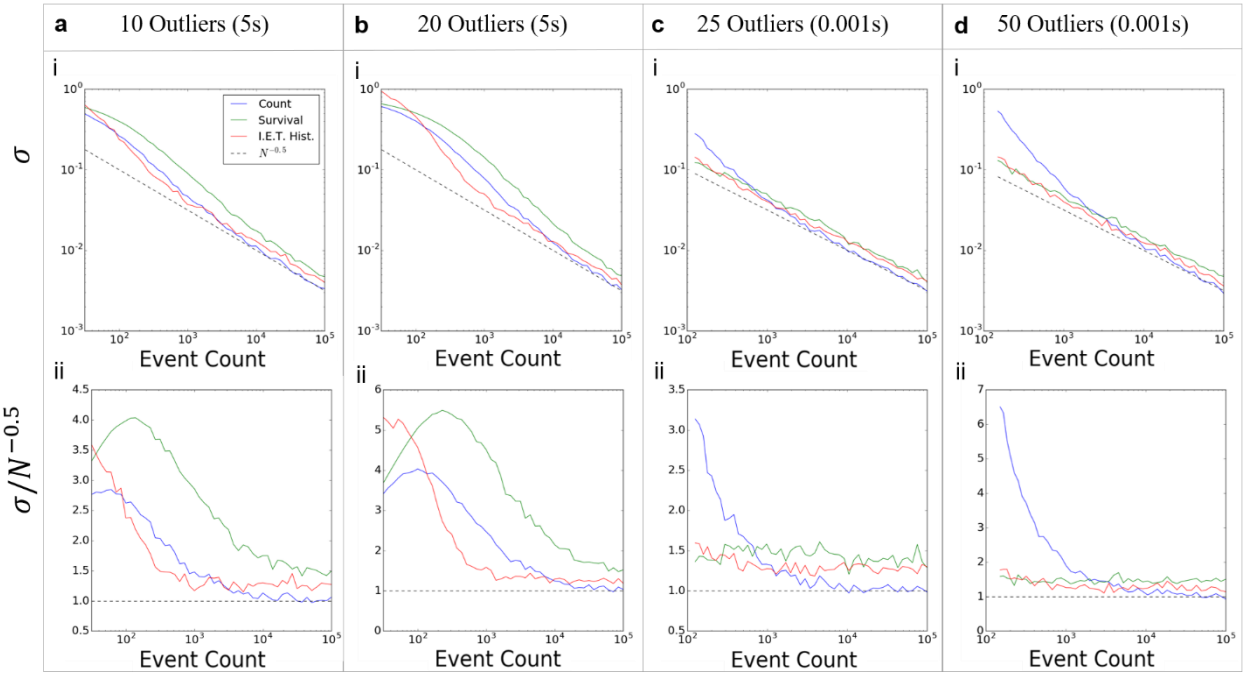

Figure 36. Comparison of the three methods for capture rate extraction as a function of event counts after introducing different number and types of inter-event time outliers. Every point is the average of 200 randomly generated Poisson processes with an expected rate of 1 Hz. The first row shows the standard deviation from the expected rate of 1Hz, whereas the second row shows the same deviation scaled by the ideal Poisson error of $N^{-0.5}$. **(a)** and **(b)** show capture rate deviations when 10 and 20 long inter-event times (5s) are introduced, respectively. **(c)** and **(d)** show capture rate deviations when 25 and 50 short inter-event times (1ms) are introduced, respectively

Table 2 below summarizes which method to use to extract capture rate over the different cases discussed above:

Table 2. Optimal capture rate extraction method for various experimental conditions

	Ideal Poisson Process	Clogs	False positive
Direct Counting	Best for all *N*	Best for large N	Largest error for N<1000 / Best for large N
Survival Probability	Useful for large datasets	Largest error for N>100	Acceptable Error
Inter-event time distribution	Largest error for small N <100	Best for intermediate N	Best for all N

5.3 Extracting Capture Rates of Time-Varying Capture Processes

In cases where the capture rate is time-varying, additional care is required when extracting physically meaningful analogues of captures rate. The following section explores non-homogeneous Poisson processes, *i.e.* processes with time-varying capture rates $J(t)$, and the effect this has on fixed capture rate extraction through the three methods already presented. For disambiguation purposes, we name $J(t)$ the true capture rate driving the non-homogeneous Poisson process, and J_{ext} the measured rate extracted from either of the three analysis methods presented. We assume no prior knowledge of $J(t)$ is obtainable.

Note that the direct counting method for a time-varying driving rate $J(t)$ reliably results, by definition, in the average value of $J(t)$ over the timespan of the experiment, *T*:

$$\frac{N}{T} = \frac{1}{T}\int_0^T J(t)dt = \overline{J(T)} \tag{58}$$

We investigate three temporal variation patterns in $J(t)$: Oscillating, drifting, and undergoing a biased random walk.

5.3.1 Oscillating Capture Rate

The first type of capture-variation tested is the oscillation type, represented by fluctuations of the form: $J(t) = J_0(1 + A\sin(\omega t))$. Here J_0 is the average capture rate, whereas A and ω determine the amplitude and angular frequency of the oscillation. Experiments of 500 second durations (T=500) are simulated, as shown in **Figure *37***, where the normalized extracted rate, J_{ext}/J_0, is plotted with respect to the normalized experimental time, ωT.

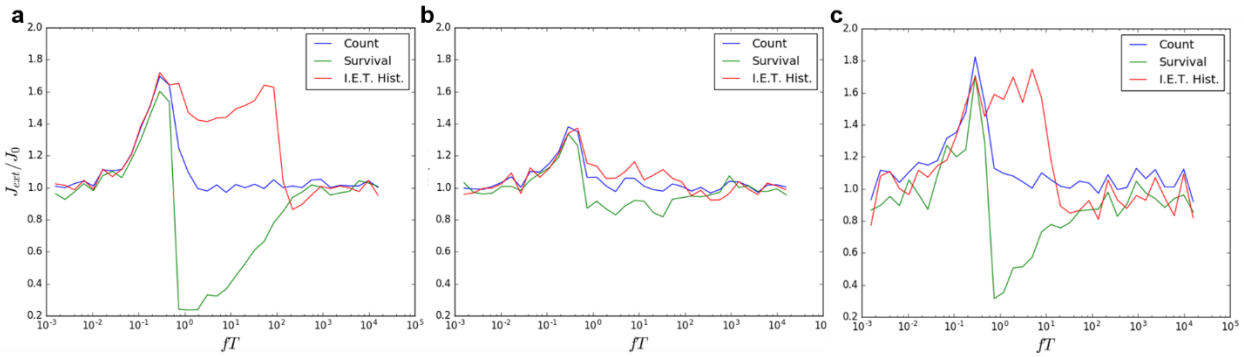

Figure 37. Normalized extracted capture rate for a 500 s time oscillating capture process, measured at various frequencies with values **(a)** J_0=1 and A=1, **(b)** J_0=1 and A=0.5, and **(c)** J_0=0.1 and A=1. The y axis shows the extracted rate normalized by J_0. Every data point is the average of 5 realizations.

Figure *37*a-c show experiments simulated with different values of A and J_0. For all experiments, the observed frequency dependence can be separated into three regimes. At low frequencies ($\omega T << 1$), J_{ext} can differ significantly from J_0. This is explained by the driving capture rate being analogous to a drifting driving rate at very low frequencies relative to the total experimental time, rather than an oscillating one, with the direction and magnitude of the error being determined by the phase and amplitude of the oscillation. As the driving frequency increases, multiple oscillations can be observed during a single experiment. This means that a few long inter-event times are introduced in the distribution, and much like with the introduction of inter-event outliers, the survival probability method results in a bad fit with a low extracted capture rate. The inter-event time distribution method however is barely affected by the long inter-event times and results in a good fit, though the extracted rate is higher than J_0. At high frequencies ($\omega T >> 1$), J_{ext} becomes frequency independent for all three methods and is equivalent to the average driving capture rate J_0, since the oscillations are no longer relevant on the timescale of the inter-event times. This behavior is observable when less than one event is present per capture rate oscillation. For this reason, the ωT value at which $J_{ext} \propto \omega^0$ depends also on the value of J_0 and T, as shown in **Figure *37***c.

To further demonstrate the change in behaviour for the three described frequency ranges, **Figure *38***a-c plot the capture rate variations of 500-second experiments for frequencies of 1 mHz, 10 mHz and 10 Hz, respectively, where vertical red lines indicate the presence of simulated events. **Figure *38***d-f shows the three capture rate extraction methods applied to the three different frequencies with $A = 1$.

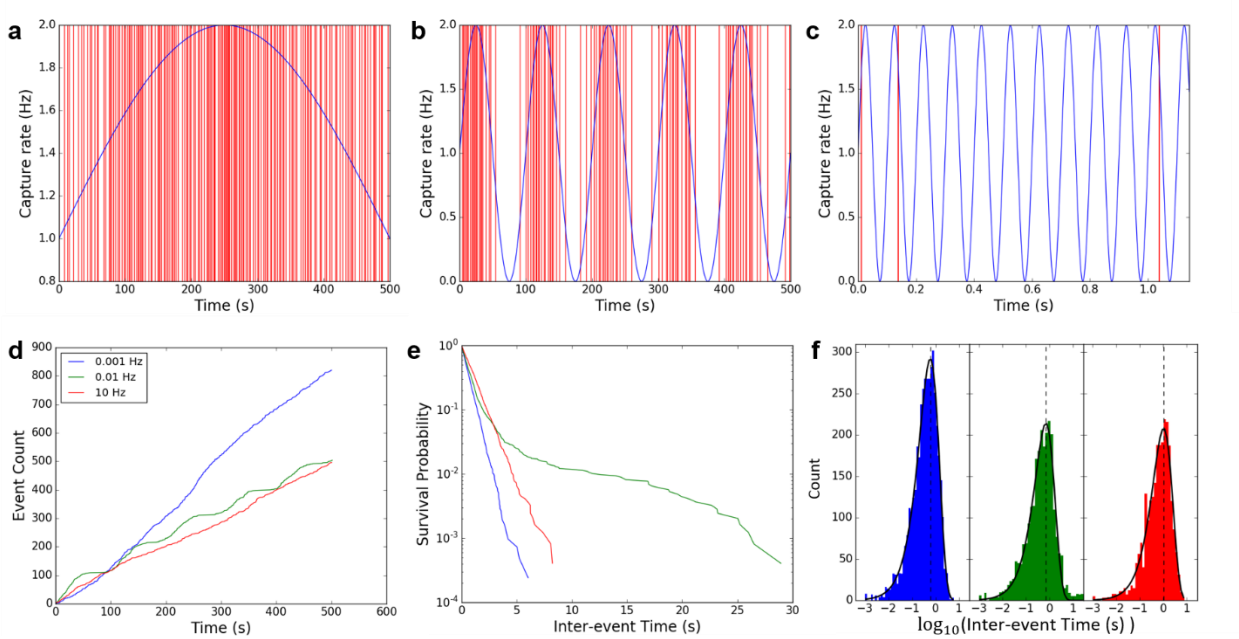

Figure 38. (a), **(b)** and **(c)** show the sinusoidal driving capture rate evolution in time, for frequencies of 1 mHz, 10 mHz and 10 Hz, respectively. Red vertical lines represent simulated event locations. Only 1 line out of 5 is shown for clarity purposes. **(d)**, **(e)** and **(f)** show the effect of a sinusoidal driving capture rate on the direct counting, the survival probability and the inter-event time distribution methods, respectively.

5.3.2 Drifting Capture Rate

We next simulate a constantly drifting capture rate $J(t)=J_0(1+pt/T)$. Here J_0 is the capture rate at time $t=0$, T is the simulation duration, and p is the slope of the drifting capture-rate. **Figure *39*** plots normalized measured capture rates J_{ext}/J_0 as a function of the drift rate p for simulations of 1000 seconds. For most drift values and extraction methods shown, the measured capture rate is simply equal to the average capture rate during the experiment. **Figure *39***b-d show the analysis for the three capture rate extraction methods. The survival probability method is not well-suited

for fitting drifting capture rate processes, as seen in **Figure *39***c. The inter-event distribution method results in reasonable fits, as shown in **Figure *39***d.

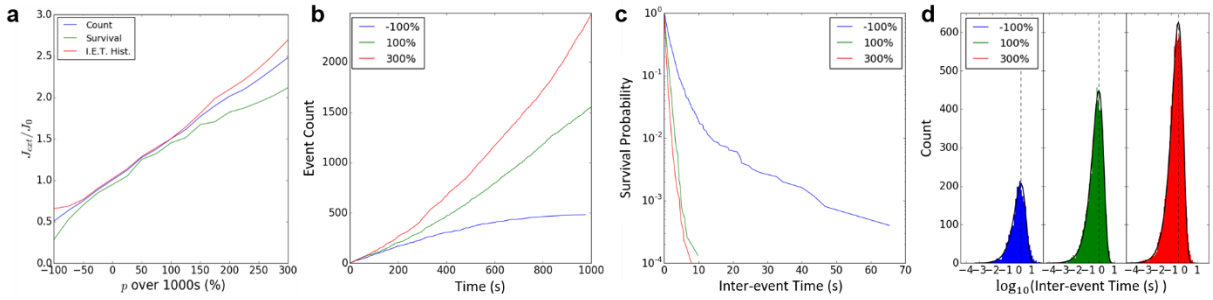

Figure 39. (a) Extracted capture rate for a 1000 s non-homogeneous drifting capture process, measured for various drift rates, using the three analysis methods. Every data point is the average of 5 realizations. **(b)**, **(c)** and **(d)** show the effect of a sinusoidal driving capture rate on the direct counting, the survival probability and the inter-event time distribution methods, respectively.

5.3.3 Randomly Varying Capture Rate

Finally, we demonstrate the three methods of capture rate measurement using a biased random walk. **Figure *40*** shows a 2000 second simulated random-walk driving rate, and the three extraction methods. A bias of 2.5% was used in the positive direction, with a reflective condition at $J = 0$. Results are very similar to the previous two types of non-homogeneous processes, in that the survival probability method performs poorly, whereas inter-event distribution method is still able to provide a reasonable fit.

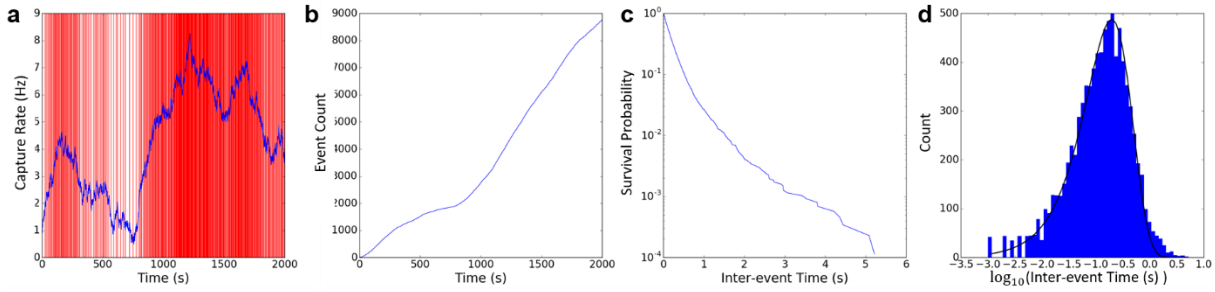

Figure 40. (a) Biased random walk driving capture rate versus time. Red vertical lines represent simulated event locations. Only 1 line out of 25 is shown. **(b)**, **(c)** and **(d)** show the effect of a biased random walk driving capture rate on the direct counting, the survival probability and the inter-event time distribution methods, respectively

5.4 Controlled Counting with Time-Varying Capture Rates

The main text proposes a method of determining biomolecular target concentration which relies on having two populations in the same solution, undergoing the same capture process independently. Underlying this method is the assumption that both populations have capture rates $J_1(t)=R_c(t)c_1$ and $J_2(t)=R_c(t)c_2$, where $R_c(t)$ is the time-varying normalized capture rate. **Figure *41***b-c shows the high correlation between two simulated populations counts of different concentrations (c_1=5, c_2=1) that follow the same normalized driving rate, a biased random-walk $R_c(t)$ shown in **Figure *41***a. **Figure *41***d shows the evolution of the normalized capture ratio $J_1 c_2 / J_2 c_1$ with time, using all three rate-extraction methods to obtain J_1 and J_2. All three methods result in a normalized ratio close to 1, however the survival probability method worsens after ~500 seconds, when the driving capture rate is reduced significantly, and is small compared to the average value, due to the survival probability fit not handling long outliers well.

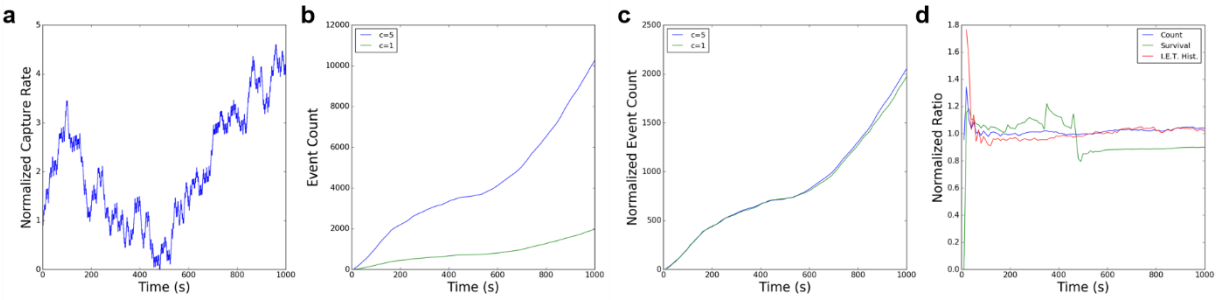

Figure 41. (a) Biased random walk driving capture rate versus time. **(b)** Event count time evolution for two populations (c_1=5 c_2=1) undergoing the same normalized capture rate **(c)** Normalized event count ($N_1(t)/c_1$ and $N_2(t)/c_2$) time evolution **(d)** Extracted capture rate ratio normalized by concentration ratio throughout the experiment using the three extraction methods

In cases where capture rates are expected to be time-varying, the capture rate becomes an ill-defined quantity. However, it is still possible to improve the precision of concentration measurements by taking a ratio of the time-averaged capture rates, or equivalently, the total number of events obtained during the experiment:

$$J_{ext} = \frac{N}{T} = \frac{1}{T}\int_0^T J(t)dt = \frac{c}{T}\int_0^T R_c(t)dt = \frac{c}{T}\overline{R_c} \tag{59}$$

Figure *42* shows the normalized ratio distribution from the three extraction methods, of two populations (c_1=5, c_2=1) undergoing the same $R_c(t)$ generated from a different biased random walk for every experiment. All three methods result in ratio distributions centered around 1. As expected, the most precise method is the direct counting method, followed by the inter-event-time distribution method, and lastly by the survival probability method.

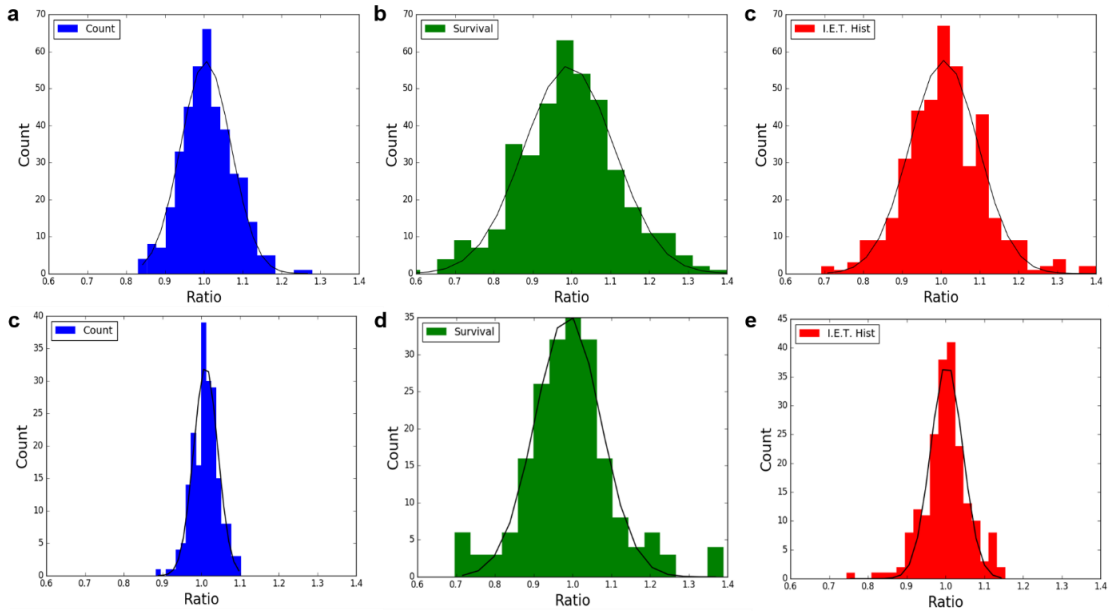

Figure 42. Capture-rate-ratio distribution, using the three extraction methods. Every ratio originates from two populations of different concentration, driven by the same randomly generated normalized biased random walk. A random walk is randomly generated for every realization. Every distribution is fit to a normal distribution, in order to extract the average ratio and its standard deviation, σ_J. The average ratios for all the tested methods and experiments were measured as 1.00±0.01. **(a)**, **(b)** and **(c)** show the capture-rate-ratio distribution of 400 realizations of 200 seconds, for which σ_J = 0.065, 0.116, 0.088, respectively. **(d)**, **(e)** and **(f)** show the capture-rate-ratio distribution of 200 realizations of 500 seconds, for which σ_J = 0.031, 0.084, 0.041, respectively

Two different experiment durations have been tested, 200 and 500s, and shown, **Figure *42***a-c and **Figure *42***d-f, respectively. The standard deviations of the measured capture rate using the inter-event-time distribution method are around ~35% larger than the direct-counting method. This is consistent with results from chapter 4, for which the CV of r_J is measured at 0.16, whereas the CV of r_N is measured at 0.12, a 33% relative difference.

Chapter 6

Outlook

6.1 Potential Sources of Capture Rate Variability

The presented technique of controlled counting has demonstrated a way of avoiding characterizing sources of capture rate variations in order to obtain precise concentration measurements. For this reason, the nature of the sources of variability and the physical processes behind were not discussed in detail. For any target label that cannot be quantified using controlled counting, understanding, characterizing and quantifying sources of variability would be of great use to control and reduce the quantification uncertainty. Using a qualitative description of capture, based on experimental data, it is possible to build an intuition on how other forces present in the system should behave. More precisely, even with the presence of other forces in the system, the diffusive regime is experimentally found to be DNA-length independent and linearly dependent on voltage. In order to elucidate the nature of the forces that would allow such properties, let's follow the absorbing-hemisphere derivation of capture radius and rate (Equations 35-37) using an extra velocity term $v_{unknown} = C/r^{\alpha}$, of undisclosed origin:

$$\begin{aligned} 0 &= -\frac{\mu_e G \Delta V}{\sigma 2\pi r^2} + \frac{D}{r} + \frac{C}{r^{\alpha}} \\ &= -\frac{A\Delta V}{r^2} + \frac{BL^{-\nu}}{r} + \frac{C}{r^{\alpha}} \end{aligned} \tag{60}$$

Here, A and B are DNA-length and voltage independent coefficients used for simplifying the expression, whereas C is assumed to depend on both L and ΔV. Note that it is assumed that the added term is hemi-spherically symmetric as a demonstrative purpose. What dependencies on

DNA length, L, and voltage, ΔV, must the coefficient C have so that the diffusion-limited capture rate remains DNA length independent and linearly dependent on voltage? Following Equation 35, we know that since capture rate scales as $J_{diff} \propto L^0 \Delta V$, the scaling of the capture radius ($r^* \propto J_{diff} D$) must follow $r^* \propto L^\nu \Delta V$. By solving Equation 60 for different values of α, a pattern in the required scaling becomes apparent.

Table 3. Various dependencies of velocities induced by forces that could be present in the nanopore system, while maintaining the DNA-length independence and linear voltage dependence.

α	r^*	$\propto C/r^\alpha$
0	$\frac{-BL^{-\nu} + \sqrt{B^2 L^{-2\nu} + 4A\Delta VC}}{2C}$	$L^{-2\nu}\Delta V^{-1}$
1	$\frac{A\Delta V}{BL^{-\nu} + C}$	$\frac{L^{-\nu}\Delta V^0}{r}$
2	$\frac{A\Delta V - C}{BL^{-\nu}}$	$\frac{L^0\Delta V^1}{r^2}$ OR $\frac{L^0\Delta V^0}{r^2}$
3	$\frac{A\Delta V + \sqrt{A^2\Delta V^2 + 4BL^{-\nu}C}}{2BL^{-\nu}}$	$\frac{L^\nu \Delta V^2}{r^3}$
n	...	$\frac{L^{(n-2)\nu}\Delta V^{n-1}}{r^n}$

Only a few relevant physical phenomena correspond to the various scalings shown in the third column; Particularly, the two different cases of $\alpha = 2$. A velocity term of the form $v \propto \Delta V/r^2$ could originate from electroosmotic flow,[124,127,137] whereas the form $v \propto r^{-2}$ could originate from convective flows induced by pressure gradients,[138–140] or something resembling electrostatic interactions. Moreover, by following the derivation of the capture rate expression with these two extra terms, we see that the addition of an EOF-like force results in a different slope in a Capture vs Voltage graph, whereas the $\propto r^{-2}$ term results in a non-zero intercept.

$$0 = -\frac{\mu_e G \Delta V}{\sigma 2\pi r^2} + \frac{C_1 \Delta V}{2\pi r^2} + \frac{C_2}{2\pi r^2} + \frac{D}{r} \tag{61}$$

$$r^* = \frac{\left(\frac{\mu_e G}{\sigma} + C_1\right)\Delta V + C_2}{2\pi D} \tag{62}$$

$$J_{diff}/c = R_{diff} = \left(\frac{\mu_e G}{\sigma} + C_1\right)\Delta V + C_2 \tag{63}$$

Interestingly, a non-zero intercept is often shown in publications, although never discussed as depicted in **Figure *43***a-b. Although an oversimplification, the above description raises interesting questions regarding the incomplete picture of capture rate.

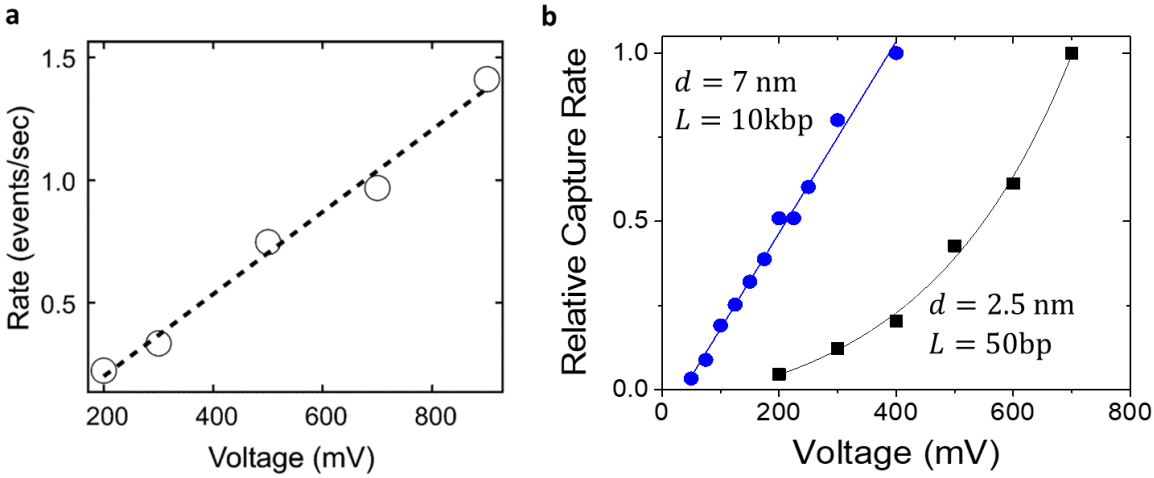

Figure 43. Capture Rate Voltage Dependence showing non-zero intercepts a) in a 15nm[79] (b) and 7nm solid-state pore.[141] Figure (a) Reprinted with permission from [*Chen, P.; Gu, J.; Brandin, E.; Kim, Y.-R. R.; Wang, Q.; Branton, D. Probing Single DNA Molecule Transport Using Fabricated Nanopores. Nano Lett. 2004, 4 (11), 2293–2298*] Copyright (2020) American Chemical Society

6.2 Expanding the Applicability of the Controlled-Counting Method

The experimental data shown in this work all pertains to linear DNA. Although intuitively controlled counting should work on different types of molecules due to its innate simplicity, this has not been demonstrated yet. For precise biomarker concentration measurements with nanopores, this is of primordial importance. The logical next step is therefore to try controlled counting on two molecules with different capture properties, i.e. different Q functions.

Controlled counting is not expected to work in the barrier-limited regime, due to the non-linear field dependence of the barrier-limited regime and the inability to precisely experimentally control the field strength. According to theoretical models, the regime transition length L^*, i.e. the diffusion-limited regime range, depends on the strength of the electric field outside the pore responsible for capture. To expand the range of applicability of the diffusion-limited regime, methods of increasing the electric field, or simply the attractive force outside the pore, should be explored. This potentially includes exploring temperature, pressure or salt gradients. At the moment, salt gradients seem to be the best avenue to investigate, since it has been reported as increasing capture rate, while reducing translocation velocity due to local EOF flows inside the pore.[45,142–145] Some questions however first need to be addressed. For example, are capture properties and regimes identical in salt asymmetry? Can controlled counting work in salt concentration gradients? What gradient conditions are ideal for signal detection and amplification?

Lastly, multiple schemes have been proposed to reach ultra-sensitivity with nanopores, such as dielectrophoresis-based pre-concentration. It remains unknown however if using an internal calibrator would result in more precise measurements, in such two-step detection schemes. For controlled counting to be applicable in such detection methods, the properties of capture by dielectrophoresis for different DNA lengths or labels should be studied. The same should also be done for non steady-state capture, the step after which target molecules are pre-concentrated near the pore opening.

Finding ways of increasing the range of applicability of controlled counting would bring us one step closer to having a rapid, precise, low-cost point-of-need ultrasensitive sensor.

Bibliography

(1) Kelley, S. O. What Are Clinically Relevant Levels of Cellular and Biomolecular Analytes? *ACS Sensors* **2017**, *2* (2), 193–197. https://doi.org/10.1021/acssensors.6b00691.

(2) Wu, Y.; Tilley, R. D.; Gooding, J. J. Challenges and Solutions in Developing Ultrasensitive Biosensors. *J. Am. Chem. Soc.* **2019**, *141* (3), 1162–1170. https://doi.org/10.1021/jacs.8b09397.

(3) Rissin, D. M.; Kan, C. W.; Campbell, T. G.; Howes, S. C.; Fournier, D. R.; Song, L.; Piech, T.; Patel, P. P.; Chang, L.; Rivnak, A. J.; et al. Single-Molecule Enzyme-Linked Immunosorbent Assay Detects Serum Proteins at Subfemtomolar Concentrations. *Nat. Biotechnol.* **2010**, *28* (6), 595–599. https://doi.org/10.1038/nbt.1641.

(4) Fan, X.; White, I. M.; Shopova, S. I.; Zhu, H.; Suter, J. D.; Sun, Y. Sensitive Optical Biosensors for Unlabeled Targets : A Review. *Anal. Chim. Acta* **2008**, *0* (1–2), 8–26. https://doi.org/10.1016/j.aca.2008.05.022.

(5) Armani, A. M.; Kulkarni, R. P.; Fraser, S. E.; Flagan, R. C.; Vahala, K. J. Label-Free, Single-Molecule Detection with Optical Microcavities. *Science (80-.).* **2007**, *317* (5839), 783–787. https://doi.org/10.1126/science.1145002.

(6) Cohen, L.; Walt, D. R. Single-Molecule Arrays for Protein and Nucleic Acid Analysis. *Annu. Rev. Anal. Chem.* **2017**, *10* (1), 1–19. https://doi.org/10.1146/annurev-anchem-061516-045340.

(7) Macchia, E.; Manoli, K.; Holzer, B.; Franco, C. Di; Ghittorelli, M.; Torricelli, F.; Alberga, D.; Mangiatordi, G. F.; Palazzo, G.; Scamarcio, G.; et al. Single-Molecule Detection with a Millimetre-Sized Transistor. *Nat. Commun.* **2018**, *9* (2018). https://doi.org/10.1038/s41467-018-05235-z.

(8) Gooding, J. J.; Gaus, K. Single-Molecule Sensors : Challenges and Opportunities for Quantitative Analysis. *Angew. Chemie Int. Ed.* **2016**, *55* (38), 11354–11366. https://doi.org/10.1002/anie.201600495.

(9) Todd, J.; Freese, B.; Lu, A.; Held, D.; Morey, J.; Livingston, R.; Goix, P. Ultrasensitive Flow-Based Immunoassays Using Single-Molecule Counting. *Clin. Chem.* **2007**, *53* (11), 1990–1995. https://doi.org/10.1373/clinchem.2007.091181.

(10) Walt, D. R. Optical Methods for Single Molecule Detection and Analysis. *Anal. Chem.* **2013**, *85* (3), 1258–1263. https://doi.org/10.1021/ac3027178.

(11) Ha, T. Single-Molecule Methods Leap Ahead. *Nat. Methods* **2014**, *11* (10), 1015–1018. https://doi.org/10.1038/nmeth.3107.

(12) Han, X. X.; Zhao, B.; Ozaki, Y. Surface-Enhanced Raman Scattering for Protein Detection. *Anal. Bioanal. Chem.* **2009**, *394* (7), 1719–1727. https://doi.org/10.1007/s00216-009-2702-3.

(13) Dey, S.; Vaidyanathan, R.; Carrascosa, L. G.; Shiddiky, M. J. A. A.; Trau, M. Electric Field Induced Isolation, Release, and Recapture of Tumor Cells. *ACS Sensors* **2016**, *1* (4), 399–405. https://doi.org/10.1021/acssensors.5b00157.

(14) Gooding, J. J. What Does Ultrasensitive Really Mean? *ACS Sensors* **2019**, *4* (3), 528. https://doi.org/10.1021/acssensors.9b00404.

(15) Hirschfeld, T. Optical Microscopic Observation of Single Small Molecules. *Appl. Opt.* **1976**, *15* (12), 2965. https://doi.org/10.1364/ao.15.002965.

(16) Sykes, P. J.; Neoh, S. H.; Brisco, M. J.; Hughes, E.; Condon, J.; Morley, A. A. Quantitation of Targets for PCR by Use of Limiting Dilution. *Biotechniques* **1992**, *13* (3), 444–449.

(17) Vogelstein, B.; Kinzler, K. W. Digital PCR. *Proc. Natl. Acad. Sci. U. S. A.* **1999**, *96* (16), 9236–9241. https://doi.org/10.1073/pnas.96.16.9236.

(18) Hindson, B. J.; Ness, K. D.; Masquelier, D. A.; Belgrader, P.; Heredia, N. J.; Makarewicz, A. J.; Bright, I. J.; Lucero, M. Y.; Hiddessen, A. L.; Legler, T. C.; et al. High-Throughput Droplet Digital PCR System for Absolute Quantitation of DNA Copy Number. *Anal. Chem.* **2011**, *83* (22), 8604–8610. https://doi.org/10.1021/ac202028g.

(19) Pinheiro, L. B.; Coleman, V. A.; Hindson, C. M.; Herrmann, J.; Hindson, B. J.; Bhat, S.; Emslie, K. R. Evaluation of a Droplet Digital Polymerase Chain Reaction Format for DNA Copy Number Quantification. *Anal. Chem.* **2012**, *84* (2), 1003–1011. https://doi.org/10.1021/ac202578x.

(20) Kreutz, J. E.; Munson, T.; Huynh, T.; Shen, F.; Du, W.; Ismagilov, R. F. Theoretical Design and Analysis of Multivolume Digital Assays with Wide Dynamic Range Validated Experimentally with Microfluidic Digital PCR. *Anal. Chem.* **2011**, *83* (21), 8158–8168. https://doi.org/10.1021/ac201658s.

(21) Jain, A.; Liu, R.; Ramani, B.; Arauz, E.; Ishitsuka, Y.; Ragunathan, K.; Park, J.; Chen, J.; Xiang, Y. K.; Ha, T. Probing Cellular Protein Complexes Using Single-Molecule Pull-Down. *Nature* **2011**, *473* (7348), 484–488. https://doi.org/10.1038/nature10016.

(22) Vollmer, F.; Arnold, S. Whispering-Gallery-Mode Biosensing : Label- Free Detection down to Single Molecules. *Nat. Methods* **2008**, *5* (7), 591–596. https://doi.org/10.1038/NMETH.1221.

(23) Boyd, R. W.; Heebner, J. E. Sensitive Disk Resonator Photonic Biosensor. *Appl. Opt.* **2001**, *40* (31), 5742. https://doi.org/10.1364/ao.40.005742.

(24) Arnold, S.; Khoshsima, M.; Teraoka, I.; Holler, S.; Vollmer, F. Shift of Whispering-Gallery Modes in Microspheres by Protein Adsorption. *Opt. Lett.* **2003**, *28* (4), 272. https://doi.org/10.1364/ol.28.000272.

(25) Zijlstra, P.; Paulo, P. M. R.; Orrit, M. Optical Detection of Single Non-Absorbing Molecules Using the Surface Plasmon Resonance of a Gold Nanorod. *Nat. Nanotechnol.* **2012**, *7* (6), 379–382. https://doi.org/10.1038/nnano.2012.51.

(26) Beuwer, M. A.; Prins, M. W. J. J.; Zijlstra, P. Stochastic Protein Interactions Monitored by Hundreds of Single-Molecule Plasmonic Biosensors. *Nano Lett.* **2015**, *15* (5), 3507–3511. https://doi.org/10.1021/acs.nanolett.5b00872.

(27) Taylor, A. B.; Zijlstra, P. Single-Molecule Plasmon Sensing: Current Status and Future Prospects. *ACS Sensors* **2017**, *2* (8), 1103–1122. https://doi.org/10.1021/acssensors.7b00382.

(28) Mejía-Salazar, J. R.; Oliveira, O. N. Plasmonic Biosensing. *Chem. Rev.* **2018**, *118* (20), 10617–10625. https://doi.org/10.1021/acs.chemrev.8b00359.

(29) Kim, S. H.; Hong, K.; Xie, W.; Lee, K. H.; Zhang, S.; Lodge, T. P.; Frisbie, C. D. Electrolyte-Gated Transistors for Organic and Printed Electronics. *Adv. Mater.* **2013**, *25* (13), 1822–1846. https://doi.org/10.1002/adma.201202790.

(30) Macchia, E.; Tiwari, A.; Manoli, K.; Holzer, B.; Ditaranto, N.; Picca, R. A.; Cio, N.; Franco, C. Di; Scamarcio, G.; Palazzo, G.; et al. Label-Free and Selective Single-Molecule Bioelectronic Sensing with a Millimeter-Wide Self-Assembled Monolayer of Anti-Immunoglobulins. *Chem. Mater.* **2019**, *31* (17), 6476–6483. https://doi.org/10.1021/acs.chemmater.8b04414.

(31) Macchia, E.; Manoli, K.; Holzer, B.; Di Franco, C.; Picca, R. A.; Cioffi, N.; Scamarcio, G.; Palazzo, G.; Torsi, L. Selective Single-Molecule Analytical Detection of C-Reactive Protein in Saliva with an Organic Transistor. *Anal. Bioanal. Chem.* **2019**, *411* (19), 4899–4908. https://doi.org/10.1007/s00216-019-01778-2.

(32) Torricelli, F.; Macchia, E.; Manoli, K.; Di Franco, C.; Kovacs-Vajna, Z. M.; Palazzo, G.; Scamarcio, G.; Torsi, L. Analysis of Label-Free Single-Molecule Biosensors Based on Gate-Biofunctionalized Organic Transistors. *2019 IEEE 8th Int. Work. Adv. Sensors Interfaces* **2019**, 70–74. https://doi.org/10.1109/IWASI.2019.8791380.

(33) Deamer, D.; Akeson, M.; Branton, D. Three Decades of Nanopore Sequencing. *Nat. Biotechnol.* **2016**, *34* (5), 518–524. https://doi.org/10.1038/nbt.3423.

(34) Wanunu, M. Nanopores: A Journey towards DNA Sequencing. *Phys. Life Rev.* **2012**, *9* (2), 125–158. https://doi.org/10.1016/j.plrev.2012.05.010.

(35) Storm, A. J.; Chen, J. H.; Ling, X. S.; Zandbergen, H. W.; Dekker, C. Fabrication of Solid-State Nanopores with Single-Nanometre Precision. *Nat. Mater.* **2003**, *2* (8), 537–540. https://doi.org/10.1038/nmat941.

(36) Li, J.; Stein, D.; McMullan, C.; Branton, D.; Aziz, M. J.; Golovchenko, J. A. Ion-Beam Sculpting at Nanometre Length Scales. *Nature* **2001**, *412* (6843), 166–169. https://doi.org/10.1038/35084037.

(37) Beamish, E.; Kwok, H.; Tabard-Cossa, V.; Godin, M. Precise Control of the Size and Noise of Solid-State Nanopores Using High Electric Fields. *Nanotechnology* **2012**, *23* (40), 405301. https://doi.org/10.1088/0957-4484/23/40/405301.

(38) Kwok, H.; Briggs, K.; Tabard-Cossa, V. Nanopore Fabrication by Controlled Dielectric Breakdown. *PLoS One* **2014**, *9* (3), e92880. https://doi.org/10.1371/journal.pone.0092880.

(39) Gilboa, T.; Zrehen, A.; Girsault, A.; Meller, A. Optically-Monitored Nanopore Fabrication Using a Focused Laser Beam. *Sci. Rep.* **2018**, *8* (1), 9765. https://doi.org/10.1038/s41598-018-28136-z.

(40) Bell, N. A. W.; Thacker, V. V.; Hernández-Ainsa, S.; Fuentes-Perez, M. E.; Moreno-Herrero, F.; Liedl, T.; Keyser, U. F. Multiplexed Ionic Current Sensing with Glass Nanopores. *Lab Chip* **2013**, *13* (10), 1859–1862. https://doi.org/10.1039/c3lc50069a.

(41) Lo, C. J.; Aref, T.; Bezryadin, A. Fabrication of Symmetric Sub-5 Nm Nanopores Using Focused Ion and Electron Beams. *Nanotechnology* **2006**, *17* (13), 3264–3267. https://doi.org/10.1088/0957-4484/17/13/031.

(42) Ivanov, A. P.; Actis, P.; Jönsson, P.; Klenerman, D.; Korchev, Y.; Edel, J. B. On-Demand Delivery of Single DNA Molecules Using Nanopipets. *ACS Nano* **2015**, *9* (4), 3587–3594. https://doi.org/10.1021/acsnano.5b00911.

(43) Nakane, J.; Akeson, M.; Marziali, A. Evaluation of Nanopores as Candidates for Electronic Analyte Detection. *Electrophoresis* **2002**, *23* (16), 2592–2601. https://doi.org/10.1002/1522-2683(200208)23:16<2592::AID-ELPS2592>3.0.CO;2-L.

(44) Gershow, M.; Golovchenko, J. A. Recapturing and Trapping Single Molecules with a Solid-State Nanopore. *Nat. Nanotechnol.* **2007**, *2* (12), 775–779. https://doi.org/10.1038/nnano.2007.381.

(45) Wanunu, M.; Morrison, W.; Rabin, Y.; Grosberg, A. Y.; Meller, A. Electrostatic Focusing of Unlabelled DNA into Nanoscale Pores Using a Salt Gradient. *Nat. Nanotechnol.* **2010**, *5* (2), 160–165. https://doi.org/10.1038/nnano.2009.379.

(46) Grosberg, A. Y.; Rabin, Y. DNA Capture into a Nanopore: Interplay of Diffusion and Electrohydrodynamics. *J. Chem. Phys.* **2010**, *133* (16), 165102. https://doi.org/10.1063/1.3495481.

(47) Tahvildari, R.; Beamish, E.; Tabard-Cossa, V.; Godin, M. Integrating Nanopore Sensors within Microfluidic Channel Arrays Using Controlled Breakdown. *Lab Chip* **2015**, *15* (6), 1407–1411. https://doi.org/10.1039/C4LC01366B.

(48) Freedman, K. J.; Otto, L. M.; Ivanov, A. P.; Barik, A.; Oh, S.-H. H.; Edel, J. B. Nanopore Sensing at Ultra-Low Concentrations Using Single-Molecule Dielectrophoretic Trapping. *Nat. Commun.* **2016**, *7*, 10217. https://doi.org/10.1038/ncomms10217.

(49) Arcadia, C. E.; Reyes, C. C.; Rosenstein, J. K. In Situ Nanopore Fabrication and Single- Molecule Sensing with Microscale Liquid Contacts. *ACS Nano* **2017**, *11* (5), 4907–4915. https://doi.org/10.1021/acsnano.7b01519.

(50) Oxford Nanopore Technologies Products.

(51) Zhang, Y.; Miyahara, Y.; Derriche, N.; Yang, W.; Yazda, K.; Capaldi, X.; Liu, Z.; Grutter, P.; Reisner, W. Nanopore Formation via Tip-Controlled Local Breakdown Using an Atomic Force Microscope. *Small Methods* **2019**, *1900147*, 1900147. https://doi.org/10.1002/smtd.201900147.

(52) Gilboa, T.; Zvuloni, E.; Zrehen, A.; Squires, A. H.; Meller, A. Automated , Ultra-Fast Laser-Drilling of Nanometer Scale Pores and Nanopore Arrays in Aqueous Solutions. *Adv. Funct. Mater.* **2019**, *1900642*, 1–9. https://doi.org/10.1002/adfm.201900642.

(53) Firnkes, M.; Pedone, D.; Knezevic, J.; Döblinger, M.; Rant, U.; Döblinger, M.; Rant, U. Electrically Facilitated Translocations of Proteins through Silicon Nitride Nanopores: Conjoint and Competitive Action of Diffusion, Electrophoresis, and Electroosmosis. *Nano Lett.* **2010**, *10* (6), 2162–2167. https://doi.org/10.1021/nl100861c.

(54) Houghtaling, J.; Ying, C.; Eggenberger, O. M.; Fennouri, A.; Nandivada, S.; Acharjee, M.; Li, J.; Hall, A. R.; Mayer, M. Estimation of Shape, Volume, and Dipole Moment of Individual Proteins Freely Transiting a Synthetic Nanopore. *ACS Nano* **2019**, *13* (5), 5231–5242. https://doi.org/10.1021/acsnano.8b09555.

(55) Yusko, E. C.; Bruhn, B. R.; Eggenberger, O. M.; Houghtaling, J.; Rollings, R. C.; Walsh, N. C.; Nandivada, S.; Pindrus, M.; Hall, A. R.; Sept, D.; et al. Real-Time Shape Approximation and Fingerprinting of Single Proteins Using a Nanopore. *Nat. Nanotechnol.* **2016**, *12* (4), 360–367. https://doi.org/10.1038/nnano.2016.267.

(56) Morin, T. J.; McKenna, W. L.; Shropshire, T. D.; Wride, D. A.; Deschamps, J. D.; Liu, X.; Stamm, R.; Wang, H.; Dunbar, W. B. A Handheld Platform for Target Protein Detection and Quantification Using Disposable Nanopore Strips. *Sci. Rep.* **2018**, *8* (1), 14834. https://doi.org/10.1038/s41598-018-33086-7.

(57) Zhang, Y.; Rana, A.; Stratton, Y.; Czyzyk-Krzeska, M. F.; Esfandiari, L. Sequence-Specific Detection of MicroRNAs Related to Clear Cell Renal Cell Carcinoma at FM Concentration by an Electroosmotically Driven Nanopore-Based Device. *Anal. Chem.* **2017**, *89* (17), acs.analchem.7b01944. https://doi.org/10.1021/acs.analchem.7b01944.

(58) Carlsen, A. T.; Zahid, O. K.; Ruzicka, J. A.; Taylor, E. W.; Hall, A. R.; Carolina, N.; States, U. Selective Detection and Quantification of Modified DNA with Solid-State Nanopores. *Nano Lett.* **2014**, *14* (10), 5488–5492. https://doi.org/10.1021/nl501340d.

(59) Zahid, O. K.; Zhao, B. S.; He, C.; Hall, A. R. Quantifying Mammalian Genomic DNA Hydroxymethylcytosine Content Using Solid-State Nanopores. *Nat. Publ. Gr.* **2016**, *6* (April), 1–6. https://doi.org/10.1038/srep29565.

(60) Plesa, C.; Ruitenberg, J. W.; Witteveen, M. J.; Dekker, C. Detection of Individual Proteins Bound along DNA Using Solid-State Nanopores. *Nano Lett.* **2015**, *15* (5), 3153–3158. https://doi.org/10.1021/acs.nanolett.5b00249.

(61) Bell, N. A. W.; Keyser, U. F. Digitally Encoded DNA Nanostructures for Multiplexed, Single-Molecule Protein Sensing with Nanopores. *Nat. Nanotechnol.* **2016**, *11* (7), 645–651. https://doi.org/10.1038/nnano.2016.50.

(62) Kong, J.; Bell, N. A. W. W.; Keyser, U. F. Quantifying Nanomolar Protein Concentrations Using Designed DNA Carriers and Solid-State Nanopores. *Nano Lett.* **2016**, *16* (6), 3557–3562. https://doi.org/10.1021/acs.nanolett.6b00627.

(63) Bell, N. A. W.; Keyser, U. F. Specific Protein Detection Using Designed DNA Carriers and Nanopores. *J. Am. Chem. Soc.* **2015**, *137* (5), 2035–2041. https://doi.org/10.1021/ja512521w.

(64) Ren, R.; Zhang, Y.; Nadappuram, B. P.; Akpinar, B.; Klenerman, D.; Ivanov, A. P.; Edel, J. B.; Korchev, Y. Nanopore Extended Field-Effect Transistor for Selective Single-Molecule Biosensing. *Nat. Commun.* **2017**, *8* (1). https://doi.org/10.1038/s41467-017-00549-w.

(65) Chuah, K.; Wu, Y.; Vivekchand, S. R. C. C.; Gaus, K.; Reece, P. J.; Micolich, A. P.; Gooding, J. J. Nanopore Blockade Sensors for Ultrasensitive Detection of Proteins in Complex Biological Samples. *Nat. Commun.* **2019**, *10* (1), 1–9. https://doi.org/10.1038/s41467-019-10147-7.

(66) Li, Q.; Zhao, Q.; Lu, B. B.; Zhang, H.; Liu, S.; Tang, Z.; Qu, L.; Zhu, R.; Zhang, J.; You, L.; et al. Size Evolution and Surface Characterization of Solid-State Nanopores in Different Aqueous Solutions.

Nanoscale **2012**, *4* (5), 1572–1576. https://doi.org/10.1039/c2nr12040b.

(67) van den Hout, M.; Hall, A. R.; Wu, M. Y.; Zandbergen, H. W.; Dekker, C.; Dekker, N. H. Controlling Nanopore Size, Shape and Stability. *Nanotechnology* **2010**, *21* (11), 115304. https://doi.org/10.1088/0957-4484/21/11/115304.

(68) Koo, B.; Yorita, A. M.; Schmidt, J. J.; Monbouquette, H. G. Amplification-Free, Sequence-Specific 16S RRNA Detection at 1 AM. *Lab Chip* **2018**, *18* (15), 2291–2299. https://doi.org/10.1039/c8lc00452h.

(69) Duan, L.; Yobas, L. Label-Free Multiplexed Electrical Detection of Cancer Markers on a Microchip Featuring an Integrated Fluidic Diode Nanopore Array. *ACS Nano* **2018**, *12* (8), 7892–7900. https://doi.org/10.1021/acsnano.8b02260.

(70) Briggs, K.; Kwok, H.; Tabard-Cossa, V. Automated Fabrication of 2-Nm Solid-State Nanopores for Nucleic Acid Analysis. *Small* **2014**, *10* (10), 2077–2086. https://doi.org/10.1002/smll.201303602.

(71) Briggs, K. Solid-State Nanopores : Fabrication , Application , and Analysis. **2018**.

(72) Nicoli, F.; Verschueren, D.; Klein, M.; Dekker, C.; Jonsson, M. P. DNA Translocations through Solid-State Plasmonic Nanopores. *Nano Lett.* **2014**, *14* (12), 6917–6925. https://doi.org/10.1021/nl503034j.

(73) Carlsen, A. T.; Briggs, K.; Hall, A. R.; Tabard-Cossa, V. Solid-State Nanopore Localization by Controlled Breakdown of Selectively Thinned Membranes. *Nanotechnology* **2017**, *28* (8). https://doi.org/10.1088/1361-6528/aa564d.

(74) Ying, C.; Houghtaling, J.; Eggenberger, O. M.; Guha, A.; Nirmalraj, P.; Awasthi, S.; Tian, J.; Mayer, M. Formation of Single Nanopores with Diameters of 20-50 Nm in Silicon Nitride Membranes Using Laser-Assisted Controlled Breakdown. *ACS Nano* **2018**, *12* (11), 11458–11470. https://doi.org/10.1021/acsnano.8b06489.

(75) Smeets, R. M. M.; Keyser, U. F.; Krapf, D.; Wu, M.-Y.; Dekker, N. H.; Dekker, C. Salt Dependence of Ion Transport and DNA Translocation through Solid-State Nanopores. *Nano Lett.* **2006**, *6* (1), 89–95. https://doi.org/10.1021/nl052107w.

(76) Kowalczyk, S. W.; Grosberg, A. Y.; Rabin, Y.; Dekker, C. Modeling the Conductance and DNA Blockade of Solid-State Nanopores. *Nanotechnology* **2011**, *22* (31), 315101. https://doi.org/10.1088/0957-4484/22/31/315101.

(77) Verschueren, D. V.; Jonsson, M. P.; Dekker, C. Temperature Dependence of DNA Translocations through Solid-State Nanopores. *Nanotechnology* **2015**, *26* (23), 234004. https://doi.org/10.1088/0957-4484/26/23/234004.

(78) Hall, J. E. Access Resistance of a Small Circular Pore. *J. Gen. Physiol.* **1975**, *66* (2), 531–532. https://doi.org/10.1085/jgp.66.4.531.

(79) Chen, P.; Gu, J.; Brandin, E.; Kim, Y.-R. R.; Wang, Q.; Branton, D. Probing Single DNA Molecule Transport Using Fabricated Nanopores. *Nano Lett.* **2004**, *4* (11), 2293–2298. https://doi.org/10.1021/nl048654j.

(80) Li, J.; Gershow, M.; Stein, D.; Brandin, E.; Golovchenko, J. A. DNA Molecules and Configurations in a Solid-State Nanopore Microscope. *Nat. Mater.* **2003**, *2* (9), 611–615. https://doi.org/10.1038/nmat965.

(81) Storm, A. J.; Chen, J. H.; Zandbergen, H. W.; Dekker, C. Translocation of Double-Strand DNA through a Silicon Oxide Nanopore. *Phys. Rev. E - Stat. Nonlinear, Soft Matter Phys.* **2005**, *71* (5), 1–10. https://doi.org/10.1103/PhysRevE.71.051903.

(82) Chang, H.; Kosari, F.; Andreadakis, G.; Alam, M. A.; Vasmatzis, G.; Bashir, R. DNA-Mediated Fluctuations in Ionic Current through Silicon Oxide Nanopore Channels. *Nano Lett.* **2004**, *4* (8), 1551–1556. https://doi.org/10.1021/nl049267c.

(83) Ando, G.; Hyun, C.; Li, J.; Mitsui, T. Directly Observing the Motion of DNA Molecules near Solid-State

Nanopores. *ACS Nano* **2012**, *6* (11), 10090–10097. https://doi.org/10.1021/nn303816w.

(84) Muthukumar, M. Theory of Capture Rate in Polymer Translocation. *J. Chem. Phys.* **2010**, *132* (19). https://doi.org/10.1063/1.3429882.

(85) Rowghanian, P.; Grosberg, A. Y. Electrophoretic Capture of a DNA Chain into a Nanopore. *Phys. Rev. E - Stat. Nonlinear, Soft Matter Phys.* **2013**, *87* (4), 1–8. https://doi.org/10.1103/PhysRevE.87.042722.

(86) Nkodo, A. E.; Garnier, J. M.; Tinland, B.; Ren, H.; Desruisseaux, C.; McCormick, L. C.; Drouin, G.; Slater, G. W. Diffusion Coefficient of DNA Molecules during Free Solution Electrophoresis. *Electrophoresis* **2001**, *22* (12), 2424–2432. https://doi.org/10.1002/1522-2683(200107)22:12<2424::AID-ELPS2424>3.0.CO;2-1.

(87) Stellwagen, E.; Lu, Y.; Stellwagen, N. C.; Lu; Stellwagen, N. C. Unified Description of Electrophoresis and Diffusion for DNA and Other Polyions. *Biochemistry* **2003**, *42* (40), 11745–11750. https://doi.org/10.1021/bi035203p.

(88) Stellwagen, N. C.; Gelfi, C.; Righetti, P. G. The Free Solution Mobility of DNA. *Biopolymers* **1997**, *42* (6), 687–703. https://doi.org/10.1002/(SICI)1097-0282(199711)42:6<687::AID-BIP7>3.0.CO;2-Q.

(89) Rowghanian, P.; Grosberg, A. Y. Electrophoresis of a DNA Coil near a Nanopore. *Phys. Rev. E* **2013**, *87* (4), 1–9. https://doi.org/10.1103/PhysRevE.87.042723.

(90) Long, D.; Viovy, J.-L. L.; Ajdari, A. Simultaneous Action of Electric Fields and Nonelectric Forces on a Polyelectrolyte: Motion and Deformation. *Phys. Rev. Lett.* **1996**, *76* (20), 3858–3861. https://doi.org/10.1103/PhysRevLett.76.3858.

(91) Stellwagen, E.; Dong, Q.; Stellwagen, N. C. Monovalent Cations Affect the Free Solution Mobility of DNA by Perturbing the Hydrogen-Bonded Structure of Water. *Biopolymers* **2005**, *78* (2), 62–68. https://doi.org/10.1002/bip.20260.

(92) Kowalczyk, S. W.; Wells, D. B.; Aksimentiev, A.; Dekker, C. Slowing down DNA Translocation through a Nanopore in Lithium Chloride. *Nano Lett.* **2012**, *12* (2), 1038–1044. https://doi.org/10.1021/nl204273h.

(93) Davenport, M.; Healy, K.; Pevarnik, M.; Teslich, N.; Cabrini, S.; Morrison, A. P.; Siwy, Z. S.; Létant, S. E. The Role of Pore Geometry in Single Nanoparticle Detection. *ACS Nano* **2012**, *6* (9), 8366–8380. https://doi.org/10.1021/nn303126n.

(94) Farahpour, F.; Maleknejad, A.; Varnik, F.; Ejtehadi, M. R. Chain Deformation in Translocation Phenomena. *Soft Matter* **2013**, *9* (9), 2750–2759. https://doi.org/10.1039/c2sm27416g.

(95) Hyun, C.; Rollings, R.; Li, J. Probing Access Resistance of Solid-State Nanopores with a Scanning-Probe Microscope Tip. *Small* **2012**, *8* (3), 385–392. https://doi.org/10.1002/smll.201101337.

(96) Meller, A.; Branton, D. Single Molecule Measurement of DNA Transport through a Nanopore. *Electrophoresis* **2002**, *23* (16), 2583–2591. https://doi.org/10.1002/1522-2683(200208)23:16<2583::AID-ELPS2583>3.0.CO;2-H.

(97) Henrickson, S. E.; Misakian, M.; Robertson, B.; Kasianowicz, J. J. Driven DNA Transport into an Asymmetric Nanometer-Scale Pore. *Phys. Rev. Lett.* **2000**, *85* (14), 3057–3060. https://doi.org/10.1103/PhysRevLett.85.3057.

(98) Bell, N. A. W. W.; Muthukumar, M.; Keyser, U. F. Translocation Frequency of Double-Stranded DNA through a Solid-State Nanopore. *Phys. Rev. E - Stat. Nonlinear, Soft Matter Phys.* **2016**, *93* (2), 1–10. https://doi.org/10.1103/PhysRevE.93.022401.

(99) Meller, A.; Nivon, L.; Branton, D. Voltage-Driven DNA Translocations through a Nanopore. *Phys. Rev. Lett.* **2001**, *86* (15), 3435–3438. https://doi.org/10.1103/PhysRevLett.86.3435.

(100) Lee, K.; Park, K.-B.; Kim, H. H.-M.; Yu, J.; Chae, H.; Kim, H. H.-M.; Kim, K.-B. Recent Progress in Solid-State Nanopores. *Adv. Mater.* **2018**, *1704680* (42), 1–28. https://doi.org/10.1002/adma.201704680.

(101) Zahid, O. K.; Wang, F.; Ruzicka, J. A.; Taylor, E. W.; Hall, A. R. Sequence-Specific Recognition of MicroRNAs and Other Short Nucleic Acids with Solid-State Nanopores. *Nano Lett.* **2016**, *16* (3), 2033–2039. https://doi.org/10.1021/acs.nanolett.6b00001.

(102) Wanunu, M.; Dadosh, T.; Ray, V.; Jin, J.; McReynolds, L.; Drndić, M. Rapid Electronic Detection of Probe-Specific MicroRNAs Using Thin Nanopore Sensors. *Nat. Nanotechnol.* **2010**, *5* (11), 807–814. https://doi.org/10.1038/nnano.2010.202.

(103) Im, J.; Lindsay, S.; Wang, X.; Zhang, P. Single Molecule Identification and Quantification of Glycosaminoglycans Using Solid-State Nanopores. *ACS Nano* **2019**, *13* (6), 6308–6318. https://doi.org/10.1021/acsnano.9b00618.

(104) Larkin, J.; Henley, R. Y.; Muthukumar, M.; Rosenstein, J. K.; Wanunu, M. High-Bandwidth Protein Analysis Using Solid-State Nanopores. *Biophys. J.* **2014**, *106* (3), 696–704. https://doi.org/10.1016/j.bpj.2013.12.025.

(105) Plesa, C.; Kowalczyk, S. W.; Zinsmeester, R.; Grosberg, A. Y.; Rabin, Y.; Dekker, C. Fast Translocation of Proteins through Solid State Nanopores. *Nano Lett.* **2013**, *13* (2), 658–663. https://doi.org/10.1021/nl3042678.

(106) Waduge, P.; Hu, R.; Bandarkar, P.; Yamazaki, H.; Cressiot, B.; Zhao, Q.; Whitford, P. C.; Wanunu, M. Nanopore-Based Measurements of Protein Size, Fluctuations, and Conformational Changes. *ACS Nano* **2017**, *11* (6), acsnano.7b01212. https://doi.org/10.1021/acsnano.7b01212.

(107) Oukhaled, A.; Cressiot, B.; Bacri, L.; Pastoriza-Gallego, M.; Betton, J.-M. M.; Bourhis, E.; Jede, R.; Gierak, J.; Auvray, L. L.; Pelta, J. Dynamics of Completely Unfolded and Native Proteins through Solid-State Nanopores as a Function of Electric Driving Force. *ACS Nano* **2011**, *5* (5), 3628–3638. https://doi.org/10.1021/nn1034795.

(108) Singer, A.; Rapireddy, S.; Ly, D. H.; Meller, A. Electronic Barcoding of a Viral Gene at the Single-Molecule Level. *Nano Lett.* **2012**, *12* (3), 1722–1728. https://doi.org/10.1021/nl300372a.

(109) Morin, T. J.; Shropshire, T.; Liu, X.; Briggs, K.; Huynh, C.; Tabard-Cossa, V.; Wang, H.; Dunbar, W. B. Nanopore-Based Target Sequence Detection. *PLoS One* **2016**, *11* (5), e0154426. https://doi.org/10.1371/journal.pone.0154426.

(110) Beamish, E.; Tabard-Cossa, V.; Godin, M. Identifying Structure in Short DNA Scaffolds Using Solid-State Nanopores. *ACS Sensors* **2017**, *2* (12), 1814–1820. https://doi.org/10.1021/acssensors.7b00628.

(111) Sze, J. Y. Y.; Ivanov, A. P.; Cass, A. E. G.; Edel, J. B. Single Molecule Multiplexed Nanopore Protein Screening in Human Serum Using Aptamer Modified DNA Carriers. *Nat. Commun.* **2017**, *8* (1), 1–10. https://doi.org/10.1038/s41467-017-01584-3.

(112) Guo, Q.; Kong, T.; Su, R.; Zhang, Q.; Cheng, G. Noise Spectroscopy as an Equilibrium Analysis Tool for Highly Sensitive Electrical Biosensing. *Appl. Phys. Lett.* **2012**, *101* (9). https://doi.org/10.1063/1.4748931.

(113) Alibakhshi, M. A.; Halman, J. R.; Wilson, J.; Aksimentiev, A.; Afonin, K. A.; Wanunu, M. Picomolar Fingerprinting of Nucleic Acid Nanoparticles Using Solid-State Nanopores. *ACS Nano* **2017**, *11* (10), 9701–9710. https://doi.org/10.1021/acsnano.7b04923.

(114) Song, L.; Shan, D.; Zhao, M.; Pink, B. A.; Minnehan, K. A.; York, L.; Gardel, M.; Sullivan, S.; Phillips, A. F.; Hayman, R. B.; et al. Direct Detection of Bacterial Genomic DNA at Sub-Femtomolar Concentrations Using Single Molecule Arrays. *Anal. Chem.* **2013**, *85* (3), 1932–1939. https://doi.org/10.1021/ac303426b.

(115) Wang, F.; Zahid, O. K.; Swain, B. E.; Parsonage, D.; Hollis, T.; Harvey, S.; Perrino, F. W.; Kohli, R. M.; Taylor, E. W.; Hall, A. R. Solid-State Nanopore Analysis of Diverse DNA Base Modifications Using a Modular Enzymatic Labeling Process. *Nano Lett.* **2017**, *17* (11), 7110–7116. https://doi.org/10.1021/acs.nanolett.7b03911.

(116) Shim, J.; Kim, Y.; Humphreys, G. I.; Nardulli, A. M.; Kosari, F.; Vasmatzis, G.; Taylor, W. R.; Ahlquist, D.

A.; Myong, S.; Bashir, R. Nanopore-Based Assay for Detection of Methylation in Double-Stranded DNA Fragments. *ACS Nano* **2015**, *9* (1), 290–300. https://doi.org/10.1021/nn5045596.

(117) Wanunu, M.; Wang, M. X.; Mcreynolds, L.; Wang, Y.; Gu, L. Q.; Wanunu, M.; Wang, M. X.; Mcreynolds, L.; Wang, Y. Detection of MiRNAs with a Nanopore Single-Molecule Counter. *Expert Rev. Mol. Diagn.* **2012**, *12* (6), 573–584. https://doi.org/10.1586/erm.12.58.

(118) Wang, Y.; Zheng, D.; Tan, Q.; Wang, M. X.; Gu, L. Q. Nanopore-Based Detection of Circulating MicroRNAs in Lung Cancer Patients. *Nat. Nanotechnol.* **2011**, *6* (10), 668–674. https://doi.org/10.1038/nnano.2011.147.

(119) Lin, Y.; Ying, Y.-L. L.; Shi, X.; Liu, S.-C. C.; Long, Y.-T. T. Direct Sensing of Cancer Biomarkers in Clinical Samples with a Designed Nanopore. *Chem. Commun.* **2017**, *53* (84), 11564–11567. https://doi.org/10.1039/c7cc06775e.

(120) Briggs, K.; Madejski, G.; Magill, M.; Kastritis, K.; de Haan, H. W.; McGrath, J. L.; Tabard-Cossa, V. DNA Translocations through Nanopores under Nanoscale Preconfinement. *Nano Lett.* **2018**, *18* (2), 660–668. https://doi.org/10.1021/acs.nanolett.7b03987.

(121) Frament, C. M.; Bandara, N.; Dwyer, J. R. Nanopore Surface Coating Delivers Nanopore Size and Shape through Conductance-Based Sizing. *ACS Appl. Mater. Interfaces* **2013**, *5* (19), 9330–9337. https://doi.org/10.1021/am4026455.

(122) Frament, C. M.; Dwyer, J. R. Conductance-Based Determination of Solid-State Nanopore Size and Shape: An Exploration of Performance Limits. *J. Phys. Chem. C* **2012**, *116* (44), 23315–23321. https://doi.org/10.1021/jp305381j.

(123) Bandara, Y. M. N. D. Y.; Nichols, J. W.; Iroshika Karawdeniya, B.; Dwyer, J. R. Conductance-Based Profiling of Nanopores: Accommodating Fabrication Irregularities. *Electrophoresis* **2018**, *39* (4), 626–634. https://doi.org/10.1002/elps.201700299.

(124) Mao, M.; Sherwood, J. D.; Ghosal, S. Electro-Osmotic Flow through a Nanopore. *J. Fluid Mech.* **2014**, *749*, 167–183. https://doi.org/10.1017/jfm.2014.214.

(125) Luan, B.; Aksimentiev, A. Control and Reversal of the Electrophoretic Force on DNA in a Charged Nanopore. *J. Phys. Condens. Matter* **2010**, *22* (45), 454123. https://doi.org/10.1088/0953-8984/22/45/454123.

(126) Ermann, N.; Hanikel, N.; Wang, V.; Chen, K.; Weckman, N. E.; Keyser, U. F. Promoting Single-File DNA Translocations through Nanopores Using Electro-Osmotic Flow. *J. Chem. Phys.* **2018**, *149* (16). https://doi.org/10.1063/1.5031010.

(127) Wong, C. T. A. A.; Muthukumar, M. Polymer Capture by Electro-Osmotic Flow of Oppositely Charged Nanopores. *J. Chem. Phys.* **2007**, *126* (16). https://doi.org/10.1063/1.2723088.

(128) Buyukdagli, S.; Ala-Nissila, T. Controlling Polymer Capture and Translocation by Electrostatic Polymer-Pore Interactions. *J. Chem. Phys.* **2017**, *147* (11). https://doi.org/10.1063/1.5004182.

(129) Tabard-Cossa, V.; Trivedi, D.; Wiggin, M.; Jetha, N. N.; Marziali, A. Noise Analysis and Reduction in Solid-State Nanopores. *Nanotechnology* **2007**, *18* (30), 305505. https://doi.org/10.1088/0957-4484/18/30/305505.

(130) Karau, P.; Tabard-Cossa, V. Capture and Translocation Characteristics of Short Branched DNA Labels in Solid-State Nanopores. *ACS Sensors* **2018**, *3* (7), 1308–1315. https://doi.org/10.1021/acssensors.8b00165.

(131) Forstater, J. H. J. H.; Briggs, K.; Robertson, J. W. F. F. J. W. F.; Ettedgui, J.; Marie-Rose, O.; Vaz, C.; Kasianowicz, J. J. J.; Tabard-Cossa, V.; Balijepalli, A. MOSAIC: A Modular Single-Molecule Analysis Interface for Decoding Multistate Nanopore Data. *Anal. Chem.* **2016**, *88* (23), 11900–11907. https://doi.org/10.1021/acs.analchem.6b03725.

(132) Raillon, C.; Granjon, P.; Graf, M.; Steinbock, L. J.; Radenovic, A. Fast and Automatic Processing of Multi-

Level Events in Nanopore Translocation Experiments. *Nanoscale* **2012**, *4* (16), 4916. https://doi.org/10.1039/c2nr30951c.

(133) Nomidis, S. K.; Hooyberghs, J.; Maglia, G.; Carlon, E. DNA Capture into the ClyA Nanopore: Diffusion-Limited versus Reaction- Limited Processes. *J. Phys. Condens. Matter* **2018**, *30* (30). https://doi.org/10.1088/1361-648X/aacc01.

(134) Vollmer, S. C.; De Haan, H. W. Translocation Is a Nonequilibrium Process at All Stages: Simulating the Capture and Translocation of a Polymer by a Nanopore. *J. Chem. Phys.* **2016**, *145* (15). https://doi.org/10.1063/1.4964630.

(135) Storm, A. J.; Storm, C.; Chen, J. H.; Zandbergen, H. W.; Joanny, J.-F. J.-F. F.; Dekker, C.; Abdulagatov, I. M.; Zeinalova, A. B.; Azizov, N. D.; Abe, T.; et al. Fast DNA Translocation through a Solid-State Nanopore. *Nano Lett.* **2005**, *5* (7), 1193–1197. https://doi.org/10.1021/nl048030d.

(136) Mihovilovic, M.; Hagerty, N.; Stein, D. Statistics of DNA Capture by a Solid-State Nanopore. *Phys. Rev. Lett.* **2013**, *110* (2), 1–5. https://doi.org/10.1103/PhysRevLett.110.028102.

(137) Sherwood, J. D.; Mao, M.; Ghosal, S. Electroosmosis in a Finite Cylindrical Pore: Simple Models of End Effects. *Langmuir* **2014**, *30* (31), 9261–9272. https://doi.org/10.1021/la502349g.

(138) Hoogerheide, D. P.; Lu, B.; Golovchenko, J. A. Pressure-Voltage Trap for DNA near a Solid-State Nanopore. *ACS Nano* **2014**, *8* (7), 7384–7391. https://doi.org/10.1021/nn5025829.

(139) Zhang, H.; Zhao, Q.; Tang, Z.; Liu, S.; Li, Q.; Fan, Z.; Yang, F.; You, L.; Li, X.; Zhang, J.; et al. Slowing down DNA Translocation through Solid-State Nanopores by Pressure. *Small* **2013**, *9* (24), 4112–4117. https://doi.org/10.1002/smll.201301263.

(140) Lu, B.; Hoogerheide, D. P.; Zhao, Q.; Zhang, H.; Tang, Z.; Yu, D.; Golovchenko, J. A. Pressure-Controlled Motion of Single Polymers through Solid-State Nanopores. *Nano Lett.* **2013**, *13* (7), 3048–3052. https://doi.org/10.1021/nl402052v.

(141) Charron, M.; Briggs, K.; King, S.; Waugh, M.; Tabard-Cossa, V. Precise DNA Concentration Measurements with Nanopores by Controlled Counting. *Anal. Chem.* **2019**, *91* (19), acs.analchem.9b01900. https://doi.org/10.1021/acs.analchem.9b01900.

(142) Phys, J. C.; Jeon, B. J.; Muthukumar, M. Polymer Capture by A-Hemolysin Pore upon Salt Concentration Gradient. *J. Chem. Phys.* **2014**, *140* (1). https://doi.org/10.1063/1.4855075.

(143) He, Y.; Tsutsui, M.; Scheicher, R. H.; Miao, X. S.; Taniguchi, M. Salt-Gradient Approach for Regulating Capture-to-Translocation Dynamics of DNA with Nanochannel Sensors. *ACS Sensors* **2016**, *1* (6), 807–816. https://doi.org/10.1021/acssensors.6b00176.

(144) He, Y.; Tsutsui, M.; Scheicher, R. H.; Fan, C.; Taniguchi, M.; Kawai, T. Mechanism of How Salt-Gradient-Induced Charges Affect the Translocation of DNA Molecules through a Nanopore. *Biophys. J.* **2013**, *105* (3), 776–782. https://doi.org/10.1016/j.bpj.2013.05.065.

(145) Chou, T. Enhancement of Charged Macromolecule Capture by Nanopores in a Salt Gradient. *J. Chem. Phys.* **2009**, *131* (3). https://doi.org/10.1063/1.3170952.